Ambient Backscatterers For Low Cost and Low Power Wireless Applications

Spyridon Nektarios Daskalakis
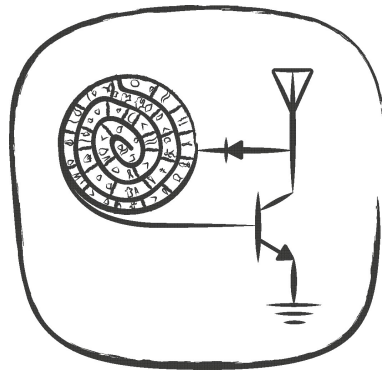
HERIOT-WATT UNIVERSITY

INSTITUTE OF SIGNALS, SENSORS AND SYSTEMS,
SCHOOL OF ENGINEERING & PHYSICAL SCIENCES.

February, 2020

Abstract

Sensors that are used in Internet-of-Things (IoT) area are hampered by extremely high costs and excessive battery power consumption – but wireless, reflective, sensor-tags could help address these issues. In agricultural applications: in order to monitor a field of 500 plants, the operating cost will typically rack up hundreds of pounds per field and will gobble tens of milliwatts per sensor. In this thesis we have tried to address some of these shortfalls by opting for each plant to have an antenna, one transistor that acts as a switch, and one microcontroller. Each sensor uses wireless communication based on a reflections technology known as backscatter. The antenna acts as a mirror and when it is illuminated with a signal, it reflects back the wave. The signal comes from an FM radio station and it is freely available in the air. The plant-sensor can modulate the information by a very smart switching of this antenna. We are trying, under laboratory conditions, to combine this low power, low-cost technology with tape-based, flexible nanomaterial printed sensors. As nanotechnology enables flexible inkjet printed electronics to revolutionise IoT applications, we developed a new technology and we hope that our nanomaterial-based printed circuit sensors will help push state-of-the-art additive manufacturing in agricultural technology.

To my family and to my real mentors.

Acknowledgements

Infinite thanks to my supervisors Apostolos Georgiadis and George Goussetis for always believing in me and supporting me during this adventure. Their trust and help was the essential parameter that brought me here. Fortunately, I also had the pleasure to meet and work with my external supervisor Manos Tentzeris from the School of Electrical and Computer Engineering, Georgia Institute of Technology and visit his lab twice during my studies. My supervisors' knowledge, patience and positive attitude always was a motivation for me to continue, work hard and finally achieve my goals.

I need to express countless gratitude to all the guys from the Microwaves and Antenna Engineering Research Group, Heriot-Watt University and especially to all my officemates, that made me feel at home in a foreign country. I think this would have never been possible without their support. They became my second family and their help made this process easier.

I would like to thank also all members of Agile Technologies for High-performance Electromagnetics Novel Applications (ATHENA) Group, Georgia Institute of Technology, Atlanta, GA for their help in various steps throughout this work.

I deeply thank Ricardo Correia, Nuno Borges Carvalho and Daniel Belo from Departamento de Electrónica, Telecomunicações e Informática, Instituto de Telecomunicações, Universidade de Aveiro, Aveiro, Portugal. Their contribution was huge in this work!

Finally and more importantly, I want to thank my parents, my sister and brother, that were always by my side no matter what and made me feel at home. Also a big thanks to that persons that made me smiling and crying during this difficult trip of life!

Contents

List of Tables

List of Figures

Glossary [1]

ADC	Analog-to-digital converter
ADS	Advance Design System
AGC	Automatic gain control
AP	Access point
AWG	Arbitrary waveform generator
BER	Bit error rate
BLE	Bluetooth low energy
BOM	Bill of materials
BW	Bandwidth
CFO	Carrier frequency offset
CLT	Central limit theorem
CMOS	Complementary metal–oxide–semiconductor
CSS	chirp spread spectrum
CW	Continuous wave
DAC	Digital-to-analog converter
DC	Direct current
DFT	Discrete Fourier transform
DTV	Digital television
EIRP	Effective isotropic radiated power
EUR	Euro
FCC	Federal communications commission
FDMA	Frequency-division-multiple-access
FEC	Forward error correction
FM	Frequency modulation
FPGA	Field programmable gate array
FSK	Frequency-shift keying

---

[1]In alphabetical order.

Glossary [2]

GBP	British pound sterling
GPS	Global positioning system
GSM	Global system mobile
IC	Integrated circuit
IoT	Internet-of-things
IQ	Inphase-Quadrature
LFM	Linear frequency modulated
LNA	Low noise amplifier
LoRa	Long range
LoS	Line-of-Sight
LPWAN	Low-power wide area network
LTE	Long-term evolution
LWS	Leaf wetness sensors
MCU	Microcontroller
NB	Narrow-band
OOK	On-off keying
OTA	Over-the-air
PCB	Printed circuit board
PER	Packet error rate
pHEMT	Pseudomorphic high electron mobility transistor
PSK	Phase-shift keying
QAM	Quadrature amplitude modulation
RBDS	Radio broadcast data system
RDS	Radio data system
RF	Radio Frequency
RFID	Radio frequency identification

---

[2]In alphabetical order.

Glossary ^{3}

RTC	Real-time clock
RX	Receiver
SDR	Software defined radio
SMA	SubMiniature version A
SF	Spreading factor
SNP	Silver nanoparticle
SNR	Signal-to-noise-ratio
SPDT	Single-pole, single-throw
SPST	Single-pole, single-throw
TDMA	Time-division-multiple-access
TV	Television
TX	Transmitter
UHF	Ultra high frequency
UNB	Ultra narrowband
USB	Universal serial bus
USD	United states dollar
VCO	Voltage-controlled oscillator
VHF	Very high frequency
VNA	Vector network analyser
VSA	Vector signal analyser
VSWR	Voltage standing wave ratio
WDS	Water deficit stress
WLAN	Wireless local area networks
WPT	Wireless power transfer
WPM	Words per minute
WSN	Wireless sensor network
WWAN	Wireless wide area networks

---

[3]In alphabetical order.

List of Symbols

ω Angular frequency

Z_a Antenna impedance

Γ Reflection coefficient

π Mathematical constant 3.14159

μ Mean

σ Variance

$\tan\delta$ Loss tangent

ε_r Permittivity in the dielectric

ϕ Phase

λ Guided wavelength

List of publications

Journal papers

1. D. Belo, R. Correia, Y. Ding, **S. N. Daskalakis**, G. Goussetis, A. Georgiadis, and N. B. Carvalho, "IQ Impedance Modulator Front-End for Low-Power LoRa Backscattering Devices", in *IEEE IEEE Transactions on Microwave Theory and Techniques (TMTT)*, pp. 1-8, October 2019.

2. **S. N. Daskalakis**, G. Goussetis, M. M. Tentzeris and A. Georgiadis, "A Rectifier Circuit Insensitive to the Angle of Incidence of Incoming Waves Based on a Wilkinson Power Combiner", in *IEEE TMTT*, vol. 67, no. 7, pp. 3210-3218, July 2019.

3. **S. N. Daskalakis**, R. Correia, G. Goussetis, M. M. Tentzeris, N. B. Carvalho and A. Georgiadis, "4-PAM Modulation of Ambient FM Backscattering for Spectrally Efficient Low Power Applications", in IEEE TMTT, vol. 66, no. 12, pp. 5909-5921, December 2018.

4. **S. N. Daskalakis**, G. Goussetis, S. D. Assimonis, M. M. Tentzeris and A. Georgiadis, "A uW Backscatter-Morse-Leaf Sensor for Low Power Agricultural Wireless Sensor Networks", in *IEEE Sensors Journal*, vol. 18, no. 19, pp. 7889-7898, Oct. 2018.

5. **S. N. Daskalakis**, J. Kimionis, A. Collado, G. Goussetis, M. M. Tentzeris and A. Georgiadis, "Ambient Backscatterers using FM Broadcasting for Low Cost and Low Power Wireless Applications", in *IEEE TMTT*, vol. 65, no. 12, pp. 5251-5262, November 2017.

6. A. Collado, **S. N. Daskalakis**, K. Niotaki, R. Martinez, F. Bolos and A. Georgiadis, "Rectifier Design Challenges for RF Wireless Power Transfer and Energy Harvesting Systems", in *RADIOENGINEERING*, vol. 26, no. 1, April 2017.

Book Chapters

1. **S. N. Daskalakis**, R. Correia, J. Kimionis, G. Goussetis, M. M. Tentzeris, N. B. Carvalho, A. Georgiadis, "paAmbient FM Backscattering Low Cost and Low Power Wireless RFID Applications", Wireless Power Transmission for Sustainable Electronics: COST WiPE - IC1301, Editor N. Carvalho and Apostolos Georgiadis, April 2020.

Conferences

1. **S. N. Daskalakis**, G. Goussetis and A. Georgiadis, "NFC Hybrid Harvester for Battery-free Agricultural Sensor Nodes", *IEEE International Conference on RFID-Technology and Applications (RFID-TA)*, Pisa, Italy, September 2019.

2. B. A. Mouris, W. Elshennawy, P. Petridis, and **S. N. Daskalakis**, "Rectenna for Bluetooth Low Energy Applications", *IEEE Wireless Power Transfer Conference (WPTC)*, London, UK, June 2019.

3. **S. N. Daskalakis**, A. Georgiadis, G. Goussetis and M. M. Tentzeris, "Low Cost Ambient Backscatter for Agricultural Applications" *International Conference on Electromagnetics in Advanced Applications (ICEAA 2019)*, Granada, Spain, September 2019.

4. **S. N. Daskalakis**s, S. D. Assimonis, G. Goussetis, M. M. Tentzeris and A. Georgiadis, "The Future of Backscatter in Precision Agriculture", *IEEE International Symposium on Antennas and Propagation and USNC-URSI Radio Science Meeting (AP-S/URSI)* 2019, Atlanta, Georgia, USA, June 2019.

5. S. D. Assimonis, **S. N. Daskalakis**, V. Fusco, M. M. Tentzeris and A. Georgiadis, "High Efficiency RF Energy Harvester for IoT Embedded Sensor Nodes", *IEEE International Symposium on Antennas and Propagation and USNC-URSI Radio Science Meeting (AP-S/URSI)* 2019, Atlanta, Georgia, USA, June 2019.

6. R. Correia, Y. Ding, **S. N. Daskalakis**, P. Petridis, G.Goussetis, A. Georgiadis and N. B. Carvalho, "Chirp Based Backscatter Modulation", *IEEE International Microwave Symposium (IMS)*, Boston, Massachusetts, USA, June

15. A. Servent, **S. N. Daskalakis**, A. Collado and A. Georgiadis, "A Proximity Wireless Sensor Based on Backscatter Communication", *International Applied Computational Electromagnetics Society Symposium (ACES)*, Firenze, Italy, March 2017.

Chapter 1

Introduction

According to the UN Food and Agriculture Organization, food production must be increased by 70% by 2050 [1]. In order to meet this demand, the use of wireless sensor networks (WSNs) in agriculture is an essential way for larger production capabilities [2]. Farmers will benefit by a high-range of energy-efficient sensors which will reduce their operational costs and water waste in general. Sensing environmental parameters as temperature, humidity and pressure over field areas can offer a precise analysis of the generated micro-climate conditions. Today, one of the main challenges is to minimise the cost and energy consumption of the existing sensor-nodes. There is a variety of wireless sensor products in the market (i.e., ZigBee, LoRa) from 40 to 4000 USD per sensor-node. Thus the networking cost of 100 plants (e.g. one sensor/plant) becomes prohibitive. The solution to this problem is a novel technique, based on reflection principles and it is called backscatter communication. It is used in radio frequency identification (RFID) systems where the sensor-node/tag receives a radio frequency (RF) wave from an emitter and sends its information back to a reader wirelessly by reflecting and modulating this incident RF signal.

This thesis discusses four novel implementations of a low-cost and low-power tags for agricultural and general Internet-of-Things (IoT) applications that utilize novel sensing and backscatter techniques at the same time. It is noted that all the proposed tags can be a part of a backscatter WSN, transmitting data to a reader.

Typical RFID systems require a continuous wave (CW) emitter, the sensor node/tag and a reader. In this thesis the reader is also defined as receiver. The reader provides the CW for both power supply and communication purposes.
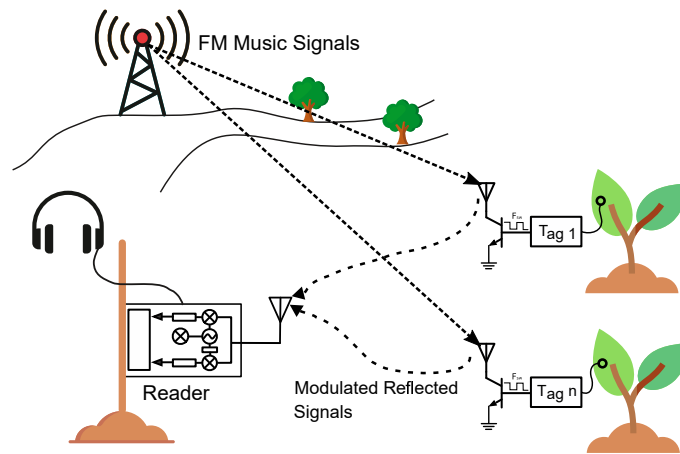
Figure 1.1: FM ambient backscatter concept. Broadcast music signals are modulated by the tags and are scattered back to a reader.

Recently, the ambient RF signals have been proposed for backscatter communication instead of a CW signal. Ambient backscattering is an idea based on the bistatic backscatter philosophy and could constitute a very promising novel approach for extremely low power and low-cost communication systems. Cellular, television, frequency modulation (FM) radio and Wi-Fi signals are typically widely available in urban areas indoors and outdoors during day and night. In our case, as the applications needs to be outdoors, far away from industrial centers, only the ambient FM signals are suitable for long-range communication. The tags, can reflect the ambient music signals from nearby FM stations in order to communicate with a FM receiver (Fig. 1.1). By using ambient signals for backscattering, the reader architecture is simplified and its power consumption is reduced dramatically since it does not need a transmitter but only a receiver circuit. The receiver consists of a commercial low-cost software-defined radio (SDR) that downconverts the received signal to baseband (0 Hz) and decodes it through a signal processing algorithm. The novel proof-of-concept prototypes are batteryless and were powered by flexible solar panels.

1.1 Document Overview

My contribution is relevant to backscatter sensor networks and energy harvesting while my experience is based on designing energy harvesting circuits and low-power/cost sensor circuits. The proposed work was designed and implemented dur-

ing my studies in Heriot-Watt University and during my visit in ATHENA (Agile Technologies for High-performance Electromagnetics Novel Applications) lab, Georgia Institute of Technology. More specifically, I was with ATHENA lab under the guidance of professor Manos Tentzeris and my supervisor Apostolos Georgiadis. I joined the group as research scholar for 6 months. The School of Electrical and Computer Engineering Georgia Institute of Technology has strong experience in inkjet-printed sensors and RF electronics. During my visiting period, I was able to: 1) Use of state-of-the-art fabrication, laboratory and test equipment. 2) Obtain knowledge on 3D-printed/Inkjet-printed RF electronics, batteries and sensors.

This thesis presents tag implementations that has the potential to be the next new primitive approach for extremely low power wireless communication systems. The configurations are explained in individual chapters, with a total of six chapters including the introduction chapter 1 and the future work chapter 6. Chapters 2, 3 present backscatter systems using dedicated CW emitters for the communication while chapters 4, 5 describe the novel FM ambient backscatter technique without the use of a dedicated CW emitter. A part of the proposed work (chapter 4) is a natural continuation of my background and with the help and expertise of the host lab. It must be noted that chapter 3 is a contribution of my collaborators Ricardo Correia and Daniel Belo with Departamento de Electrónica, Telecomunicações e Informática, Instituto de Telecomunicações, Universidade de Aveiro, Portugal. Every chapter has its own introduction/conclusion section and every introduction section includes the motivation and the literature review part. The thesis is organised as follows.

Chapter 2 presents a novel, low-cost and low-power system for leaf sensing using a new plant backscatter sensor node/tag. The latter, can result in the prevention of water waste (water-use efficiency), when is connected to an irrigation system. Specifically, a leaf sensor measures the temperature differential between the leaf and the air, which is directly related to the plant water stress. The tag collects information from the leaf sensor through an analog-to-digital converter (ADC) and communicates remotely with a low-cost software-defined radio (SDR) reader using backscatter communication. The tag consists of the sensor board, a microcontroller (MCU), an external timer and an RF front-end for communication. The timer produces a subcarrier frequency for simultaneous access of multiple tags. The proposed

work could be scaled and be a part of a large backscatter WSN. The communication protocol exploits for the first time, low-complexity Morse code modulation on a 868 MHz carrier signal. The presented novel proof-of-concept prototype is battery-less and was powered by a flexible solar panel consuming power around 20 μW. The performance was validated in an indoors environment where wireless communication was successfully achieved up to 2 m distance.

Chapter 3 presents the design of an IQ impedance modulator which is used to generate Long-Range (LoRa) symbols with backscattering techniques, allowing building low-power devices that may be compatible with the current LoRa networks. It is shown that a linear frequency modulated (LFM) chirp can be generated by properly varying the phase of a reflected wave instead of directly varying its instantaneous frequency. The proposed device consists of two RF transistors that generate a set of impedances by changing their gate bias, allowing reflecting their incident wave with predefined phase values. By joining these two reflected waves in quadrature, a new set of impedances is obtained whose phases vary 360 degrees, on a constant voltage standing wave ratio (VSWR) circle. In order to validate the proposed design, several LoRa symbols were generated, successfully transmitted and decoded. Measurements of the bit error rate (BER) versus signal-to-noise ratio (SNR) were conducted and shown to be in accordance with other related work. Moreover, the impact of intentional perturbations added to the control bias voltages was analyzed and tests over-the-air (OTA) were performed for different indoor propagation scenarios.

Chapter 4 introduces a novel wireless tag and receiver system that utilizes broadcast FM signals for backscatter communication. Although backscatter radio communication is a mature technology used in RFID applications, ambient backscattering is a novel approach taking advantage of ambient signals to simplify wireless system topologies to just a sensor node and a receiver circuit eliminating the need for a dedicated carrier source. The proposed tag consists of an ultra-low-power microcontroller (MCU) and a radio frequency front-end for wireless communication. The MCU can accumulate data from multiple sensors through an ADC, while it transmits the information back to the receiver through the front-end by means of backscattering. The front-end uses On-Off keying (OOK) modulation and FM0 encoding with

ambient FM station signals. The receiver consists of a commercial low-cost software-defined radio which downconverts the received signal to baseband and decodes it using a suitable signal processing algorithm. A theoretical analysis of the error rate performance of the system is provided and compared to bit-error-rate measurements on a fixed transmitter-tag-receiver laboratory setup with good agreement. The prototype tag was also tested in a real-time indoor laboratory deployment. Operation over a 5 m tag-reader distance was demonstrated by backscattering information at 2.5 Kbps featuring an energy per packet of 36.9 μJ.

Chapter 5 presents a novel wireless tag, which for the first time utilizes 4-pulse amplitude modulation (4-PAM) technique to modulate the ambient backscattered FM signals in order to send data to a nearby low-cost software-defined radio reader. The tag is based on an RF front-end that uses a single transistor controlled by an ultra low-power MCU. The MCU includes an ADC for sensing and a digital-to-analog converter (DAC) for RF front-end control. A proof-of-concept prototype is demonstrated in an indoor environment with the low bit rate of 345 bps and power consumption 27 μW. It operated using a FM station 34.5 Km away and the tag-to-reader distance was tested from 1 m. The value of energy spent in this modulator was 78.2 nJ/bit at 345 bps and 27.7 nJ/bit at 10.2 Kbps.

Chapter 2

Backscatter Communication

2.1 Introduction

Recently, IoT has become the trend for networking every day objects so as to automate and make easier our daily lives. During the last decade there has been a rapid growth of the technologies related to IoT, applying mechanical, material and electrical innovations in a variety of sectors such as agriculture, smart cities, smart homes and autonomous vehicles. In the near future IoT is expected to connect millions of sensors through WSNs. The most important challenge for IoT applications, is the minimization of the cost and energy dissipation of the sensors. Keeping the massive number of energy-constrained IoT sensors active with low cost designs is a key issue. For example, in farming applications, covering a big field with dozens of sensors requires a cost on the order of thousands Euros (100 $\sim$ 200 EUR per sensor node). In case of sensors that are deployed within materials such as walls or even the human body, battery recharging or replacement is difficult if not impossible. Commercial radio modules used in IoT devices typically use power-hungry RF chains including oscillators, mixers and DACs resulting in significant limitations of the battery life. One particularly promising approach to alleviate these issues is backscatter communication [3] that allows IoT sensor nodes-tags to transmit data by reflecting and modulating an incident RF wave [4]. Communication using backscatter principles has been widely deployed in the application of RFID for passive tags [5]. The wireless communication part (RF front-end) of each tag can be simplified into a single RF transistor and an antenna, which can be used for each sensor tag

to send information to a base station (reader). In this case the tags are battery-free and can operate using only RF power transmitted from an RFID reader resulting in communication ranges up to several meters [6, 7].

Alternatively, semi-passive tags (energy assisted) are built in bi-static architectures where the CW emitter and the reader are not co-located [8]. The tag power is supplied by a small battery and longer communication distances can be achieved. For example, in a recent work [9] an effective communication was observed over a tag-to-reader distance in excess of 250 m. In [10], a field programmable gate array (FPGA) based tag can create up to 11 Mbps WiFi and ZigBee compatible signals by backscattering Bluetooth transmissions.

Binary amplitude shift keying or phase shift keying (ASK or PSK) modulations are commonly used for the communication between the tag and reader, such that information is encoded using two states of the amplitude or the phase of the reflected CW [11]. For example in the WISP platform [6], the communication protocol employs 2-ASK modulation to encode the bits 1 and 0 with long and short gaps in RF power, respectively. Recently, a body implanted device powered by a 13.56 MHz wireless power transfer (WPT) link, uplinks neural data at 915 MHz using a binary (BPSK) backscatter modulation [12]. In the aforementioned examples, the reader provides the CW for supply and communication purposes.

In order to increase the data rate, other works have exploited higher order modulation schemes for semi-passive and passive sensor networks [13–15]. In [14] the authors present a 4-quadrature amplitude modulation (QAM) scheme for backscatter communication enabling the transmission of 2 bits per symbol instead of 1 bit with 2-ASK, effectively increasing the data rate and leading to a reduced on-chip power consumption. The modulator involved a battery-assisted (semi-passive) and a passive tag operating in the range of $850 - 950$ MHz. This system demonstrated transmission of 4-PSK/4-QAM with a bit rate of 400 kbps and with static power dissipation of 115 nW. The backscatter modulator uses four lumped impedances connected to an RF switch and it was controlled by a microcontroller (MCU). The same authors developed a 16-QAM modulator for ultra high frequency (UHF) backscatter communication with five switches. Using a 16-to-1 multiplexer, they were able to modulate the antenna load between 16 different states [16]. The tag was tested on

a 915 MHz, +23 dBm, CW signal. The tag-to-reader range was measured at 1.24 m with a high bit rate 96 Mbps. In [17] a novel backscatter modulator is presented which employs a Wilkinson power divider and two switches. The divider introduces a phase shift in one of the branches and two transistors acting as switches. High order backscatter modulations of M-QAM or M-pulse amplitude modulation (M-PAM) can be achieved as each transistor can be controlled with different voltage levels to achieve different reflection coefficient values. The 16-QAM modulator demonstrated in [17], features an energy consumption as low as 6.7 pJ/bit for a bit rate of 120 Mbps. In work [18] is presenting a 5.8 GHz RF-powered complementary metal–oxide–semiconductor (CMOS) transceiver with 32-QAM communication scheme. The uplink part uses the backscattering technique with a modulation 32-QAM while consuming 113 μW at 0.6 V. The RF font-end of the design consists of two transistors and the quadrature modulation is realized by two intermediate frequency (IF) signals (I/Q). In [19] a tutorial survey of backscatter modulation is provided as an emerging means for short-range low-rate communications. It provides the relationship between on-tag power harvesting and forward error correction applied to the higher order modulation work [13].

Ambient backscattering is an idea based on the bistatic backscatter philosophy and could constitute a very promising novel approach for extremely low power and low cost communication system [20]. In the next chapters 4, 5 we describe two communication systems with different modulation schemes using the ambient backscattering technique.

2.2   Backscatter for Agriculture

Precision agriculture methods allow farmers to maximize yields using minimal resources such as water, fertilizer, pesticides and seeds. By deploying sensors and monitoring fields, farmers can manage their crops at micro scale [21]. This is also useful in order to predict diseases, conserve the resources and reduce the impacts of the environment. Smart agriculture has roots going back to the 1980s when global positioning system (GPS) capability became accessible for civilian use. Once farmers were able to accurately map their crop fields, they could monitor and apply

fertilizer and weed treatments only to areas that required it. During the 1990s, early precision agriculture users adopted crop yield monitoring to generate fertilizer and pH correction recommendations. As more variables could be measured by sensors and were introduced into a crop model, more accurate recommendations could be made. The combination of the aforementioned systems with WSNs allows multiple unassisted embedded devices (sensor nodes) to transmit wirelessly data to central base stations [22, 23]. The base stations are able to store the data into cloud databases for worldwide processing and visualization [24]. Data (e.g., temperature, humidity, pressure) are collected from different on-board physical sensors: dielectric soil moisture sensors, for instance, are widespread for moisture measurements, since they can estimate the moisture levels through the dielectric constant of the soil, which changes as the soil moisture is changing.

Transpiration is an important physiological process of plants and it is defined as the evaporation of water from leaves (through stomata), stems and flowers. After the watering procedure, water uptake by roots, transport through the xylem and goes out from the stomata of leaves to the atmosphere. When the stomata are open, water vapour escapes from the leaves, increasing the local humidity on the leaf surface. Consequently, by installing humidity sensors on leaves surface it is possible to monitor that humidity variation. In [25], the authors have developed graphene-based "tattoo" sensors in order to track the key time points at which significant water loss occurs at the leaves. The sensing is based on changes in the electrical resistance of graphene strips in different moisture levels.

Leaf sensing is an another way to measure the water status of a plant. When compared to soil moisture sensors, they can provide more accurate data since the measurements are directly taken on the plant and not through the soil or the atmosphere (air), which surround the latter [26]. Commercial leaf sensors are involve phytometric devices that measure the water deficit stress (WDS) by monitoring the moisture level in plant leaves. In recent works [27, 28], a leaf sensor is used to measure the plant's leaf thickness in order to determine the WDS. In the second work, the thickness measurement was taken with a Hall-effect sensor, placed between two magnets. The sensor presented in [27] is provided by AgriHouse Inc. and it costs 290 USD without the wireless communications equipment. It is suitable for real-

time monitoring in aeroponics, hydroponics and drip irrigation systems [29]. In an extreme WDS scenario, the leaf thickness can be decreased dramatically (by as much as 45%) within a short period of time (2 hours). On other occasions, the leaf thickness can be kept fairly constant for several days, but can be decreased substantially when WDS became too severe for the plant [27]. Despite such favourable features, this class of sensors can only be used in controlled environments (i.e., greenhouses) in combination with other type of sensors. This is because a direct relationship seems to exist between leaf thickness and the relative humidity of the ambient air, temperature, soil temperature and soil salinity [27].

Since a major role of transpiration is leaf cooling, canopy temperature and its reduction relative to ambient air temperature is an indication of how capable is transpiration in cooling the leaves [30]. The use of canopy temperature as an indicator of crop water stress has been the subject of much research over the past 30 years. Based on the above, a different type of leaf sensor for WDS monitoring, is described in [26] and is using two temperature sensors. One sensor measures the canopy temperature on the leaf (T_{leaf}) and the other sensor measures the atmospheric temperature (T_{air}). The difference $T_{\text{leaf}} - T_{\text{air}}$ is strictly related to the plant water stress and can be used as decision parameter in a local irrigation system [31]. Canopy temperature and water stress are related: when the soil moisture is reduced, stomatal closure occurs on the leaves resulting to reduced transpirational cooling. The canopy temperature is then increased above that of the air [32]. In a plant with adequate water supply, the term $T_{\text{leaf}} - T_{\text{air}}$ will be zero or negative, but when the available water is limited, the difference will be positive.

The leaf sensors that were described above are different from the well known leaf wetness sensors (LWS). A LWS can detect the leaf wetness which is a meteorological parameter that describes the amount of dew and precipitation left on leaf surfaces. Leaf wetness can be caused by dew, fog, rain or overhead irrigation. Today, the LWS are used most for disease-warning systems [33] and provided by companies like Davis Instruments Inc. or Meter Environment Inc. [34]. For example, PHYTOS31 sensor [34] can monitor the level of surface moisture on foliage, with range from 0 (completely dry) to 15 (saturated). The sensor measures the dielectric constant of the sensor's upper surface, and it can detect the presence of water or ice anywhere

on the sensor's surface.

The agricultural applications frequently involve large, expansive areas where wire connection for communication and power is undesirable or impracticable [22]. The high-cost and the high-power requirements of the today WSN hardware prevent its usage in agriculture. The deployment of these systems therefore relies on reducing the cost to an affordable amount. Capital expenditure relates to the cost of the hardware, which should therefore be maintained minimum. Energy autonomy for the sensor achieved by a combination of minimizing power consumption and harvesting ambient energy is likewise critical in order to reduce operational costs. Above factors drive the demand for low-cost, low-power WSN systems.

Backscatter radio communication in combination with the use of energy assisted (or not) sensor tags is a method that could addresses the aforementioned constraints. It is a very energy-efficient communication technique thus the RF signal is used not only for the communication, but also, for the power of the tag [35]. In the recent literature, backscatter WSNs for smart agriculture purposes [9, 36–38] were proposed. In [9, 36], soil moisture and humidity sensors were proposed. A proof-of-concept demonstration was presented where the tags send measurements to a SDR reader. The WSNs employ semi-passive tags in bistatic topology and each backscatter sensor tag has power consumption of the order of 1 mW. The achieved communication range (tag-reader distance) is of the order of 100 m; this is achieved by supplying the tags with small batteries thereby enabling increased communication range. In [37], electric potential (EP) signals of plants can be measured by the tag in order to estimate when the plant needs water; in that work, the tags are batteryless and they harvest energy from the plant itself. In [38] two UHF RFID sensor nodes for soil moisture sensing were designed based on conventional RFID chips.

This chapter discusses the implementation of a low-cost and low-power wireless sensor system for agricultural applications, which uses a novel plant, backscatter sensor node/tag. Similarly in [39], is presented the same sensing concept based on a commercial RFID chip. The tag is fabricated on polylactic acid (PLA) flexible substrate and was able to operate in semi-active mode, supplied by a flexible solar cell. Preliminary results on this sensor node were proposed in [40]. The tag is connected with a temperature leaf sensor board for WDS measurements and reflects
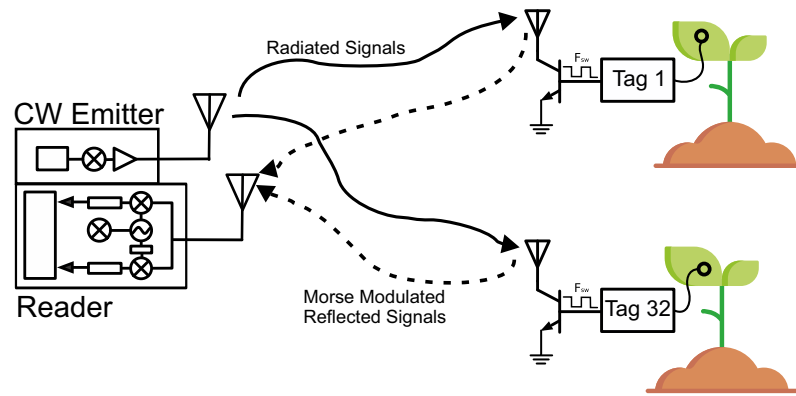
Figure 2.1: Bistatic collocated backscatter communication setup. Plant sensing is achieved by the tags and the information is sent back to a low-cost reader. Information is modulated using Morse coding on a 868 MHz radiated carrier.

RF signals from a carrier emitter. It is noted that the proposed system can be a part of a backscatter WSN, transmitting data to a reader as shown in Fig. 2.1. Specifically the tag architecture consists of a MCU and an external timer for the modulation. There is also a sensor board for the measurements and an FR front-end for the backscatter communication. The tag reads the information from the sensors and generates pulses that control an RF switch. The Morse code was used for the backscatter modulation and to the best of our knowledge, it is the first time that this technique is taken into consideration for a backscatter WSN system. The Morse code was selected due its low-complexity modulation scheme and receiver implementation. It is based on well-known On-Off keying (OOK) modulation which means that a frequency signal exists in only two states either "On" or "Off". Morse code and OOK contribute to architectural and power consumption efficiencies for the tag. A low-cost SDR is used as reader and collects the signals for further processing. The 868 MHz in the European RFID band was selected as carrier emitter frequency.

The structure of the this chapter is as follows: Section 2.3 provides the basic principles of backscatter communication. Section 2.4 describes Morse encoding technique in details. In Section 2.5 the design and the implementation of the tag is described. Section 2.6 discusses the hardware and software part of the low-cost receiver. Section 2.7 presents the proof-of-concept experimental setup and a communication indoor demo. In Section 2.8, the benefits of our proposed low-power WSN and future work are discussed. Finally, section 2.9 includes concluding remarks.
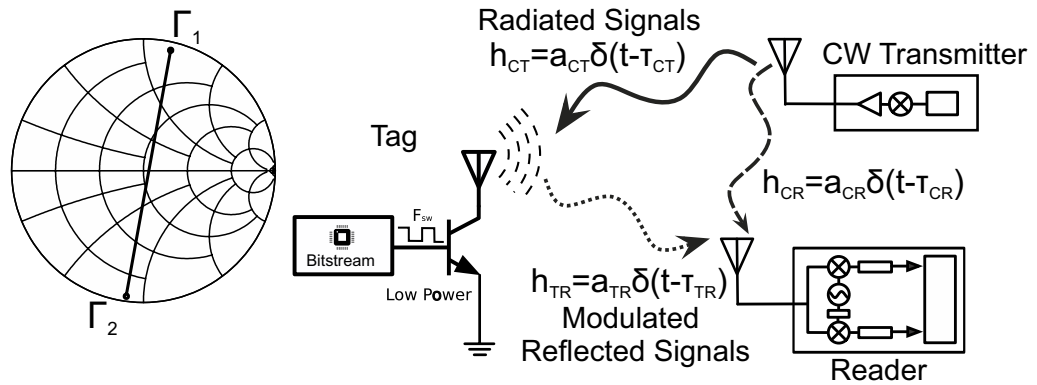
Figure 2.2: Left: Two-state antenna S_{11} parameters on a Smith chart. Right: Bistatic backscatter principle. The emitter transmits a carrier signal and the tag reflects a small amount of the approaching signal back to the reader. The tag modulates the backscattered signal by changing the load connected to its antenna terminals resulting in a Γ_i change between two values (states).

2.3 Backscatter Principles

A general backscatter system can be implemented in a bistatic or monostatic architecture and requires a CW emitter, the tag and a reader. Traditional batteryless RFID systems utilize monostatic architectures were the reader includes the transmitter (CW emitter) and the receiver. The tag receives a CW carrier signal with frequency F_c and scatters a fraction of it back to the reader as shown in Fig. 2.2 (right). It superimposes the sensor information on top of the carrier by appropriately changing the load connected to its antenna terminals according to [41, 42]:

$$\Gamma_i = \frac{Z_i - Z_a^*}{Z_i + Z_a}.$$

(2.1)

with Z_i and Z_a denoting the load and the tag antenna impedance. $(.)^*$ is the complex-conjugate operator and Γ_i is a modified voltage reflection coefficient that reduces to the usual form of transmission-line reflection coefficient when Z_a is real [43]. Typically the antenna impedance is chosen to be 50 Ohm. For binary modulation, the reflected signal is modulated by switching the load between two discrete values (Z_1 and Z_2) effectively resulting in two reflection coefficient values, (Γ_1 and Γ_2) over time. The 180 degrees difference between the two load values (Fig. 2.2, left) is necessary for maximization of backscatter performance. The reader captures the reflected signal at a frequency $f_c + \Delta F$ and an additional phase ϕ and then filters out the high frequency components. ΔF is the carrier frequency offset (CFO) between

the emitter and the reader. According to [8] the received signal can be expressed in the following complex baseband form:

$$y_r(t) = n(t) + \frac{A_c}{2} e^{-j2\pi\Delta F t} \left[\alpha_{\mathrm{CR}} e^{-j\phi_{\mathrm{CR}}} + s\alpha_{\mathrm{CT}}\alpha_{\mathrm{TR}} e^{-j\phi_{\mathrm{CTR}}} \Gamma(t - \tau_{\mathrm{TR}}) \right], \qquad (2.2)$$

where A_c is the carrier amplitude, $\alpha_{\mathrm{CR}}, \alpha_{\mathrm{CT}}, \alpha_{\mathrm{TR}} \in \mathbb{R}$ and $\phi_{\mathrm{CR}}, \phi_{\mathrm{CTR}} \in [0, 2\pi)$. Moreover τ_{TR} is the time delay constant of the tag-reader channel. Term s is related to the tag scattering efficiency and tag antenna gain at a given direction. The term $\alpha_{\mathrm{CR}} e^{j\phi_{\mathrm{CR}}}$ defines the component which depends on the emitter-to-reader channel (h_{CR} in Fig. 2.2). The tag signal is a direct function of Γ over time and the term $\alpha_{\mathrm{CT}}\alpha_{\mathrm{TR}} e^{j\phi_{\mathrm{CTR}}}$ scales and rotates the modulated part of the tag signal. This term depends on the transmitter-to-tag and tag-to-reader channel parameters (h_{CT} and h_{TR} in Fig. 2.2). Finally, $n(t)$ is the complex thermal Gaussian noise at the receiver.
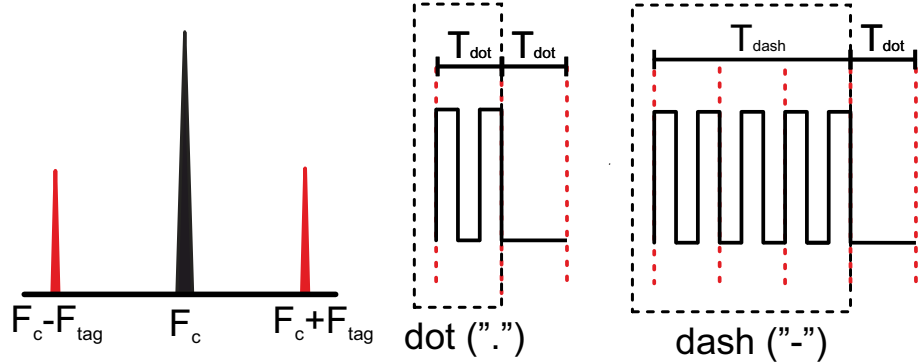
Figure 2.3: Left: In Backscatter principle when a F_c carrier exists and the RF switch frequency is F_{tag}, two subcarriers appear with frequencies $Fc \pm F_{\mathrm{tag}}$. Right: Morse code symbols.

In this work dislocated bistatic architecture is employed [42]; the emitter transmits a CW signal at frequency $F_c = 868$ MHz. The tag receives and scatters a fraction of it back to the reader as shown in Fig. 2.2. The backscatter binary communication can be implemented on the tag using an RF switch, an antenna and a control unit. The switch alternates the load of the antenna between two values $Z_{1/2}$ and offers two reflection coefficients, $\Gamma_{1/2}$. When the CW with frequency F_c arrives on the antenna and the RF switch frequency is F_{tag}, frequency modulation occurs and two subcarriers appear in the spectrum with frequencies $F_{\mathrm{sub1/2}} = F_c \pm F_{\mathrm{tag}}$. The reflected signal (subcarriers) and the carrier are depicted in Fig. 2.3 (left). The subcarriers are next modulated using the Morse code scheme as it is described in

the next section.

2.4   Morse Encoding

Morse code is a method of transmitting text information as a series of On-Off tones, named after the inventor of the telegraph Samuel F. B. Morse in the 1830s [44]. It is referred as the earliest type of binary digital communications since the code is made solely from ones and zeros ("On" and "Off"). In modern times Morse code is still used widely in amateur radio communications, as Morse coded signals can get a message through noise, whereas a voice signal often cannot. Each letter of the alphabet is translated to combinations of dots "." and dashes "-" that are sent over telegraph wires or by radio waves from one place to another. For example, the letter "A" is translated to the sequence ".-" with elements one dot and one dash symbol. Lets assume that the duration of a dot (T_{dot}) is one unit, then the duration a dash is three units ($3T_{dot}$). Dot and dash symbols are followed by a short silence, equal to one unit (Fig. 2.3, right). The space between the elements of one letter/character is one unit, between characters is three units and between words, seven units.

The Morse code is the only digital modulation designed to be easily read without a computer. Today it is usually used by radio amateurs and it is the fist time that is used in backscatter communication. The OOK modulation is used to transmit Morse code signals over a fixed radio frequency. The OOK is a simplest form of ASK modulation that can represent digital data using a presence ("On") or an absence ("Off") of a carrier signal. With OOK modulation and thus Morse code, the complexity of the receiver and the tag is drastically simplified compared to a FM scheme thus there is no need for a different frequency for each symbol [45]. Also, Morse code was designed so that the most frequently used letters have the shortest codes. In general, code length increases as frequency decreases.

In this work, the "." (dot of Morse code) is implemented as a signal with a specific duration T_{dot} and frequency F_{tag}. As it is expected, the "-" (dash in Morse code) is implemented using a frequency signal with three times the duration of the dot signal. The T_{dot} value is defined by the MCU and the F_{tag} value is defined by the external timer of the tag. The dot and dash frequency signals are shown in Fig. 2.3
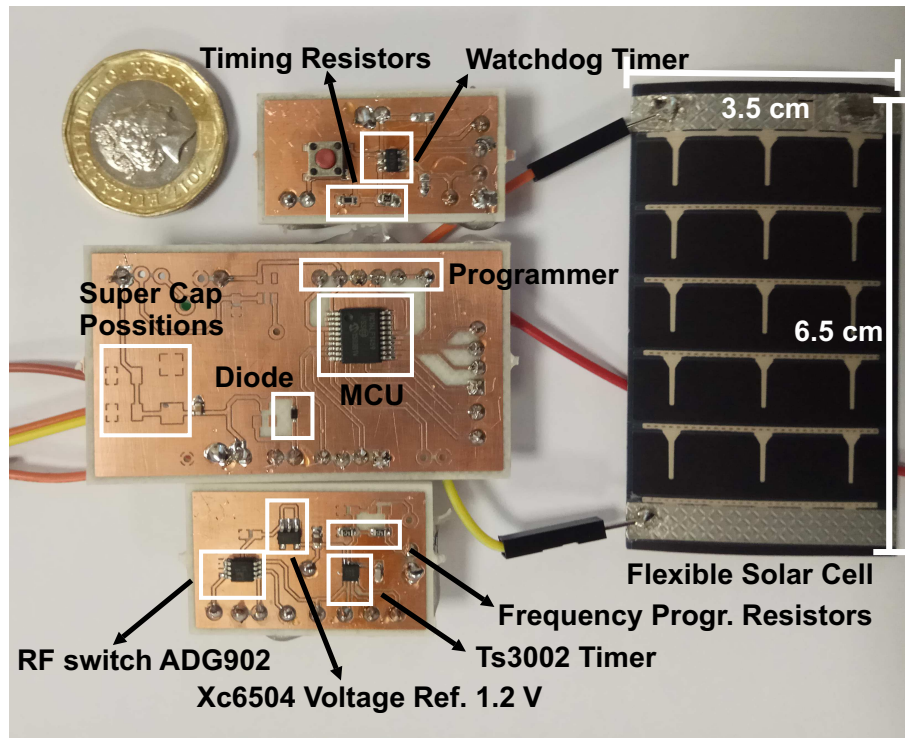
Figure 2.4: Printed circuit boards of the tag and the solar cell. The watchdog timer (top) and the timer module (bottom) are connected with the main processor unit in the middle.

(left). The speed of Morse code is stated in words per minute (WPM) and according to the standards, the word PARIS is used to determine it. The word is translated to exactly 50 units and one dot duration is defined by the formula: $T_{\mathrm{dot}} = 1200/\mathrm{WPM}$ with T_{dot} in ms.

2.5 Tag Implementation

2.5.1 Main Unit

Our proof-of-concept tag consists of five different parts implemented in different printed circuit boards (PCBs) for simplifying debugging. These parts are a MCU unit, a timer part, a watchdog timer part, a sensor board, and finally an RF front-end. The MCU unit (Fig. 2.4, middle board) is the main part of the system and it is responsible for the sensor-data acquisition, the implementation of the Morse code symbols and the control of all the other parts. The schematic of the main system is depicted in Fig. 2.5. The ultra-low-power 8-bit PIC16LF1459 from Microchip Inc. with current consumption of only 25 μA/MHz at 1.8 V [46] was selected for
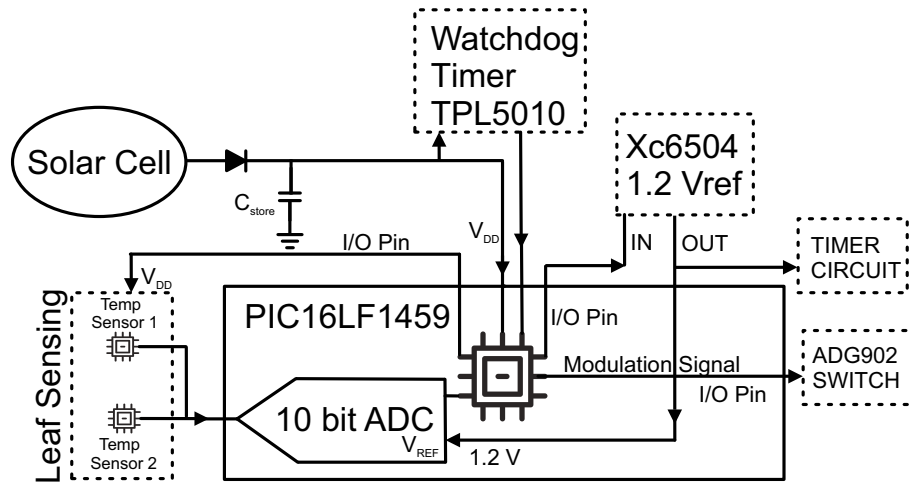
Figure 2.5: The schematic of the tag's main unit. The main part, is a low-power microcontroller (MCU) that controls the sensors, the timer and the RF front-end.

the MCU. In sleep mode, the MCU current consumption was only 0.6 μA at 1.8 V. The MCU collects data from the sensor board using the internal ADC with 10-bit resolution. The internal 31 kHz low-power oscillator was utilized as clock source in order to reduce the power consumption of the tag. The MCU contains also a DAC with 5-bit resolution and is responsible to supply all the parts of the tag with voltage when it is necessary. The main part is connected with a μW timer for the subcarrier signal (F_{tag}) production and an external watchdog timer to wake up the MCU from the "sleep" operation mode.

2.5.2 Timer Modules

The timer module (Fig. 2.4, bottom) consists of a very low-power timer (TS3002), a voltage reference and a switch. It is responsible for producing the subcarrier frequency of the tag F_{tag} and modulating this subcarrier through the switch. The low-power single-pole, single-throw (SPST) switch ADG902 was used in this case and one of the MCU input/output (I/O) pins was programmed to provide the necessary Morse code pulses for the control. The implemented circuit is depicted in Fig. 2.6. The TS3002 is a CMOS oscillator provided by Silicon Labs Inc., fully specified to operate at around 1 V and to consume current lower than 5 μA with an output frequency range from 5.2 kHz to 290 kHz [47]. The timer was supplied by a voltage reference integrated circuit (IC) XC6504 at 1.2 V [48] in order to reduce the power consumption. XC6504 provides also stable reference voltage at the ADC of the
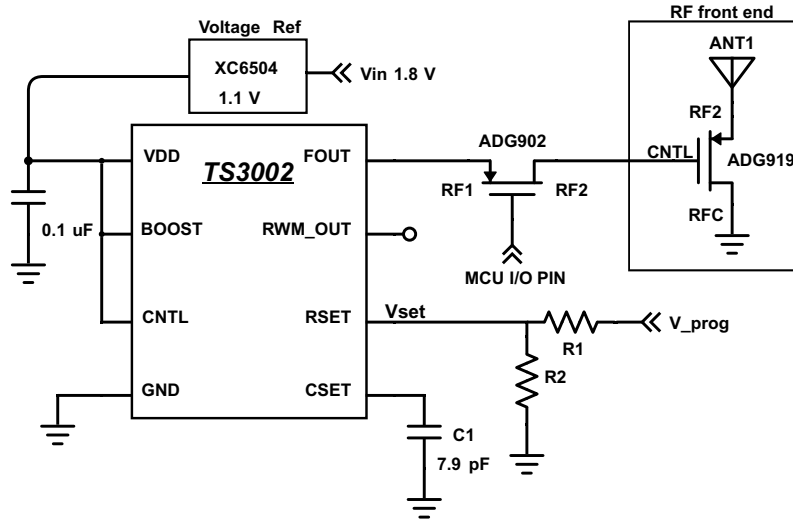
Figure 2.6: Timer and RF front-end schematic of the tag. The timer produces square wave pulses with 50% duty circle and supplies the RF front-end through a modulation switch (ADG902). The ADG902 switch is controlled by the MCU.

tag and it is activated by an I/O pin of MCU. The output frequency of the timer is programmed by using two parallel external resistors, a capacitor and a voltage value. The square wave pulses have 50 % duty cycle and the maximum oscillation frequency when a zero voltage is applied at V_{prog}, is given by:

$$F_{tag,max} = \frac{1}{1.19 C_1 R_{set}},$$ (2.3)

with $R_{set} = R_1 R_2 / (R_1 + R_2)$. In our proof-of-concept prototype two identical resistors were used with value of 6.2 MOhm and tolerance 1% in order to avoid the frequency jitter. The output frequency was programmed to 34.3 kHz and the power consumption of the timer circuit was measured at 2.62 μW (1.8 V). Is is noticed that the above measurement includes the power consumption of the voltage reference IC. The timer module was fabricated in a separate PCB for debug purposes and is depicted in Fig. 2.4 (bottom). The TS3002 can be configured as a voltage-controlled oscillator (VCO) by applying a positive voltage value at V_{prog} terminal and the F_{tag} frequency is defined as [49]:

$$F_{tag} = V_{prog} \frac{-F_{tag,max}}{V_{prog,max}} + F_{tag,max},$$ (2.4)
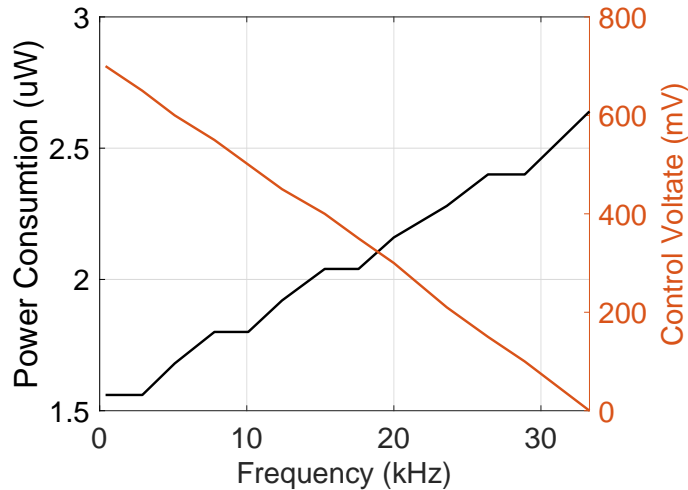
Figure 2.7: Power consumption of the TS3002 timer versus the output frequency (F_{tag}) versus the control voltage V_{prog}.

with $V_{\text{prog,max}}$, the maximum value of V_{prog} when the timer gives zero frequency at its output. In Fig. 2.7, it is shown the ultra-low-power consumption of the timer versus different frequencies at the output. Each frequency value corresponds to a different control voltage (V_{prog}).

In case of a multiple access scheme, we have multiple tags in the same network sending information simultaneously. Each tag must operate in different F_{tag} frequency and the embedded DAC could be used in order to tune every tag in different subcarrier. The DAC can supply the timer with 2^5 distinct voltage levels (V_{prog}) corresponding to 32 distinct subcarriers resulting in 32 tags in the same network. In this work the DAC is not used in order to reduce the overall power consumption of the prototype tag. The subcarrier frequency was programmed manually by using only the two resistors. V_{prog} terminal was connected to the ground.

A duty cycle operation of the tag was programmed for minimization of the average power consumption. The tag was active only for a desired minimum period of time and a watchdog timer was used as a real-time clock (RTC). Specifically, the nano power TPL5010 timer from Texas Instruments [50] was utilized, which consumes only 35 nA. The TPL5010 can work as RTC and allows the MCU to be placed in sleep mode. It can provide an interrupt signal in selectable timing intervals from 0.1 to 7200 s by programming two external parallel resistors. It was programmed to wake up the MCU every 4 s activating the duty cycle operation of the system. The
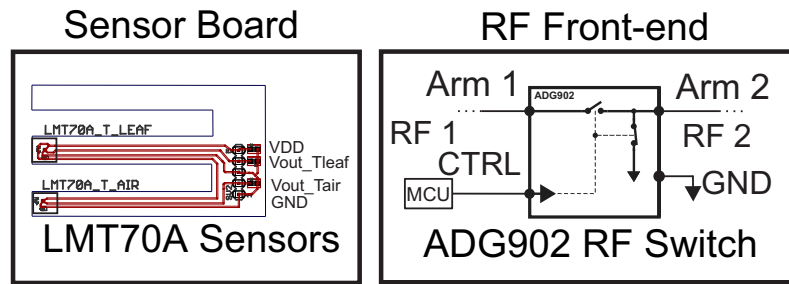
Figure 2.8: Left: Sensor board schematic with low power LMT70A sensors in Clothes-pin design. Right: ADG902 RF switch schematic.
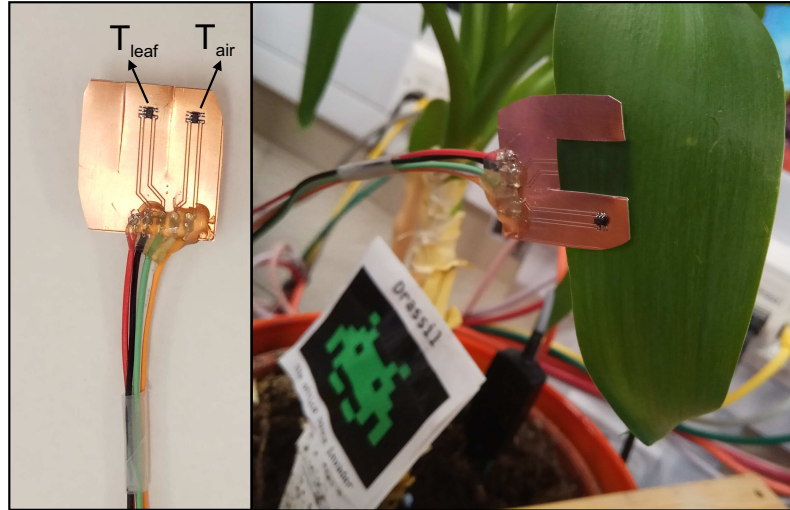
Figure 2.9: Printed circuit board with low-power LMT84 temperature sensors. The sensor board can be placed easily on a leaf.

PCB of the watchdog timer is shown in Fig. 2.4 (top).

2.5.3 Sensor Board

The sensor board consists of two analog temperature sensors "LMT84" by Texas Instruments (Fig. 2.9, left). Each sensor is connected with an ADC input and consumes 5.4 μA at 1.8 V [51]. The accuracy of each one is $\pm 0.4°C$, while both were placed on a "clip" scheme board in order to be easily mounted on a leaf. The prototype placed and on a leaf and the schematic of the sensors board, are depicted in Fig. 2.9 and Fig. 2.8 (Left), respectively. The temperature sensor seen on the top measures the air temperature (T_{air}), while a similar sensor under the leaf surface is placed in direct contact with the leaf and measures the canopy temperature T_{leaf}.
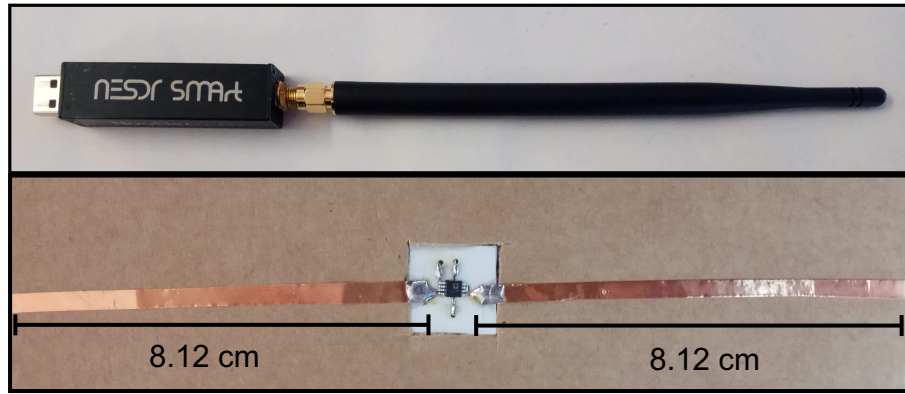
Figure 2.10: Top: Low-cost software-defined radio. Bottom: RF front-end board with ADG919 switch.

The transfer function of the each sensor is defined as [51]:

$$T_{\text{leaf/air}} = \frac{5.506 - \sqrt{36.445 - 0.00704V_{\text{leaf/air}}}}{-0.00352} + 30, \tag{2.5}$$

where $V_{\text{leaf/air}}$ is the ADC value in mV and $T_{\text{leaf/air}}$ is temperature in $°C$. The MCU collects data from sensors one by one in order to minimize the instantaneous power consumption. The two ADC measurements were encoded using the Morse code and were sent back to the receiver. At the receiver, the signal from both sensors is decoded in terms of a voltage value (mV) and the temperature is then calculated using the (2.5). Subsequently, the temperature difference $T_{\text{leaf}} - T_{\text{air}}$ is estimated and recorded.

2.5.4 RF Front-end

The RF front-end part consists of an RF switch and a custom dipole antenna as it is depicted in Fig. 2.10 (bottom). The schematic of the board is shown in Fig. 2.8 (Right). The RF front-end is connected to the ADG902 switch of the timer module (Fig. 2.6). It is used for the wireless communication with the reader and it it responsible for creating the reflections of the incident CW signal. The single-pole, double-throw (SPDT) switch ADG919 [52] was selected due to its low insertion loss and high "OFF" isolation. The "RFC" and the "RF2" terminals of the RF switch were connected to the two arms of dipole antenna. The antenna was connected directly with the RF switch without any connector in order to avoid the extra losses. The dipole antenna has omnidirectional attributes at the vertical to its axis level
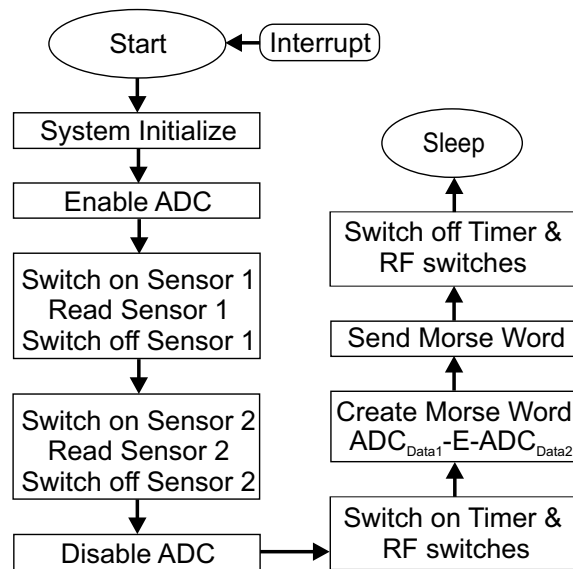
Figure 2.11: Flow chart of the tag algorithm. This algorithm was implemented in the MCU and controls all the peripherals of the tag.

and was designed for operation at 868 MHz. The bottom picture of Fig. 2.10 shows the fabricated prototype and the dimensions of the antenna. The RF front-end was fabricated using copper tape on cardboard substrate.

2.5.5 Tag Analysis

In this work a solar panel harvester was employed for powering the tag. Solar energy could be used to power the tag also in combination with other energy harvesting technologies [53]. This solar module is the flexible, thin-film SP3-37 provided by PowerFilm Inc. [54]. The solar panel charges a 11 mF super capacitor (CPH3225A) instead of a battery through a low voltage drop Schottky diode. For the diode, the SMS7630-079LF by Skyworks Inc. with forward voltage drop only 150 mV was selected. The solar panel, the diode and the capacitor positions are depicted in Fig. 2.4.

On the tag, a real-time algorithm was implemented in order to read the sensor information and wirelessly transmit it to the receiver. The steps of the algorithm are shown in Fig. 2.11. Initially, an interrupt signal coming from the watchdog timer is used to wake up the MCU. Next, initialization of the system (ADC, clock, I/O pins) is achieved and the ADC is enabled for data capture. The temperature sensors are consecutively powered and the ADC reads the data from each one. The ADC
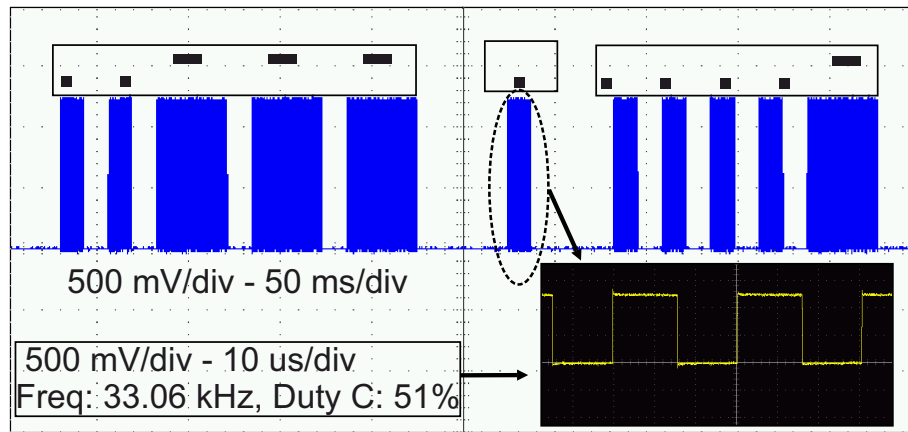
Figure 2.12: Oscilloscope measurement of a Morse coded word: ". . - - -   .   . . . . -" corresponding to "2**E**4" word. This square wave signal is used to control the RF front-end.

is turned off immediately after this action for reducing the energy consumption. In the next step, the TS3002 timer and the ADG902/919 switches are switched on two steps before the data sending. This is necessary for the frequency stabilization of the timer. The tag was programmed to send a Morse coded word with fixed format every time the algorithm is running. The format of the word was defined as "ADC_{DATA1}**E**ADC_{DATA2}" with ADC_{DATA1}, ADC_{DATA2}, the ADC values, varied for 0 to 1023. The sensor data were separated by the letter "E" and without any spaces between them. The goal was to create a short word to minimize the transmission time and thus the energy consumption. The letter "E" is the most common letter in English alphabet and has the shortest code, a single dot. The word is then translated in dots and dashes using the frequency F_{tag} of the timer and baseband pulses coming from the MCU.

The MCU produces baseband pulses that contain the dots, dashes and the spaces between them. This signal is coming from an I/O pin and is used to modulate the timer's frequency signal through the ADG902 switch. In Fig. 2.12 an oscilloscope measurement of a modulated example signal at the output of ADG902 switch is shown. The word of "2**E**4" was selected as an example and it is translated in ". . - - -   .   . . . . -", while each dot/dash is a 33 kHz signal with different duration. The required spaces between the Morse code symbols can also be observed. In order to send this word wirelessly, the RF switch ADG919 is fed with this signal and the incident CW carrier is modulated again by the tag information. In the last step

23

of the algorithm, the switches and the timer were switched off and the tag goes to sleep mode. The time duration of the algorithm depends from the ADC data and the worst-case scenario is the word "1023**E**1023". This is because the ADC has 10 resolution and the measurement varies from 0 to 1023 value. In that case the duration of the whole process lasts 2.8 s assuming 104.3 WPM speed.

2.6   Receiver

2.6.1   Software-Defined Radio

In our system the temperature ADC data are received by a low-cost SDR. This receiver is the "NESDR SMArt" SDR available by the NooElec Inc. (Fig. 2.10, top) [55]. It is an improved version of classic RTL SDR dongle based on the same RTL2832U demodulator with universal serial bus (USB) interface and R820T2 tuner. The new version provides a better oscillator, temperature stability and antenna improvements compared to the old one. It comes with an ultra-low phase noise 0.5 PPM temperature compensated crystal oscillator (Phase noise @100 KHz: -152 dBc/Hz). The dongle was redesigned with an RF-suitable voltage regulator with under 10 μVRMS of noise for lower power consumption. Power consumption has been reduced by an average of 10 mA according to manufacturer [55]. A custom heatsink is affixed to the primary PCB for temperature improvement and it comes with a low-loss RG58 feed cable and SubMiniature version A (SMA) antenna connector for better signal reception. The tuning frequency range varies from 24 MHz to 1850 MHz with sampling rate up to 2.8 MS/s and noise figure about 3.5 dB. Gain control is also provided through the embedded low noise amplifier (LNA) at the input of R820T2, while at the output through a variable gain amplifier. It down-converts the received RF signal to baseband and it sends real (I) and imaginary (Q) signal samples to a computer through the USB interface. All the above parameters make it suitable for our application also noting that the required sampling rate is quite low (250 kS/s) and it costs only 12.8 GBP. The receiver was connected with a 868 MHz monopole antenna to receive the signals from the tag.
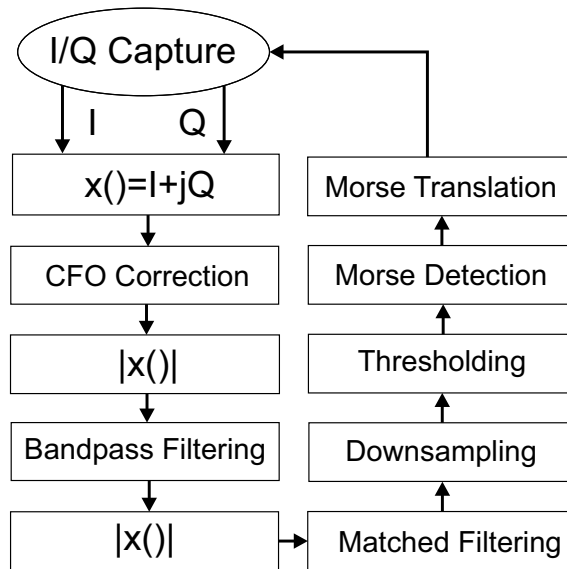
Figure 2.13: Flow chart of the real-time receiver algorithm. The decoding algorithm was implemented in MATLAB software.

2.6.2 Receiver Algorithm

A real-time algorithm was implemented in MATLAB software in order to detect the reflected signals. The implemented algorithm is available in Appendix A.1. The SDR can be connected with MATLAB through the open course GNU radio framework [56]. In the algorithm, the subcarrier frequency F_{tag} of the tag is known and the algorithm collects data in a window with duration: 2×length(maximum word). As shown in Fig. 2.13, the received I and Q digitized samples were combined together in complex numbers. CFO was estimated and the signal was corrected. This accounts for the difference in carrier frequency between the SDR and the emitter, providing the variance between the real values and the estimated values of the subcarrier signal. The CFO was estimated after the samples were collected and then all samples were frequency shifted accordingly. The absolute value is taken and a bandpass filter with center frequency F_{tag} is applied in order to appear the Morse code word. After considering the signal magnitude, a matched filter was applied to appear the baseband Mode symbols. The matched filter is a square pulse with duration T_{dot}. The received signal of the Fig. 2.12 word is shown in Fig. 2.14, (a) after the band-pass filtering. In Fig. 2.14, (b) is shown the above signal after matched filtering. The matched filtering was followed by downsampling with a factor of 100 for reducing of the computational complexity. Next, the received signal must
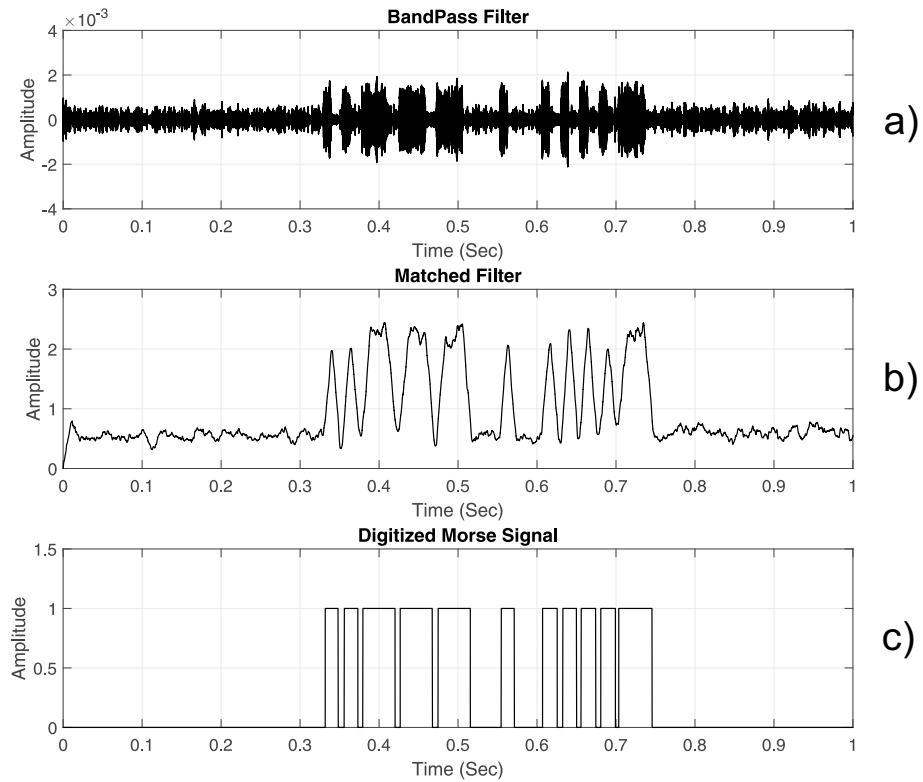
Figure 2.14: A received signal including a Morse coded word in three different steps of decoding algorithm.

be digitized using a threshold level. Automatic gain control (AGC) and threshold decision is needed because the signal strength varies over time. The digitization procedure, which is using a suitable threshold, is depicted in Fig. 2.14, (c). The digitized signal was classified in order to detect the Morse code symbols and thus the alphabet characters. For the classification, a group of tokens was used with each token to be an English alphabet character translated in dots and dashes. The output of the algorithm is the English text and number representation of the Morse word.

2.7 Experimental Results

The proof-of-concept system was tested indoors in a setup depicted in Fig. 2.15 in order to validate the effectiveness of our backscatter communication system. The emitter, the tag and the reader were tested in dislocated bistatic architecture in Heriot-Watt University electromagnetic lab [42]. A signal generator with a monopole antenna was utilized as the CW emitter at 868 MHz, with a transmission
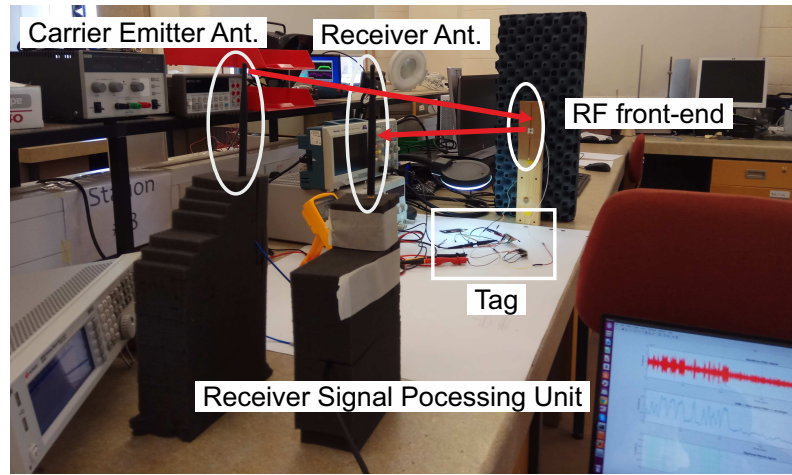
Figure 2.15: Experimental indoor backscatter topology. The tag was measured in dislocated bistatic architecture 2 m away from emitter and receiver antennas.

power of 13 dBm. The SDR reader was used as the software-defined receiver in the same position with the emitter. The receiver was tuned to 868 MHz with sampling rate 250 kbps. The distance between the reader and emitter antenna was fixed at 17.27 cm ($\lambda/2$). The tag was placed 2 m away from the emitter/reader antennas and was programmed to produce words with Morse code symbols. Each word contains the T_{leaf} and T_{air} values in mV at 104.3 WPM speed. The sensor node has low-power consumption and was supplied by the solar panel and the super capacitor. An office lamb was used as an indoor source of light. Results shown that the transmitted words can be presented clearly at the receiver.

Table 2.1 provides cost of the most significant components of the tag and the current consumption of each one. In active mode, the maximum overall dissipated current at 1.8 V was measured 11.5 μA (20.7 μW) when the ADC was off and 201 μA (362 μW) when the ADC was active. In the sleep mode operation the current consumption was 0.6 μA (1 μW). Finally, using discrete electronic components in terms of bill of materials (BOM), the tag results in the cost of 14.1 GBP and the prices of each component were found from online suppliers on the order of one. Looking at the market, we found only one leaf sensor provided by Agrihouse Inc. It costs 290 USD without the wireless communication equipment and according to the above, this work seems to be a promising low-cost alternative solution in order to monitor the WDS of the plans.

Table 2.1: Tag Current Consumption & Cost Analysis

Tag Part	Cost (GBP)	Current (μA)
MCU (PIC16F1459)	1.44	-
ACTIVE MODE (ADC OFF)	-	3.3 @$V_{\mathrm{DD}} = 1.8$ V
ACTIVE MODE (ADC ON)	-	198.4 @$V_{\mathrm{DD}} = 1.8$ V
SLEEP MODE	-	0.6 @$V_{\mathrm{DD}} = 1.8$ V
Timer (TS3002)	0.54	2.2 @$V_{\mathrm{DD}} = 1.2$ V
Voltage Reference (XC6504)	0.42	0.6 @$V_{\mathrm{DD}} = 1.8$ V
Watchdog timer (TPL5010)	0.93	0.035 @$V_{\mathrm{DD}} = 1.8$ V
RF Switches (ADG902+ADG919)	2.39 + 2.49	0.1 @$V_{\mathrm{DD}} = 1.8$ V
Temp Sensors (2×LMT84)	0.64 + 0.64	5.3 @$V_{\mathrm{DD}} = 1.8$ V
Super Cap (CPH3225A)	2.05	-
Solar Panel (SP3-37)	2.20	-
Sum	14.16	-
Sum ACTIVE MODE (ADC OFF)	-	11.5 @$V_{\mathrm{DD}} = 1.8$ V
Sum ACTIVE MODE (ADC ON)	-	201 @$V_{\mathrm{DD}} = 1.8$ V
Sum SLEEP MODE	-	0.6 @$V_{\mathrm{DD}} = 1.8$ V

2.8   System Considerations

The architecture of the proposed WSN could include many low-cost emitters/readers, installed in a field and around them, multiple, backscatter sensors can be spread. For example, multiple carrier emitters can be placed around a central reader and around them, could be placed multiple low-power and low-cost tags. Carrier emitters can be simple devices that comprise of an oscillator and a power amplifier while the reader can be implemented in a commodity software- defined radio (SDR) device. Working in cells that contain groups of tags, each tag can backscatter information to the receiver at a specific subcarrier frequency. The tags inside each cell will employ frequency-division-multiple-access (FDMA) scheme, whereas the emitters/readers could operate in a time-division-multiple-access (TDMA) scheme. Using the above concept the development of a backscatter sensor network, could include hundreds of low-cost tags.

The classic WSN nodes utilize duty cycling operation in order to decrease the power consumption thus extending WSN lifetime. In this work, the tag was designed such that as low as possible power and the utilization of duty cycling could further decrease the required energy requirements. In [36] was demonstrated that the power

consumption of a similar proposed backscatter WSN is lower than a ZigBee-type WSN. ZigBee sensors are based on IEEE 802.15.4 communication protocol and are widespread for wireless area networks with small digital radios [57].

The communication range of our proposed deployment can be extended by the following modifications. First, it is possible to use circular polarized and directive antennas instead on the monopoles at the reader and the emitter. The antennas would be designed and fabricated on the same substrate with a proper distance between them in order to maximize gain and keep mutual coupling between them at low level. With circular polarization the alignment between the reader/emitter antenna and the tag will have less effect. Secondly, the RF front-end dipole antenna could be replaced with a better gain antenna. This work is a first attempt to design a low-cost and low-power leaf sensor for agriculture and specific sensing plant measurements will be prepared in the future. The proposed sensor must be calibrated for different values on relative humidity and soil moisture for a specific type of plant. Finally, the cost of the tag can be reduced by replacement of the super capacitor and the solar panel with a cheaper option.

2.9 Conclusion

In this chapter a novel backscatter leaf sensing system for agricultural purposes was presented. Specifically, it includes a sensor for leaf canopy temperature measurements and it can be used for water stress measurements on plants. The sensor node has low-power consumption of only 20 μW and it was supplied by a solar panel without need of battery. Morse code modulation was used for the wireless communication with a low-cost SDR receiver by backscattering RF signals from a carrier emitter. The proposed system is part of the backscatter WSN for agriculture with a small cost per sensor node. It is suitable for distributed monitoring of environmental parameters in large scale, precision agriculture applications.

Chapter 3

Spread Spectrum Backscatter

3.1 Introduction

Nowadays there is a plethora of wireless communication protocols, including short-range radio protocols such as ZigBee, Bluetooth/Bluetooth low energy (BLE), Wi-Fi/Wi-Fi HaLow or RFID; mobile networks and longer-range radio protocols such as LoRaWAN, SigFox54, NarrowBand-IoT (NB-IoT), or long-term evolution (LTE)-M. Each of them is defined in its own standard, for example ZigBee and ZigBee 3.0 are based on IEEE 802.15.4. Wireless technologies have different characteristics, such as a specific signal range, bandwidth, etc. and can be classified as wireless local area networks (WLAN), wireless wide area networks (WWAN) or low-power wide area networks (LPWANs). The vast majority of the connected things at the moment use IEEE 802.15.4-based systems, in particular ZigBee. The most prominent features of these networks are that they operate mainly in the 2.4 GHz and optionally in the 868/915 MHz unlicensed frequency bands.

Table 3.1: IoT Technologies in Europe

Technology	Sensitivity (dBm)	Frequency	Bit Rate
LoRa	-137	865-868 MHz	0.3-27 Kbps
NB-IoT (NB20)	-129	971-821 MHz	0.6-200 Kbps
Sigfox	-126	868 MHz	100 bps
ZigBee	-125	865-868 MHz	250 Kbps
Bluetooth	-97	2.4 GHz	1-2 Mbps
Wi-Fi	-95	2.4/5 GHz	1-300 Mbps
RFID	-22	865-868 MHz	27-128 Kbps

Table 3.1 lists the most common technologies used in IoT applications in Europe, with their respective sensitivities and data rates. The sensitivity of the technology largely determines the range at which a device can communicate. The nominal sensitivity of ZigBee and Bluetooth receivers is around –125 dBm and –97 dBm with 250 kbps in ZigBee and 1–2 Mbps in Bluetooth, respectively. The SIGFOX physical layer employs ultra narrowband (UNB) PSK wireless modulation with a coverage area of 30–50 km in rural areas and 3–10 km in urban areas [58] with a maximum throughput of only 100 bps. NB-IoT is a Narrow Band IoT technology that is designed for connecting a wide range of static IoT devices using current cellular communication bands and infrastructures. It can coexist with global system mobile (GSM) communications and LTE under licensed frequency bands of $700, 800$ and 900 MHz. Sigfox operates in the UHF band and uses PSK modulation to transmit data at very low data rates, thus achieving long range.

LoRa is a new physical layer LPWAN solution, designed and patented by Semtech Corporation. The technology employs a chirp spread spectrum (CSS) techniques and uses the linear frequency modulated signals (chirps) with cyclic shifts to encode information. The chirp's frequency sweep is equivalent to the spectral bandwidth of the signal. In the LORA protocol, a symbol (chirp) is encoded in a longer sequence of bits, thus reducing the signal-to-noise-plus-interference ratio required at the receiver for correct reception, without changing the frequency bandwidth of the wireless signal. In CSS modulation, 0 bit could be represented as a continuous chirp that increases linearly with frequency, while the 1 bit could be a chirp that is cyclically shifted in time. The length of the spreading code is equal to 2^{SF}, where SF is a tunable parameter, called spreading factor. SF can be varied from 7 up to 12, thus making it possible to provide variable data rates, giving the possibility to trade throughput for coverage range, link robustness or energy consumption. The LoRa data rate is between 300 bps and 27 kbps depending on spreading factor and channel bandwidth.

The communication in LoRaWAN always begins with (uplink) messages sent by the end-device and it specifies if it is a confirmed or unconfirmed message. In the case that the end-device specifies that it is a confirmed message, then the gateway shall downlink an acknowledgement. If an unconfirmed message was set by the end-

device, then no acknowledgement will be needed [59]. In fact, the gateway does not need to downlink any message. This is particular convenient for situations where the end-devices are very low power and read-only devices, such as sensors. This optional acknowledgement is also suitable for LoRaWAN since the transmit time of the end-devices is limited, and a certain amount of packet-loss is allowable.

Figure 3.1: Agricultural backscatter communication setup in bistatic architecture. An emitter sends a pure carrier signal and a reader receives the modulated reflections of each tag. The tags could be embedded on leaf sensors for precise water stress monitoring.

While backscatter principles have been restricted to communication ranges of up several meters; there is a challenge and a necessity how to increase the emitter-to-tag and tag-to-reader ranges. In order to address the short range problem, the WSN must utilize bistatic topology and semi-passive (i.e., battery-assisted) tags. Also in order to increase the receiver sensitivity and thus the range, conventional embedded radios could be used as low-cost receivers or emitters (Fig. 3.1). In [60] it is shown that using a commercial FSK transceiver and 13 dBm emitter transmission power, 246 meters tag-to-reader distance is possible. A set of 1000 packets was transmitted per measurement and a packet was transmitted every 500 ms. At 246 meters tag-to-reader distance, the packet error rate (PER) was less than 1%, while 268 meters are possible at the expense of increased PER, in the order of 10%. The Silicon Laboratories SI1064 ultra-low power MCU with integrated transceiver was configured as receiver using the binary FSK-modulation.

Some recent studies implemented a backscatter modulator that can be compatible with LoRa hardware, and extend significantly the range of communication

[61, 62]. The implementation can synthesize LoRa symbols, but has very low data rates which limits the scalability of the technology for other applications. In [61] they showed that can be achieved reliable coverage in a one-acre (4046 m^2) farm using only one emitter and receiver. Their backscatter device is co-located with the RF source with distance 5 m, and the receiver can be as far as 2.8 km away. They presented a simulation design of a LoRa backscatter chip that consumes only 9.25 μW of power, which is more than 1000x lower power than LoRa radio chipsets. The implementation can synthesize LoRa symbols by using three cascaded switches that create eight different impedances corresponding to eight different reflected phases, which constraints the implementation in terms of scalability. Due to the unavoidable harmonic content generated, in the same work, the authors also presented a harmonic cancellation technique that fairly mitigates the problem but, however, it increases the complexity of the system.

In [62], the authors have a design called PLoRa that takes ambient LoRa transmissions as the excitation signals, conveys data by modulating an excitation signal into a new standard LoRa chirp signal. They shift this new signal (by an amount of $BW/2$ and -$BW/2$) to a different LoRa channel to be received at a gateway faraway. They demonstrated a prototype tag that can backscatter an ambient LoRa transmission sent from a nearby LoRa node (20 cm away) to a gateway up to 1.1 km away, and deliver 284 bytes data every 24 minutes indoors, or every 17 minutes outdoors. They also simulated a 28-nm low-power FPGA based prototype whose digital baseband processor achieves 220 μW power consumption. This implementation is entirely dependent on LoRa communications, since it uses FSK modulation with an active LoRa chirp. Moreover, the achievable data rate is lower than the LoRa, since the design can only encode one bit per active LoRa symbol.

This chapter is an extended version of the work presented in [63], where preliminary results of an IQ backscatter modulator shown to be able to synthesize an up-chirp, which is used in the LoRa's packets preamble. A LoRa encoder and decoder was also developed in order to prove that the proposed circuit can generate any LoRa symbol, proving that it may be compatible with current LoRa gateways or networks. It is also shown that it is scalable for other types of applications due to its simple implementation and versatility for different frequencies. Measurements

of the BER versus SNR are provided as well as several measurements Over-the-air (OtA) with different propagation scenarios. Additionally, the robustness of the proposed design is evaluated when the control bias voltages are corrupted with specific perturbations. The modulator consists of only two transistors and a power divider and has negligible dc power consumption. The overall dc power consumption will be determined by the processing unit, which is intended to operate in baseband and to be as low power as possible, ideally battery-less and wirelessly powered. This allows to integrate this technology into domains such as smart cities, precision agriculture and many other applications where backscatter is currently unfeasible due to the short covering range. By developing the system for 2.45 GHz, it is possible to use Wi-Fi or 802.15.4 devices to generate the backscatter carrier, since most of those radio transceivers provide access to a special test mode that generates an unmodulated carrier signal [64].

The structure of the chapter is as follows: Section 3.2 provides information about the LoRa telecommunication protocol. Section 3.3 describes the design and implementation of the proposed IQ modulator. Section 3.4 shows how the symbols are translated to chirp signals and the decoding procedure. Section 3.5 presents proof-of-concept experimental results using a measurements setup with cables and without them. Finally, section 3.6 includes concluding remarks.

3.2   LoRa Modulation & Demodulation

This section provides an overview of the Semtech's LoRa modulation, which is used to provide long range communications [65]. LoRa is a modulation technique based on CSS and it uses linear frequency modulated CW signals with cyclic shifts to encode data [66]. The bit rate achieved by such technique is given by:

$$R_{\text{Lora}} = SF\frac{BW}{2^{SF}}, \tag{3.1}$$

where BW is the bandwidth of the signal. The SF relates to the number of chips (steps/frequencies) per symbol, namely 2^{SF} chips per symbol. Additionally, the number of bits that can be encoded within a symbol is SF. Thus, a symbol with a total length of 2^{SF} chips, can be cyclically shifted from 1 to 2^{SF} positions. The refer-
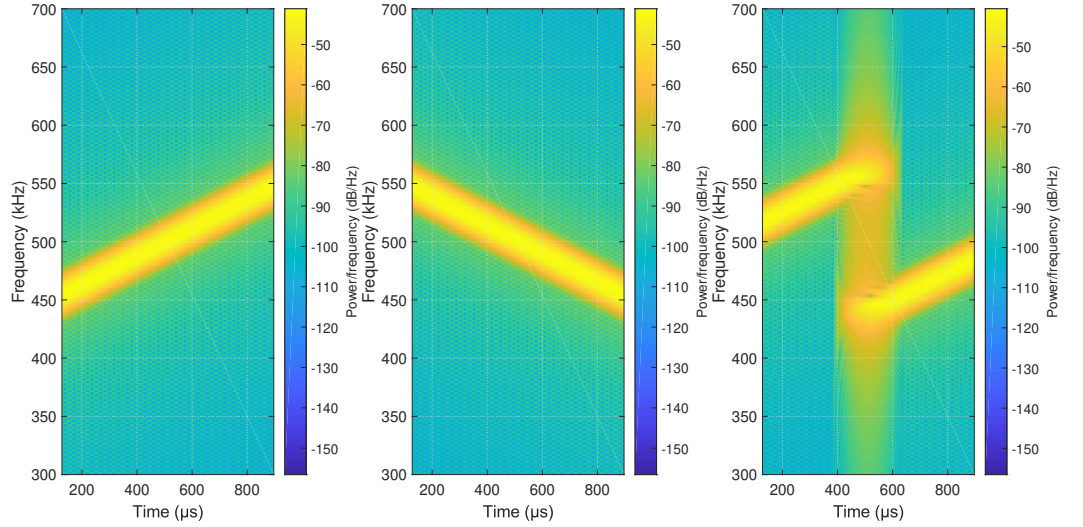
Figure 3.2: Lora frequency modulated carrier wave (CW) signals (chirps) $SF = 7$ and $BW = 125$ kHz. Left: up-chirp, Middle: down-chirp, Right: shifted up-chirp by 64.

ence symbol is given by the unshifted symbol at the beginning of a LoRa packet. The baseband reference symbol is a linear up-chirp/down-chirp that can be represented as a complex waveform described by:

$$s(t) = e^{j\phi(t)}. \tag{3.2}$$

The instantaneous frequency of the signal, $f(t)$ is defined as the phase changing rate given by:

$$f(t) = \frac{1}{2\pi} \frac{d\phi(t)}{dt}. \tag{3.3}$$

In a linear modulated chirp, the frequency varies linearly with time as:

$$f(t) = \frac{BW}{T_s} t \tag{3.4}$$

where T_s is the LoRa symbol period given by:

$$T_s = \frac{2^{SF}}{BW}. \tag{3.5}$$

Taking into account the above three forms and by knowing that the function for the phase is the integral of the frequency, we have:

$$\phi(t) = \phi_0 + 2\pi \int_0^t f(\tau)d\tau = \phi_0 + \pi \frac{BW}{T_s} t^2, \tag{3.6}$$

where ϕ_0 is the initial phase at the time instant $t = 0$. Based on (3.6) a linear modulated up-chirp (Fig. 3.2, left) can be generated by properly varying the phase of a sinusoidal signal instead of directly varying its instantaneous frequency. In order to encode SF bits within an up-chirp as introduced before, LoRa uses cyclic shifts as shown in Fig. 3.2, (right). The reference chirp is divided into 2^{SF} equal frequency steps and the starting frequency will represent the symbol. As is depicted in Fig. 3.2, (right) the symbol 64 is represented by a up-chirp shifted by 64 frequency steps (chips).
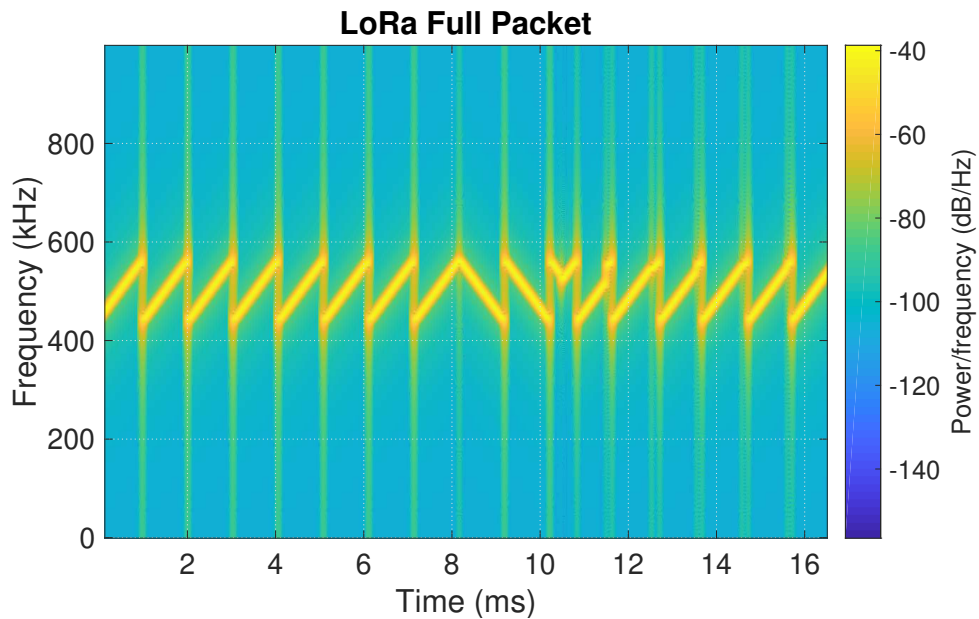
Figure 3.3: Full LoRa packet representation in frequency domain with $SF = 7$ and $BW = 125$ kHz. The packet consists of 8 preamble up-chirp symbols, 2.25 synchronization down-chirps and 6 data symbols.

The first step to demodulating LoRa symbols is to de-chirp the received signal [67]. This is done by channelizing the complex baseband signal to its bandwidth (BW) and then multiplying the result against a locally generated chirp and its complex conjugate (Fig. 3.2, middle). This produces two IQ streams, where the chirped signals are "rotated" within the spectrum to have a chirp rate of 0, meaning

each symbol resides on a unique constant frequency. In the transmitter the result can be defined as:

$$z(t) = s(t)e^{-j(\phi_0 + \pi \frac{BW}{T_s} t^2)},$$ (3.7)

and it is a sequence of discrete samples, $z[k = Ts/m]$, with $k = 1, 2, \ldots, 2^{SF}$ and $m = 2^{SF}, \ldots, 2, 1$. Applying the discrete Fourier transform (DFT) to the sequence $z[k]$ and assuming perfect synchronization, a peak will occur at the bin k that corresponds to the introduced cyclic shift. In order to detect LoRa packets, a specific number of up/down-chirps are added at the beginning of the transmission as a preamble as it is depicted in Fig. 3.3. Two and a quarter additional down-chirps are followed for synchronization purposes and the rest of the packets includes the data section. In Fig. 3.3 the packet consists of 8 preamble up-chirp symbols, 2.25 synchronization down-chirps and 6 data symbols. It is mentioned that in this work only two down-chirps are considered as the synchronization symbols. The aim of the present work is to generate a LoRa packet with an SF of 7 and a BW of 125 kHz, similar to the one represented in Fig. 3.3 with a simple backscatter modulator front-end circuit. The design is targeted to operate at 2.45 GHz and it can operate with any other value of SF or BW.

3.3   IQ Modulator Design

The circuit used to synthesize and backscatter LoRa packets is shown in Fig. 3.4 (a). The circuit was simulated and optimized to operate at 2.45 GHz. It consists of two E-PHEMT RF transistors ATF-54143 [68] from Avago Technologies that can generate a set of impedances by changing their bias, allowing to reflect the incident wave with a pre-defined phase value. Since LoRa uses small bandwidths, the frequency at which the phase is changed (or transistor update) is low. The most important property that the transistors must require is the capability to operate at the backscatter carrier frequency. Due to the low sample rate required, ultra-low power processing units can be attached and operate with the proposed backscatter modulator front-end.

From the previous section, it was shown that any LoRa symbol can be alter-
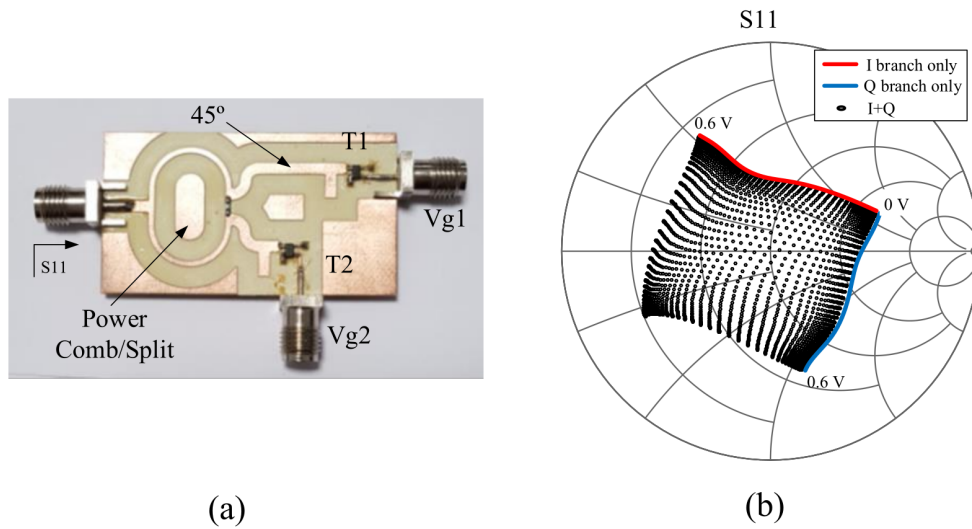
Figure 3.4: IQ impedance modulator front-end. (a) Picture of the prototype. Transistor T_1 and T_2 are controlled by a baseband external source, such as a low power microcontroller. (b) All possible synthesized impedances measured with a grid of 10 mV step, from 0 V to 0.6 V.

natively generated by properly varying the phase of the carrier signal. It is known that phase modulation, in the form of PSK, is an important technique in modern RF systems and phase modulation can be conveniently achieved, in the form of IQ modulation by varying the amplitude of the I and Q signals. Hence, by joining the reflected waves from two independent transistors it is possible to add such modulation to the final reflected wave. Here, the quadrature is achieved by inserting a delay of 45 degrees in one of two branches. In the delayed branch, both the incident and the reflected waves experience a delay of 45 degrees, which produces a reflected signal that is in quadrature (90 degrees) with the signal produced by the other branch. In this work, a conventional Wilkinson power divider is employed to power divide the incident wave as well as to combine the reflected waves produced by both branches. The losses introduced by the power divider (from power split and insertion loss), will undesirably decrease the value of the reflection coefficient. Nevertheless, space power combining techniques may be considered to avoid those losses, at the expense of at least, one additional antenna. It should be noted that, a sweep on the bias voltage of each branch generates a line of impedances in the Smith Chart, which are converted to a blur by joining the I and Q signals in quadrature, as shown in Fig. 3.4 (b). All possible synthesized reflection coefficients measured with a grid of 10 mV step (both I and Q voltages), from 0 V to 0.6 V are depicted in Fig. 3.4
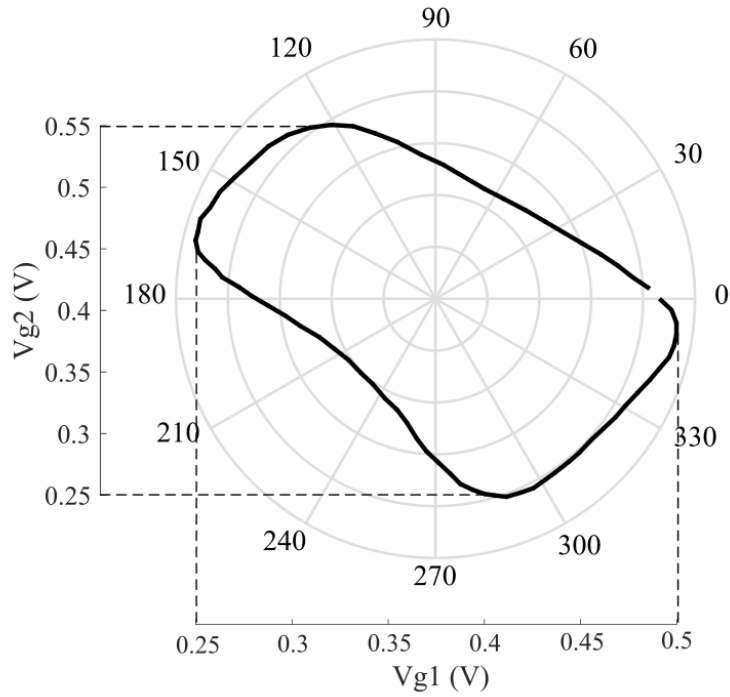
Figure 3.5: Phase of the reflected wave (steps of 5 degrees) and its corresponding IQ voltages. All points will produce a reflected wave with equal amplitude.

(b). In practice, the circuit was characterized with 1 mV step. The 10 mV representation gives a better visualization of the trend. Parallel open stubs were added at the transistors' drains to shift the response to the center of the Smith Chart. By doing so, a new set of impedances can be achieved whose phases vary 360 degrees, within a constant voltage standing wave ratio (VSWR) circle. Thus, it is possible to create LoRa symbols by properly switching between those points/phases with constant VSWR. While the power divider decreases the magnitude of the reflected wave, it affects with the same magnitude value, the whole set of chosen reflections, thus the constant VSWR is still ensured. Also, the circuit was characterized as a whole structure, so the power divider/combiner effects are taken into account.

After the circuit's characterization, the reflection coefficients with phases from 0 to 355 degrees with 5-degree step and a VSWR of 1.9 were identified as well as their respective I (V_{g1}) and Q (V_{g2}) control voltages. The relation between those phases and voltages is depicted in Fig. 3.5 and, therefore, every LoRa symbol can be synthesized by following the represented non-linear transformation.

The circuit was tested with only one branch but, unfortunately, it is not possible to synthesize a set of reflections whose phases vary 360 degrees. Thus, to create such

reflections was founded that by joining two branches in quadrature was the best solution. Additionally, by following this design, it is possible to generate quadrature amplitude modulations, which can make the circuit compatible with several other communication standards [17].

3.4   Coding & Decoding Validation

Based on the relation given in Fig. 3.5 from the previous section, and also based on the required phase progression given by (3.6), a single LoRa symbol was synthesized in order to validate the symbol generation process. For this, a two channel arbitrary waveform generator (AWG) was selected to produce the control voltages required for V_{g1} and V_{g2}. Additionally, a vector signal analyzer (VSA) acquires the backscattered signal and down-converts it to the complex baseband. The sample rate of the generated voltage signals was fixed to 10 MSa/s witch is the maximum upper limit of the AWG. Since the bandwidth of the chirp is BW and thus the frequency is given by phase change, the frequency at which the phase needs to be updated is then given by at least $2BW$. The maximum frequency presented in any gate signal does not exceed BW Hz. LoRa specifies a maximum BW of 500 kHz (we are using 125 kHz), which is a relatively small bandwidth for any conventional RF transistor. The only important property that the transistor must require is the capability to operate at the backscatter carrier frequency.

The captured complex signal is loaded into the MATLAB software and processed. It should be noted that in a real scenario, the arbitrary waveform generator used to validate our proposed design is supposed to be replaced by a small FPGA which is intended to operate at the lowest required sampling rate (ideally $2BW$, which in our example is 250 kHz). For this bit rate the gate voltage will have a maximum update rate of 250 kHz decreasing significantly the power consumption of the overall system. A future challenge is to employ the control circuit of this modulator thus in this work, focus is given to the modulator front-end design and implementation.

Considering symbol index 44 (that is, the result given by (3.6) cyclically shifted by 44), the phase progression required to generate that symbol is depicted in Fig. 3.6, (a). In order to obtain a linear frequency modulated signal, the phase of the signal
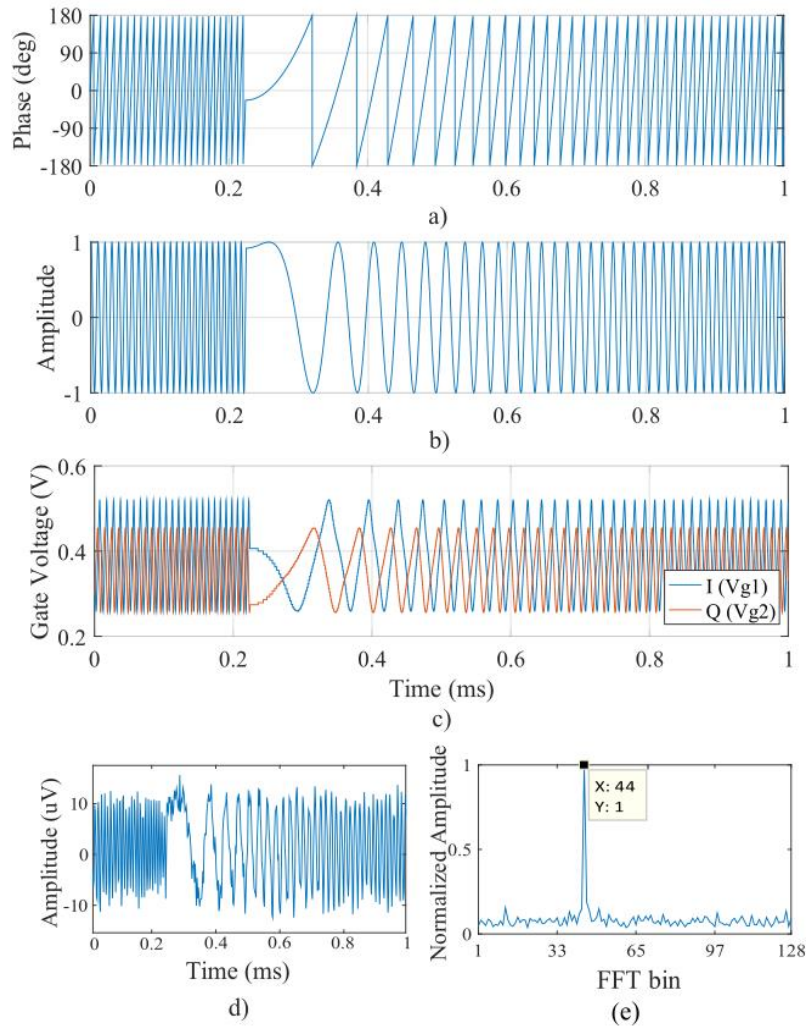
Figure 3.6: Generation of one LoRa symbol. (a) Phase progression required to generate the signal; (b) Real component of the complex baseband waveform; (c) I and Q signals required to produce the phase progression for the desired symbol; (d) Real component of the acquired baseband symbol and (e) DFT result.

must have a quadratic relation as shown. The presented phase progression will generate a complex signal whose real component is depicted in Fig. 3.6, (b) and the required control voltages that must be applied to V_{g1} and V_{g2} to produce the required phase progression are shown in Fig. 3.6, (c). Finally, the real component of the signal acquired and down-converted by the VSA is shown in Fig. 3.6, (d) and the symbol estimation in Fig. 3.6, (e). With a spreading factor of 7, there are 128 possible symbols and LoRa decoding is made in the frequency domain for each symbol period (with an FFT of 128 points). Each FFT will show a single peak at a specific bin, which corresponds to the decoded symbol. In this case, the SNR was

equal to 9.8 dB and was computed by:

$$SNR = 10log_{10}\left(\frac{P_{\text{BW}} - P_{\text{N, BW}}}{P_{\text{N}}}\right), \tag{3.8}$$

where P_{BW} is the total power within the symbol bandwidth (125 kHz), $P_{\text{N, BW}}$ is the noise power within the symbol bandwidth and P_{N} is the total noise power in the sampled bandwidth. It should be noted that the signal may be sampled at exactly BW Hz, allowing to reduce the total noise power level and thus, enhancing the sensitivity.

A CW signal generator was used to generate the backscatter carrier, and the AWG was loaded with the control bias voltage waveforms, V_{g1} and V_{g2}, previously synthesized. A directional coupler was employed to take a fraction of the reflected wave to feed the VSA. Then, the down-converted I/Q signal was loaded into MATLAB, down-sampled to exactly BW Hz and multiplied by the reference down-chirp. Finally, the DFT was applied for symbol decoding.
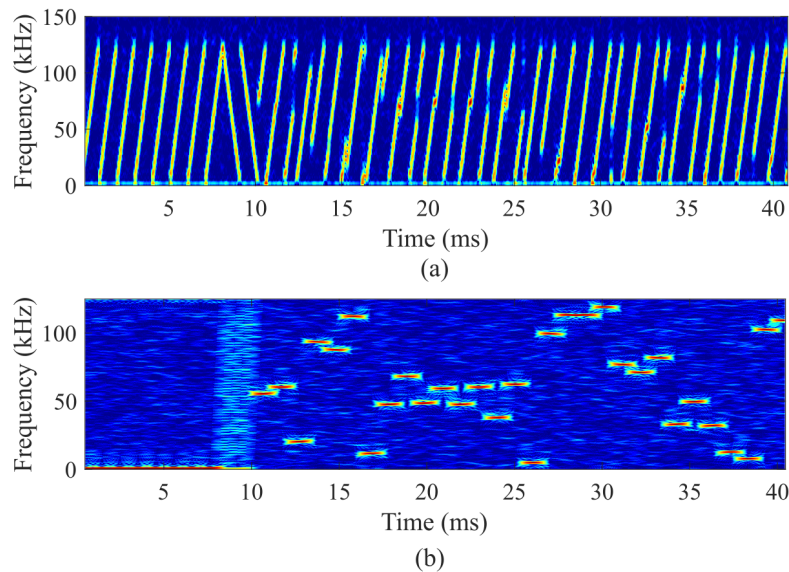
Figure 3.7: (a) Measured received LoRa packet spectrogram and (b) its decoding. Only the first 40 symbols out of 12000 are presented. The packet consists of a preamble of 8 reference symbols, 2 synchronization symbols and 30 data symbols.

After symbol coding and decoding validation, a bit stream consisting of 84000 bits (12.000 symbols) was generated and the respective control voltages, V_{g1} and V_{g2}, were synthesized and loaded to the AWG. A spectrogram of the first 40 symbols received by the VSA are shown in Fig. 3.7, (a). The represented signal consists of a preamble

with 8 reference symbols, 2 synchronization symbols and 30 data symbols. Fig. 3.7, (b) illustrates the spectrogram from the decoded symbols. After multiplying each symbol with the conjugate of the reference symbol, the preamble, synchronization and transmitted data symbols can be clearly seen. The data symbols are represented by constant frequencies that result from such multiplication. The frequency represents the symbol and the length of the data symbol represents the time that it took to be fully transmitted. The synchronization was performed by delaying the received packet until a maximum occurs at the first DFT bin, for the first 8 preamble symbols.

3.5   Performance Evaluation

For receiver sensitivity calculations, we require the minimum SNR value so that the information can be decoded without a significant amount of errors, before applying error correction algorithms [69]. LoRa modulation combines forward error correction (FEC) techniques and spread spectrum processing gain to allow high sensitivities. This SNR value depends upon the spreading factor. Lower spreading factor values allow to increase the data rate but will reduce the distance at which the signal can be successfully decoded. On the other hand, higher spreading factor values will increase the OTA time and will in turn, reduce the allowable data rates. Nevertheless, in these situations higher communication distances can be achieved. In order to evaluate the performance of the proposed LoRa backscatter modulator front-end, cabled as well as OTA tests were conducted as follows.

3.5.1   Cabled Measurements

The first experiment was dedicated to evaluate the BER vs SNR. For this, the 12000 symbols generated before were transmitted several times for each SNR value, sampled by the VSA and processed with MATLAB. The achieved BER was computed by taking the average value of all those measurements and it is plotted in Fig. 3.8. The achieved results are in accordance with other related work within the literature, with the same spreading factor value [70–72]. It must be noted that the received signal power level is controlled by setting the appropriate input power level
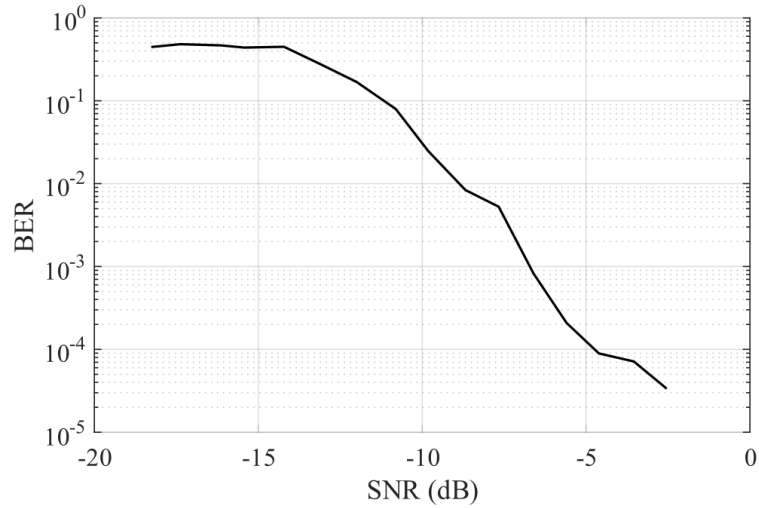
Figure 3.8: Measured bit error rate (BER) versus received Signal-to-noise-ratio (SNR).

of the backscatter carrier that is fed to the circuit.
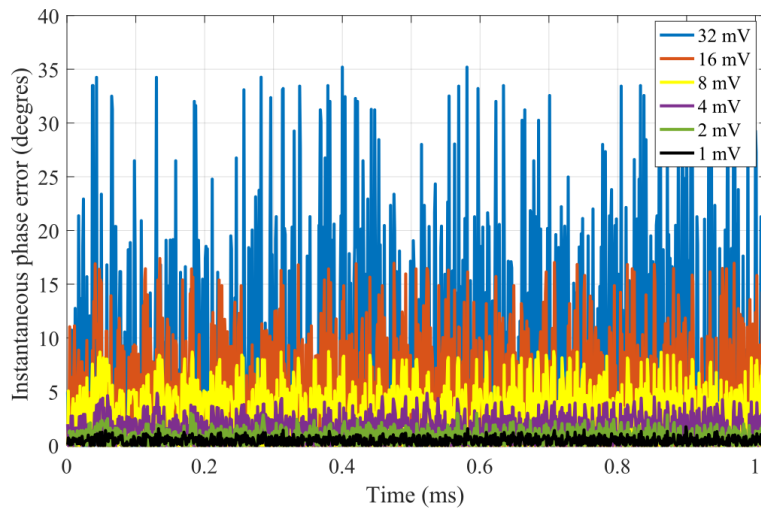
Figure 3.9: Instantaneous phase error of one preamble symbol when each sample of the control voltages V_{g1} and V_{g2} are corrupted with $\pm 1, 2, 4, 8, 16$ and 32 mV.

Additionally, with the same cabled configuration, intentional noise was added to the control voltages that are required to generate a preamble symbol. The aim is to evaluate the required processing unit precision and its robustness against external interferences. Both control voltages were corrupted by random perturbations around the nominal value. Perturbations of ± 1 mV up to ± 32 mV of the nominal value were tested, measured and the instantaneous error between those measurements and the nominal scenario are represented in Fig. 3.9. The instantaneous phase error is
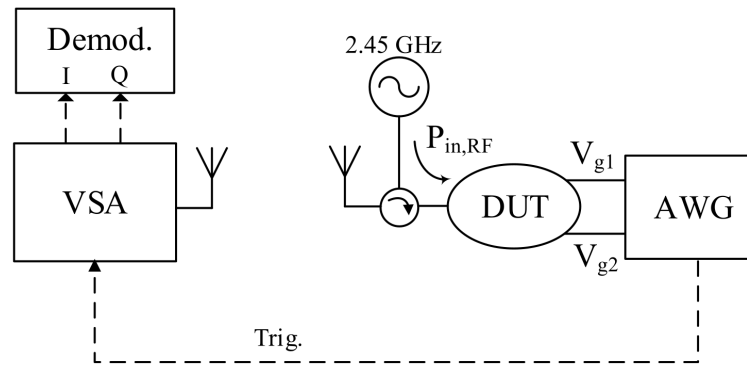
Figure 3.10: Block diagram representation of the laboratory setup used for over-the-air measurements.

shown to be less than 2 degrees for perturbations of ± 1 mV, less than 10 degrees for ± 8 mV, and for ± 32 mV it can get as high as 35 degrees. It was seen that the BER vs SNR curve, under control bias noise, is exactly the same. However, the backscatter input power must be increased to achieve the same SNR. In the following, it will be shown that the impact of a ± 8 mV perturbation is almost unnoticeable while ± 32 mV starts to produce undesired results.

3.5.2 Over-the-Air Measurements

With the laboratory setup illustrated in Fig. 3.10, several OTA tests were performed. A 2.45 GHz power source that generates the backscatter carrier is collocated with the proposed device. A circulator redirects the reflected wave to the antenna as shown. The receiver consists of a VSA that down-converts the signal to the complex baseband. Then, the acquired signal is loaded into MATLAB software and processed to obtain an estimation of the transmitted information. Two similar single element patch antennas were designed to operate at 2.45 GHz, with an estimated gain of 6 dBi.

Three different indoor scenarios within a laboratory environment were targeted for evaluation and shown in Fig. 3.11. The aim is to provide information about how much power the device requires from the backscatter carrier to produce a successful transmission. The first, Fig. 3.11 (a), is a typical indoor scenario with Line-of-sight (LoS) conditions. An estimation of the distance between the receiver (VSA) and the device is 10 meters. In this particular scenario, intentional perturbations were also

added to the control voltages, namely, ± 8 mV and ± 32 mV. In the second scenario, Fig. 3.11 (b), the device is positioned close to the floor at roughly 7.5 meters from the receiver. In this situation, there are desks with laboratorial instruments and other common laboratory hardware in-between the device and the receiver antenna. In the third scenario, Fig. 3.11 (c), the setup is re-positioned in order to account the effects produced by a wall on the signal's path, with the receiver located 10 meters away from the device.

In all these indoor experiments, 12000 symbols were transmitted several times for each backscatter carrier input power level (steps of 1 dB) and the percentage of the overall symbol error was computed and shown in Fig. 3.12. It is shown that in the first scenario, -40 dBm of backscatter carrier input power is required to produce error-free transmissions. Additionally, it is shown that a random perturbation of ± 8 mV on the control voltages does not produce noticeable effects, while ± 32 mV produces a sensitivity decrease of 2.2 dB. Higher perturbation values require higher backscatter carrier input power to keep the same received SNR. In the second scenario, the non-LoS conditions imposed by the desks determine that the required backscatter carrier input power for error-free transmission is -25 dBm. Finally, due to the wall attenuation, the input power required for error-free transmissions is -26 dBm. It should be noted that the measurements were taken during normal operation of the laboratory and under possible heavy 2.45 GHz Wi-Fi network interference.

Backscatter communications are generally associated with wireless power transfer (WPT) systems. Thus, with the presented approach, it is possible to build a full passive wirelessly powered LoRa backscatter communication device that may operate over larger distances when compared with the conventional SNR needed for ASK, FSK or PSK backscatter modulation systems. Moreover, it is shown that the proposed device has the prominent versatility to backscatter signals compatible with many other standards, thanks to the IQ impedance modulation.

The proposed backscatter approach power consumption is negligible when compared with the control circuit consumption that will be attached to it. It should be noted that every LoRa end-device requires some kind of processor which is used to process data as well as to control its RF front-end. With our design we only

require the baseband signals and 2 RF transistors. For example, the RN2483 Microchip LoRa transceiver idle state current consumption, for a 3.3 V operation, is 2.8 mA, while in transmit mode the current consumption is 38.9 mA (1.6 uA for the sleep state). These values clearly show the impact of a LoRa end-device RF front-end power consumptions. The drawback of employing backscatter techniques is the communication range. Nevertheless, by using them, ultra-low power end-devices can be explored.

3.6 Conclusion

In this chapter, an novel IQ impedance modulator for LoRa backscatter was presented. The poof-of-concept modulator combines LoRa standards with backscatter communication and generates chirp symbols by reflecting an incident unmodulated carrier. Moreover, the design was validated by generating several LoRa symbols with successful transmissions. Measurements of the un-coded BER vs SNR were conducted. By considering an un-coded BER of 10^{-3}, which can be considered as a reference value, our design requires an SNR of -6.8 dB. One of the main advantages compared to other related circuits is that it is based on a very simple circuit, it employs only two transistors and a power divider. Since LoRa uses small bandwidths, the frequency of the phase change (or transistor update) is low. Due to the low sample rate required, ultra-low power processing units can be attached and operate with this device. By developing the system for 2.45 GHz, it is possible to use the Wi-Fi or 802.15.4 devices (from the Wi-Fi routers and ZigBee hubs) to generate the required RF carriers, since most of those radio transceivers provide access to a special test mode that produces an un-modulated carrier signal.

Figure 3.11: Scenarios targeted for evaluation. (a) Typical indoor scenario with LoS conditions. The distance between the receiver (VSA) and the device is 10 meters. (b) Desks with laboratorial instruments and other common laboratory hardware in-between the device and the receiver antennas, 7.5 meters. (c) A wall in-between device and receiver, 10 meters.
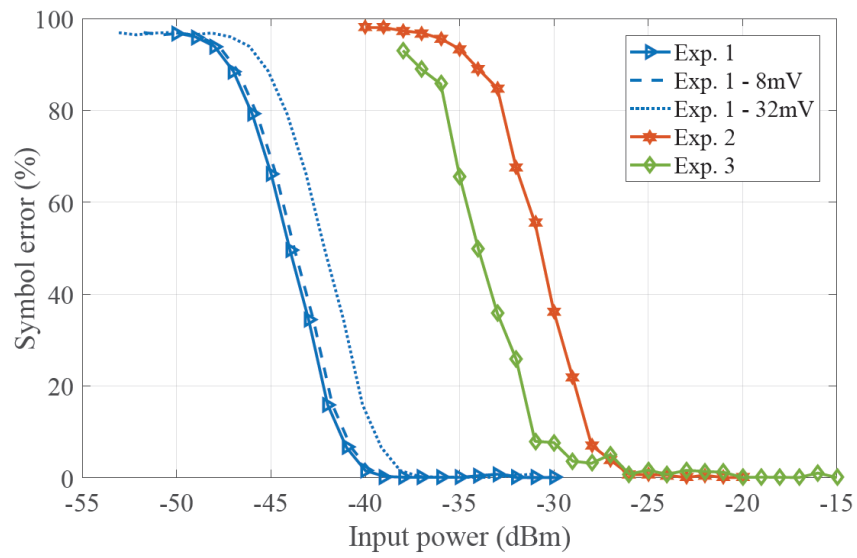
Figure 3.12: Symbol error percentage versus backscatter carrier input power level measured for all scenarios. Results for perturbations of ± 8 mV and ± 32 mV are provided for the first experimental scenario.

Chapter 4

Binary Ambient Backscatter

4.1 Introduction

Utilizing ambient signals for backscattering, the communication scheme is simplified since it requires only a receiver eliminating the need for a CW emitter. For example, ambient backscattering devices, such as RFID tags, can communicate with a reader by backscattering ambient RF signals that are available from multiple sources, such as mobile communications, television [20], frequency modulated (FM) radio [73] and Wi-Fi [74] that are typically widely available in urban areas indoors and outdoors during day and night. In [20] two battery-free tags communicate via ambient backscatter TV signals. In [74], a Wi-Fi backscatter deployment was designed to connect battery-free devices with off-the-shelf Wi-Fi devices. Also a full-duplex ambient communication system was introduced in [75], where a Wi-Fi access point (AP) can cooperate with backscatter IoT sensors with high data throughput. The use of ambient RF signals as the only source of both the CW carrier and the tag power is an extremely energy-efficient communication technique compared to the general backscattering technique. In ambient backscatter communication there are issues with the signal detection that adopts the differential encoding (FM0, Manchester, and Miller encoding) to eliminate the necessity of channel estimation. In [76–78] is presented a fully developed theory on signal processing and performance analysis for ambient backscatter communication systems. A practical transmission model for an ambient backscatter system is presented in [78]. They assume that the tag sends some low-rate messages to a reader with the help of an ambient RF signal source.
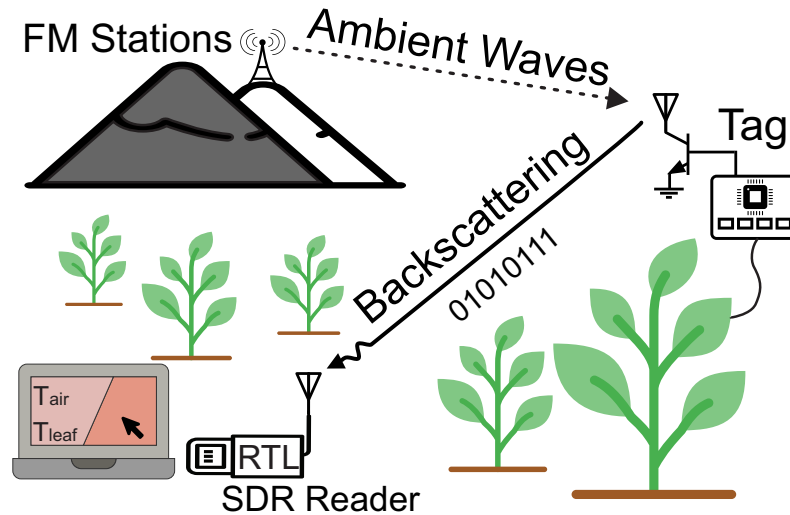
Figure 4.1: Deployment of ambient backscattering in smart agriculture applications. Backscatter communication is achieved using ambient frequency modulated (FM) signals. The differential temperature (T_{leaf}-T_{air}) is measured by the tag-sensor and is transmitted back to a SDR receiver.

It provides fundamental studies of noncoherent symbol detection when all channel state information of the system is unknown.

In [79] preliminary results for a wireless sensor node prototype for agricultural monitoring were presented. The sensor node measures the temperature difference between the leaf and the atmosphere in order to estimate the water stress of a plant [26]. The tag modulates and reflects a fraction of the ambient FM station signals back to the reader as it is shown in Fig. 4.1.

This chapter is an extensive presentation of an novel ambient FM backscatter monitoring system [79] with low complexity and low power. We propose an improved version of this system for generic environmental monitoring applications by designing an improved receiver algorithm. In addition to the receiver implementation, we provide additional details about the tag circuitry, a theoretical tag-receiver framework for the operation of the ambient backscatter system and a series of PER and BER measurements in a proof-of-concept indoor environment. The tag consists of a MCU and an RF communication front-end. The tag reads the information from the sensors and generates pulses that control an RF switch. The binary OOK with FM0 encoding [80] was selected for backscatter modulation, similarly to conventional passive RFID tags. Furthermore, a real-time receiver was implemented using an ultra low cost SDR. The operation of the system prototype was demonstrated

in the lab using an existing FM transmitter broadcasting 34 km away from the tag. Operation over a 5 m tag-to-reader distance was achieved by backscattering sensor data at 0.5, 1 and 2.5 Kbps bit rates.

The work is different from [20], which first proposed ambient backscattering, in that it used ambient digitally modulated television signals (DTV) whereas the system proposed in this paper uses analog FM signals. Also, a moderately expensive software defined USRP-N210 radio ($\sim 1 - 5K$ USD) used in [20] to receive and decode the signals whereas in our work a low cost Realtek (RTL) SDR (22 USD) was used. Recently, [73] also proposed ambient backscattering using FM signals but only for 2-FSK modulated signals. In our work we used OOK modulation with FM0 encoding. In addition, an arbitrary waveform generator was used in [73] to generate the ambient FM signals contrary to signals from existing broadcast FM stations in this paper. Therefore, this work takes into account all the signal characteristics of an FM radio broadcasting and serves as the proof-of-concept for practical ambient backscatter deployments. The findings reported are equally useful for indoors and outdoors, where FM broadcasting signals are pervasive.

The structure of the chapter is as follows: Section 4.2 provides the principles of binary FM ambient backscatter communication. Section 4.3 describes the design and implementation of the sensor node-tag parts. Section 4.4 provides the theory and performance analysis of the proposed system. Section 4.5 discusses the hardware and software part of the low cost receiver. Section 4.6 presents proof-of-concept experimental results, including an indoor demonstration and range measurements. Results showing the correlation of PER and BER versus tags-to-reader distance are also provided. Finally, section 4.7 includes concluding remarks.

4.2   FM Ambient backscattering

4.2.1   FM Broadcasting Operation

The FM broadcasting technology was first utilized in 1940 radio-audio transmissions and nowadays FM radio broadcasts take place between radio frequencies of 88 MHz to 108 MHz with a channel bandwidth of 200 KHz. Each FM station uses frequency modulation in order to transmit the audio signals and the information signals varying
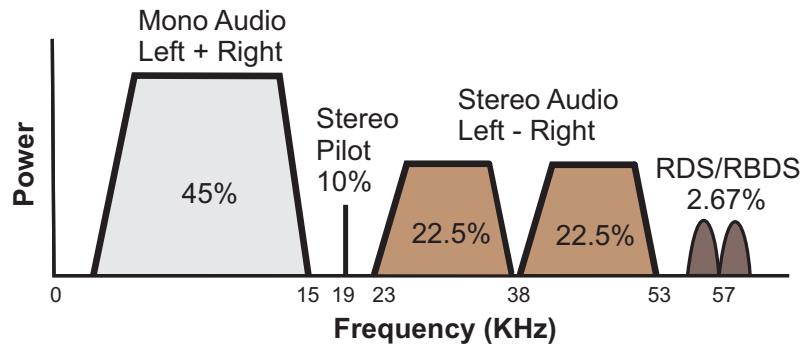
Figure 4.2: Baseband Spectrum of a generic modern-day FM audio station. The signal contains left (L) and right (R) channel information (L+R) for monophonic and stereo reception.

the frequency of a carrier wave accordingly. A typical FM output signal is given by the following equation [81]:

$$x_{\mathrm{FM}}(t) = A_{\mathrm{c}} \cos\left[2\pi f_{\mathrm{c}}t + 2\pi K_{\mathrm{VCO}}\Delta f \int_0^t m(x)\mathrm{d}x\right] \tag{4.1}$$

where $m(x)$ is the baseband message signal, and Δf is the frequency deviation which is equal to the maximum frequency shift from f_{c} while K_{VCO} is the gain of the transmitter's VCO. Generally, it is not straightforward to analyze the properties of $x_{\mathrm{FM}}(t)$ due to its non-linear dependence to the $m(x)$. The baseband message signal of a typical FM station as shown in Fig. 4.2 can be expressed as:

$$m(t) = A_0\big[S_{\mathrm{L}}(t) + S_{\mathrm{R}}(t)\big] + A_1 \cos(2\pi f_1 t) +$$

$$\tag{4.2}$$

$$A_0\big[S_{\mathrm{L}}(t) - S_{\mathrm{R}}(t)\big]\cos(2\pi f_2 t) + A_2\mathtt{RDS}(t)\cos(2\pi f_3 t)$$

with $f_1 = 19$ KHz, $f_2 = 38$ KHz, $f_3 = 57$ KHz. The S_{L} and S_{R} define the time domain signals from the "stereo left" and "stereo right" channels, respectively, while $\mathtt{RDS}(t)$ is the time domain signal of the Radio Data System (RDS) and Radio Broadcast Data System (RBDS). The gain factors A_0, A_1, and A_2 are used to appropriately scale the amplitude of S_{L} and S_{R} waveforms. As it can be easily observed in Fig. 4.2, the $0 - 15$ KHz part of the message signal consists of the left and right channel information [(Left)+(Right)] for monophonic sound. Stereophonic sound is the result of the amplitude modulation of the [(Left)-(Right)] message onto a suppressed 38 KHz subcarrier in the $23 - 53$ KHz region of spectrum. Furthermore, there is a 19 KHz

pilot tone to enable receivers to recognize and decode the two stereo channels. Modern FM radio signals also include a 57 KHz subcarrier that carries RDS and RBDS data.

4.2.2 Ambient FM backscatter

In the case of typical ambient FM backscatter systems, incident "CW carrier" to the tag antenna is the signal in (4.1). The SDR receiver receives the superposition of this signal and the backscattered tag signal. Following the same procedure described in [8] and equation (2.2), but using a FM modulated carrier instead of a CW signal one may obtain the following complex baseband signal at the receiver:

$$y_{\mathrm{amb}}(t) = n(t) + \frac{A_c}{2} e^{-j2\pi\Delta Ft} \big[\alpha_{\mathrm{CR}} e^{-j\phi_{\mathrm{CR}}} e^{-jM(t-\tau_{\mathrm{CR}})}$$

$$+ s\alpha_{\mathrm{CT}}\alpha_{\mathrm{TR}} e^{-j\phi_{\mathrm{CTR}}} e^{-jM(t-\tau_{\mathrm{TR}})}\Gamma(t - \tau_{\mathrm{TR}})\big] \tag{4.3}$$

and

$$M(t) = 2\pi K_{\mathrm{VCO}}\Delta f \int_0^t m(x)\mathrm{d}x. \tag{4.4}$$

The received signal y_{amb} contains the desired information Γ but also the carrier, FM modulation and frequency offset. The magnitude square of the received complex waveform will be formulated below in order to eliminate the frequency offset. If the desired magnitude square is formed, a component proportional to the desired information will be generated along with direct current (DC) and other interference terms. We show theoretically and experimentally in section 4.6 that it is possible to successfully decode the signal provided there is a sufficiently high SNR.

4.3 Tag Design

4.3.1 Tag

The main DIGITAL part of proposed tag is based on a 16-bit MCU development board MSP-EXP430FR5969 [82] (Fig. 4.3). The development board is powered from a 0.1 F supercapacitor. The tag also includes a real-time clock (RTC) to wake up the MCU from the "sleep" operation mode, where the current consumption of the board
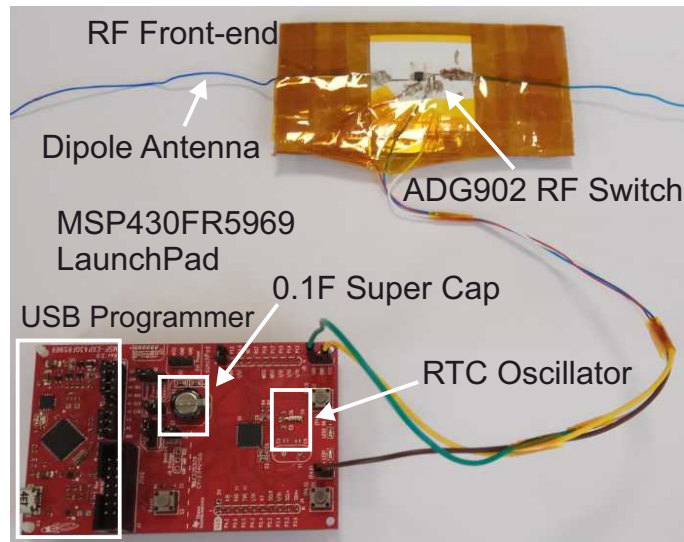
Figure 4.3: The proposed tag prototype consists of a MSP430 development board connected with an RF front-end board. The RF front-end was fabricated using inkjet printing technology on a paper substrate. A MCU digital output pin was connected with the control signal of the RF switch. The operation power of RF front-end was supplied by the MCU development board and the whole system was supplied by an embedded super capacitor for duty cycle operation.

is 0.02 μA. The MCU generates 50% duty cycle pulses that control the RF switch, thus generating an OOK modulated backscattered signal. The OOK modulation is described in more detail in the subsection 4.3.2. The MCU was programmed at 1 MHz clock speed using the internal local oscillator. The current consumption at 1 MHz was 126 μA at 2.3 V (290 μW).
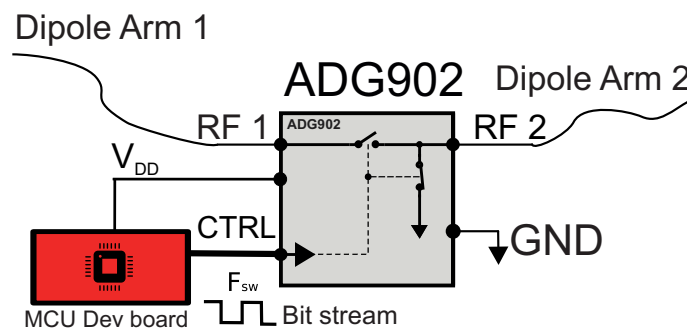
Figure 4.4: Schematic of the RF switch utilized for the load modulation and of the dipole antenna arms.

The MCU has a 16 channel, 12 bit ADC which was used to read analog output signals from sensors. In this work the tag is programmed to read four analog inputs and the voltage level of the super capacitor. These analog inputs can be used to provide information from out to four sensors. This part of work focuses on the

telecommunication aspect of the system and when a tag wants to communicate with the reader, it sends a packet that contains the information of only one sensor each time. In [79] only two ADC inputs for two high precision, analog temperature sensors were used.

The backscatter communication of the tag is achieved with a separate RF front-end board. It consists of a 1.5 m wire dipole antenna in order to resonate within the FM band (95 MHz) and a SPST RF switch ADG902 by Analog Devices. The fabricated prototype is shown in Fig. 4.3, while the circuit schematic of the front-end is provided in Fig. 4.4.

The switch element varies the antenna load between two impedance values and is selected due to its low insertion loss ($\sim$ 0.5 dB @ 100 MHz) and high off isolation ($\sim$ 57.5 dB @ 100 MHz). The RF switch is a complementary CMOS reflect-mode (i.e. not terminated) switch with high off-port voltage standing wave ratio (VSWR) and consumes less than 1 μA at 2.75 V [83]. It is driven by a digital output of the MCU as shown in Fig. 4.4. The power consumption of the RF switch follows the equation $\frac{1}{2}C_{RF}V_{DD}^2 F_{\text{sw}}$ which is the CMOS dynamic consumption [16]. The F_{sw} is the control switching frequency and C_{RF} the dynamic power dissipation capacitance at RF path when it is ON. For $F_{\text{sw}} = 2.5$ KHz, which equals to our maximum bit rate 2.5 Kbps, $V_{DD} = 3.3$ V, and $C_{RF} = 1.2$ pF (@ 1 MHz) the power consumption is estimated at 16.3 nA. As the data rate increases (switching speed) the DC power consumption increases. The front-end PCB was fabricated using inkjet printing technology on a paper substrate. The characteristics of the the substrate was: $\varepsilon_{\text{r}} = 2.9$, $\tan \delta = 0.045$ and substrate height 210 μm. The traces were printed with conductive silver nanoparticle (SNP) ink and conductive epoxy deposition was used in order to attach the switch to the substrate.

In order to minimize the average power consumption, a duty cycle operation was programmed where the tag was active only for a desired minimum period of time. The duty cycle operation was set using the RTC and the sleep mode of the MCU. An RF harvester and solar cell could be utilized for powering as it is shown for example in [53, 84].

Figure 4.5: Left: In FM0 encoding, the boundaries of the bits must always be different. Two sequential "on" or "off" correspond to the bit "1". Right: FM0 decoding technique, after shifting by T_{symbol}, receiver has to detect only two possible pulse shapes (line square or dash line square).

4.3.2   Telecommunication Protocol

The tag uses ASK modulation to transmit its data via backscattering. More specifically, by changing the RF switch states between "on" and "off" and backscattering the ambient FM broadband signals, a binary ASK modulated signal of OOK type can be created described by (4.3). Using OOK modulation, the information-containing received tag signal of (4.3) can be expressed as [8]:

$$\Gamma(t - \tau_{\text{TR}}) = \sum_{n=0}^{N-1} x_n \Pi[t - nT_{\text{symbol}} - \tau_{\text{TR}}], \tag{4.5}$$

where $x_n \in \{-1, 1\}$ are the N transmitted symbols and $\Pi(t)$ is the pulse (symbol) with duration T_{symbol}. In addition to the OOK modulation, the low-power consuming FM0 technique is utilized to encode the sensor data. For binary OOK, x_n would be the bits and for FM0-coded OOK, x_n are the binary symbols. In FM0 encoding there is an inversion of the phase at every bit boundary (at the beginning and at the end of every bit), and additionally bit "0" has an additional phase inversion in the middle (Fig. 4.5, left). Each bit includes two symbols, as shown in Fig. 4.5. The duration of a bit and of a symbol are denoted as T_{bit} and T_{symbol} respectively. The data bit rate is $1/T_{\text{bit}}$ bits per second (bps). The FM0 encoding always ends with a dummy "1" bit in order to detect easily the end of the bitstream. In the case that the received backscatter waveform finishes with a "LOW", it would be indistinguishable from receiving the reader's CW only (i.e. no packet transmission).

Figure 4.6: Example of the oscilloscope-measured transmitted rectangular pulses (MCU output). The packet ("bit stream") consists of the Preamble, Tag ID, Sensor ID and Sensor Data bits and an extra dummy bit "1" at the end.

The tag is programmed to send the data in packets to the reader and the reader tries to receive and decode them. The length of each packet is fixed. Fig. 4.6 shows a typical packet format. The packet has the length of 26 bits and begins with the preamble bits. After that follow the "Tag ID" bits, the "Sensor ID" bits and finally the "Sensor Data" bits. The preamble is useful for bit-level synchronization at the receiver and was fixed to be `1010101111` (10 bits) in our proof-of-concept tests. The "Tag ID" (2 bits) is utilized in the case of simultaneous multiple tag utilization. As mentioned before, the tag can support up to four sensors, and therefore the "Sensor ID" (2 bits) is used to identify the sensor the data is coming from.

4.4 Receiver Theory

In this work, ambient backscatter modulation based on OOK modulation with FM0 encoding is used, as in conventional passive RFID tags [80]. It is also known as biphase-space modulation [85]. In FM0, a symbol "1" is represented by a rectangular pulse while a "0" is represented by a positive half-symbol wide rectangular pulse followed by a negative half symbol pulse. In addition, a polarity change is implemented in the beginning of every symbol. An example of FM0 encoding is shown in Fig. 4.5, left. As a result, four possible waveforms are transmitted corresponding to a two-dimensional bi-orthogonal constellation. However, if one observes the FM0 signal shifted by one symbol, only two possible waveforms exist, which are the ones of bit "0". These two waveforms correspond to a one-dimensional antipodal constel-

lation which is easier to study and decode [85]. The detected bits from the half-bit time shifted signal correspond to the originally transmitted bits after differential encoding. Therefore, one can proceed to decode the FM0 signal in two steps, first detecting the time-shifted bits and then using a differential decoder to recover the originally transmitted bits. In this section, we first derive the error probability P_s of the time shifted signal. Once P_s is obtained, the error probability of the originally transmitted bit stream P_e is given by [85, 86]:

$$P_e = 2P_s(1 - P_s). \tag{4.6}$$

As it is shown in [85], in addition to the simplification of the detection process, the fact that an antipodal constellation is used leads to a SNR improvement of approximately 3 dB in comparison to the standard detection method based on the bi-orthogonal constellation.

In order to derive P_s, one may proceed following references [8] and [78]. In [8] a thorough analysis of traditional backscattering in a bi-static configuration is presented using a CW carrier signal. OOK modulation was assumed but without considering FM0 encoding. In [78], the analysis of the error probability of ambient backscatter systems was presented considering randomly modulated signals. In addition the special case of PSK modulation is treated in Appendix B, which is similar in analysis to FM signals used in this work, in that the carrier amplitude is constant. However, [78] also does not use FM0 encoding. In this work, we proceed by following the formulation of [78] but treat the case of FM0 encoding taking into account [85] as described in the previous paragraph. The received signal complex envelope was given in (4.3) and repeated here for convenience in a more compact form:

$$y(t) = Ae^{-jD}\left(\alpha_1(t)e^{-jK_1} + \alpha_2(t)b(t)e^{-jK_2}\right) + n(t). \tag{4.7}$$

The term D includes the frequency and phase offset, K_1 is the delayed modulation signal arriving directly from transmitter to the receiver and K_2 delayed modulation signal arriving through the tag. $b(t)$ is the information signal and $n(t)$ is additive zero mean complex white Gaussian noise added at the receiver $n(t) \sim \mathcal{N}(0, N_w)$. Following [78] we assume that $K_1 = K_2$ due to the fact that the two paths are

approximately equal. In addition, any thermal noise generated in the tag is ignored as very low [78] value. The obtained equation is:

$$y(t) \approx Ae^{-jD}e^{jK}h(t) + n(t). \tag{4.8}$$

Where $h(t) = a_1(t) + a_2(t)b(t)$ is the complex valued signal containing the information from the tag and the channel effects. In order to eliminate the frequency and phase offset in the receiver we form the magnitude square of the envelope:

$$Z(t) = A^2|h(t)|^2 + |n(t)|^2 + 2\Re\{Ae^{-jD}e^{jK}h(t)n^*(t)\}$$

$$= A^2|h(t)|^2 + w(t). \tag{4.9}$$

Following the Appendix B of [78], and invoking the Central Limit Theorem (CLT), $w(t)$ is a real Gaussian process with mean and variance given by:

$$w(t) \sim \mathcal{N}\left(N_{\mathrm{w}}, N_{\mathrm{w}}^2 + 2A^2N_{\mathrm{w}}|h(t)|^2\right). \tag{4.10}$$

The N_{w} is the noise power at the receiver. One should note that before the decoding process the receiver applies a low pass filter consisting of an averaging operation of approximately 1000 samples, which further supports the reasoning of invoking the CLT. The receiver applies a synchronization algorithm to derive the beginning of the information signal which is described in more detail in section 4.5. In order to facilitate the synchronization process a DC offset removal was applied to $Z(t)$. Due to the fact that the DC offset removal does not affect the detection process it will not be considered in this section. Once synchronization is achieved a time shifted version of the received bits $Z(t)$ is considered and detection based on an antipodal constellation is applied. Specifically, the received signal $Z(t)$ is correlated with pulse:

$$q(t) = \begin{cases} +1, & \text{if } 0 < t \leq \frac{T_{\mathrm{bit}}}{2} \\ -1, & \text{if } \frac{T_{\mathrm{bit}}}{2} < t \leq T_{\mathrm{bit}} \end{cases} \tag{4.11}$$

giving:

$$U(t) = X + V$$

$$= \int_0^{T_{\text{bit}}} A^2 |h(t)|^2 q(t) \mathrm{d}t + \int_0^{T_{\text{bit}}} w(t) q(t) \mathrm{d}t.$$

(4.12)

Due to binary modulation $|h(t)|^2$ takes one of two values $|h_{\text{H}}|^2$ or $|h_{\text{L}}|^2$. It is straight-forward to show that V is a real Gaussian process with mean and variance given by

$$V \sim \mathcal{N}\left(0, 2T_{\text{bit}} N_{\text{w}}^2 + T_{\text{bit}} A^2 N_{\text{w}} \left(|h_{\text{H}}|^2 + |h_{\text{L}}|^2\right)\right).$$

(4.13)

Similarly:

$$X_{\pm} = \pm \frac{T_{\text{bit}}}{2} A^2 \left(|h_{\text{H}}|^2 - |h_{\text{L}}|^2\right),$$

(4.14)

with the sign depending on whether $q(t)$ or $-q(t)$ was transmitted. Assuming equal probability of transmission of the two possible symbols, one derives:

$$P_{\text{s}} = P\{U < 0|+\} = Q\left(\frac{X_+}{\sigma_{\text{V}}}\right),$$

(4.15)

where $Q(x)$ is the tail probability of the normal distribution function [85, 86]. $P(U < 0|+)$ denotes the probability that $U < 0$ when $q(t)$ was transmitted. Therefore, the originally transmitted bit error probability is:

$$P_{\text{e}} = 2Q\left(\frac{X_+}{\sigma_{\text{V}}}\right)\left(1 - Q\left(\frac{X_+}{\sigma_{\text{V}}}\right)\right).$$

(4.16)

It should be noted that in order to compute P_{e} one needs information of the signal at the two different states $|h_{\text{H}}|^2$ and $|h_{\text{L}}|^2$ but also of the noise power N_{w}, something which was also highlighted in [78], Appendix B.

A method to compute P_{e} is outlined in order to compare the theoretical analysis with bit-error rate measurements. Consider a given setup of transmitter, tag and receiver, and perform the following three power measurements, i.e. on signal $Z(t)$. While transmitting a modulated signal, set the tag to a fixed state and measure the received power, to obtain:

$$P_{\text{yH}} = A^2 |h_{\text{H}}|^2 + N_{\text{w}}$$

(4.17)
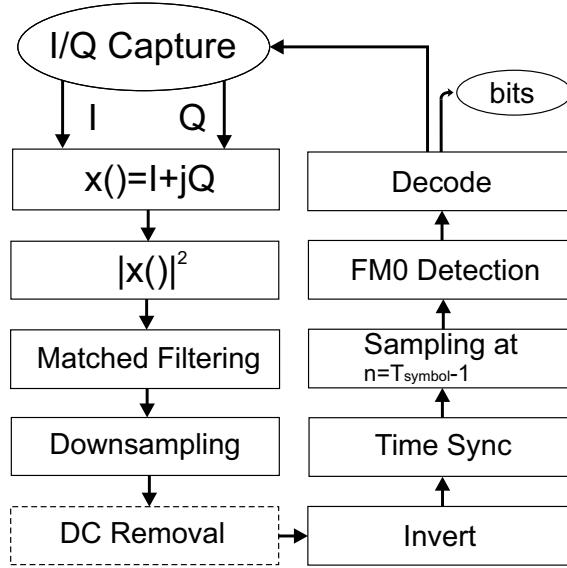
Figure 4.7: Flow chart of the real-time receiver algorithm.

and

$$P_{\text{yL}} = A^2 |h_{\text{L}}|^2 + N_{\text{w}}. \tag{4.18}$$

Then turn the transmitter off and measure the noise power N_{w}. The most significant noise contribution is due to the receiver electronics and thus the state of the tag during the noise measurement is not important. Using the three measurements one has

$$X_{\pm} = \pm \frac{LT_{\text{s}}}{2} \left(P_{\text{yH}} - P_{\text{yL}} \right) \tag{4.19}$$

and

$$\sigma_V^2 = LT_{\text{s}} N_{\text{w}} \left(P_{\text{yH}} + P_{\text{yL}} \right). \tag{4.20}$$

where T_s is the sampling period. In our implementation $L = 10$ samples per bit were used. Using the P_{yH}, P_{yL} and N_{w} measurements, one can apply (4.19) and (4.20) in (4.16) to compute the theoretical BER for a given transmitter power level.

4.5   Receiver Implementation

In this work, the low cost RTL SDR was used as receiver same as subsection 2.6.1. Using the sampling rate of 1 MSps, it was connected to an improved telescopic monopole antenna in order to receive the FM signals. The received signal of Eq. 4.3 contains the useful bits in FM0 encoding (rectangular pulses in Eq. 4.5). A real-
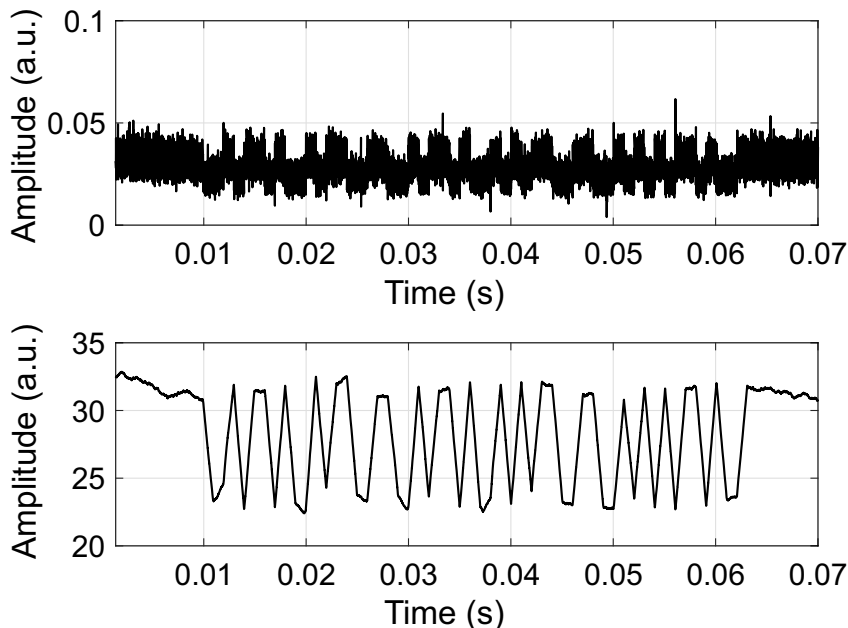
Figure 4.8: Received signal including a data packet. Top: Squared absolute value signal. Bottom: Received signal after matched filtering for a symbol period, $T_{\text{symbol}} = 1$ ms. The packet is flipped due to the channel characteristics.

time receiver and digital signal processing was implemented in order to read the backscattered information sent from the tag. The implemented MATLAB algorithm is available in Appendix A.2. The steps of the algorithm are briefly shown in Fig. 4.7 and the software that was used was Matlab and GNU radio framework. The GNU radio provides the I and Q samples to Matlab through a FIFO file and the samples are interleaved for further processing. The received digitized signal after sampling with a sampling period T_{s}, can be written as:

$$y_{\text{r}}[k] = y_{\text{amb}}(kT_{\text{s}} + \tau_{TR}) = x_{\text{r}}[k] + n[k] = I[k] + jQ[k], \qquad (4.21)$$

with $n[k] = n(kT_{\text{s}})$ and $n[k] \sim \mathcal{N}(0, \sigma_n^2)$. The term $x_{\text{r}}[k]$ is the signal without noise that consists of a DC component, a modulated component and the ambient FM signal utilized for the backscattering. The algorithm collects and process the data in a window with duration: $3 \times$ packet duration.

The first step of the signal processing algorithm is the CFO correction. In our case, CFO is the frequency difference between the FM transmitter and SDR reader and, if not properly removed it causes a performance loss at the receiver. In or-

der to eliminate this term without using an a-priori CFO estimation and correction algorithm, the absolute value $|y_r[t]|^2$ was taken, which is an established CFO compensation technique in digital communication textbooks, such as [87].

A matched filter was then applied to the samples in order to filter out noise and interference terms and maximize the SNR, consisting of a square pulse with duration T_{symbol}. Fig. 4.8 (top) depicts the received packet of Fig. 4.6 after absolute square operation. The same packet after matched filtering is shown in Fig. 4.8 (bottom). Matched filtering was followed by downsampling by a factor of 10 in order to reduce the computational cost of the subsequent operations without compromising the detection quality.

The DC offset of the received window was estimated by averaging some samples when the tag is not transmitting data (average at the start or at the end of the window). The DC offset was removed by subtracting the above estimate from all the values within the receive window. The outcome of this step can be an upright or an inverted waveform. In the case shown in Fig. 4.8 (bottom), an inverted waveform will result after the DC offset removal. Upright or inverted waveforms may result due to the channel propagation characteristics. If an inverted waveform is detected after the DC offset removal, it is flipped so that only upright waveforms y_{fl} are forwarded to the synchronization block.

The received signal must be symbol-synchronized in order to determine when the packet starts. In order to find the starting sample of the packet, cross-correlation with the known preamble symbol sequence (`11010010110100110011`) was used. The similarity of the waveform y_{fl} and the preamble sequence p was evaluated as a function of the time-lag according to:

$$C[n] = \sum_{t=1}^{\infty} p[t]y_{\text{fl}}[t+n], \ n \in [0, N_s/2] \tag{4.22}$$

with N_s the number of received packet samples. The starting point of the packet is defined as:

$$I_{\text{start}}[n] = \arg\max_n C. \tag{4.23}$$

which corresponds to the position of the peak of the cross-correlation between the

known sequence p and the received waveform.

In FM0-encoded signals, the received bits can be determined by comparing two neighbouring symbols. In order to begin decoding, $y_{fl}[t]$ is shifted to sample $I_{start} + P - T_{symbol}$, where P is the length of the preamble. Two possible orthogonal pulse waveforms can be received, as shown in [85] and used in [88]. The two waveforms are indicated in Fig. 4.5, (right) with a solid line square and a dash line square. With this observation the algorithm has to easily decode two adjacent received symbols in order to detect a whole bit. This method gives a gain of 3 dB compared to maximum likelihood symbol-by-symbol detection [89]. The two orthogonal waveforms can be expressed as:

$$D_1[k] = \begin{cases} +1, & \text{if } 0 < k \le \frac{M}{2} \\ -1, & \text{if } \frac{M}{2} < k \le M \end{cases} \tag{4.24}$$

and $D_2[k] = -D_1[k]$ with M the oversampling factor T_{symbol}/T_s. The shifted signal is correlated with $D_1[k]$ and $D_2[k]$ and it is possible to determine which bit has been sent according to [90]:

$$S_k = \begin{cases} 1, & \text{if } \sum_{i=1}^{N_s} y_{sh}[i]D_1[i] > \sum_{i=1}^{N_s} y_{sh}[i]D_2[i] \\ 0, & \text{elsewhere} \end{cases} \tag{4.25}$$

with $y_{sh}[t]$ is the shifted version of waveform $y_{fl}[t]$. The results from the above calculation were stored in a vector L and the estimated bit a_{k+1} that was sent is determined by:

$$a_{k+1} = \begin{cases} 0, & \text{if } L_k = L_{k+1} \\ 1, & \text{elsewhere.} \end{cases} \tag{4.26}$$

It is noticed that the first waveform derived by this decoding procedure is from the last preamble symbol (decoding starting point in Fig. 4.5, right). The following waveforms will be either D_1 or D_2. This means that if the first waveform is D_1 and the second is D_2 and vice versa, the bit "1" was sent, otherwise the bit "0" was transmitted.
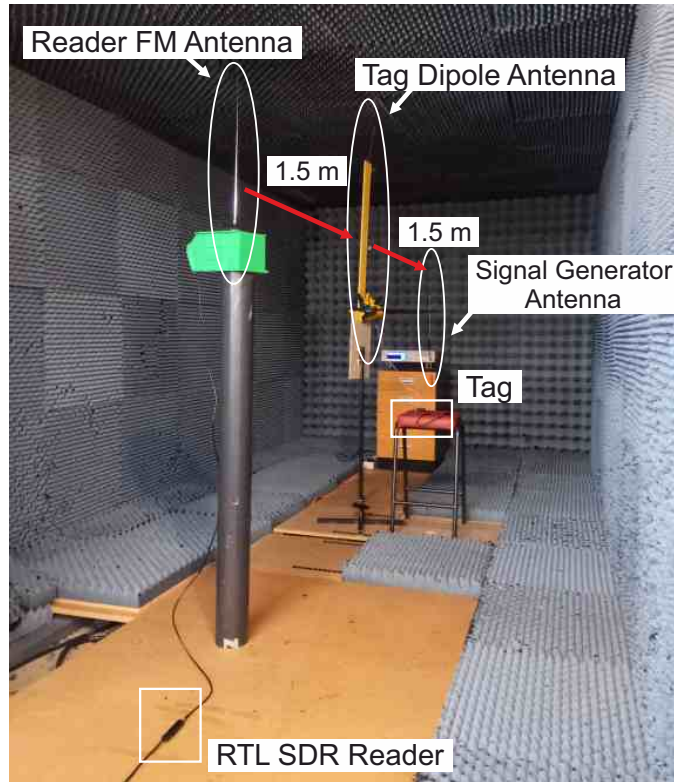
Figure 4.9: Anechoic chamber experimental setup. The receiver antenna was placed at 1.5 m away from the tag and the tag was placed at 1.5 m away from the signal generator.

4.6   Experimental Results

In this work we tried to produce a systematic set of measurements and compare them with the theoretical result of (4.16). For the systematic characterization in a controlled environment the system was demonstrated first in the anechoic chamber of the Heriot-Watt Microwaves and Antennas Laboratory (Fig. 4.9). The tag was placed in a far-field anechoic chamber together with an analog signal generator used as a transmitter (TX). The SDR receiver (RX) was also placed at the edge of the anechoic chamber. The tag, TX and RX are in fixed locations with fixed distances tag-TX 1.5 m and tag-RX 1.5 m. The TX and RX use commercial passive FM antennas with gain 2.5 dBi while the tag antenna is a wire dipole. The anechoic chamber was not specified to work at FM frequencies but it was used to minimize multipath and external interference.

The analog signal generator produces an FM modulated signal with a carrier centered at 98.5 MHz and frequency deviation of 75 KHz. The carrier frequency was selected so as to utilize a frequency band without any interference from any external

stations. We used a sinusoidal signal with a frequency of 15 KHz to modulate the TX carrier. The 15 KHz is equal to the end of mono audio (left and right) signal frequency of a standard stereo FM signal transmission (Fig. 4.2) and that FM stations typically use a 75 KHz deviation [81].

The tag was programmed to send packets with fixed information bits for bit rate: 500 bps. An oscilloscope measurement of the packet transmitted at 500 bps is presented in Fig. 4.6. The data information was the 12-bit binary representation of 965 mV: 001111000101.

The receiver has a bandwidth of 1 MHz around the carrier frequency. The noise power P_w at the receiver was computed over the 1 MHz bandwidth while TX was off. Then, for a given transmit power at the TX, the received power at RX was recorded while the tag was set to a fixed load state A or B, resulting in P_{yH} or P_{yL}. The measured data consist of downconverted time domain values, which were converted in the frequency domain by taking a fast Fourier transform (FFT) and the total power was computed by taking the sum of the squared magnitude values of the FFT operation. It is noted that P_{yH} and P_{yL} correspond to the total signal plus noise power measurement. Two sets of P_{yH} and P_{yL} measurements were collected for a varying transmit power from -55 dBm to -25 dBm. In order to compute an estimate of average power values, for each transmit power, 200 sets of data were collected and an average power value was computed.

The BER was measured for each value of the transmitted power while the tag rate was backscattering a fixed package with bit rate of 500 bps. In addition, the BER was recorded for each transmit power level. The resulting BER vs TX transmit power curves are shown in Fig. 4.10 along with the theoretical BER results (P_e). To calculate the analytical BER, the measured values of P_{yH} and P_{yL} and N_w were used with (4.16). One can see a good agreement between simulation and measurement. BER measurements were performed for transmitted power levels up to -30 dBm where the BER approached 10^{-3}. Due our system memory limitations it was not possible to setup longer measurements containing a sufficient number of data to ensure a good confidence level of BER measurements. The equation that can be rearranged to calculate the number of bits required for a given BER and confidence
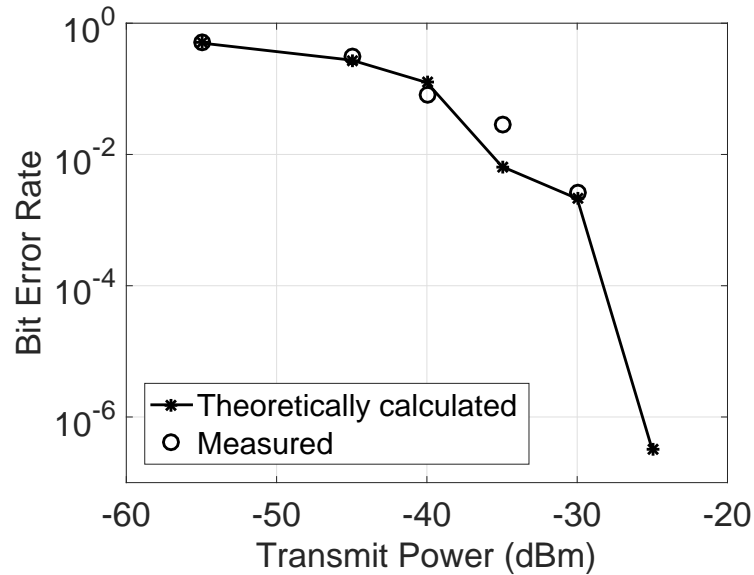
Figure 4.10: Measured and theoretically calculated bit error rate (BER) versus the signal generator transmit power for 0.5 Kbps.

level (C_{L}) is [91]:

$$N_{bits} = \frac{-\ln(1 - C_L)}{BER} \tag{4.27}$$

For example for a typical confidence level of 0.95 the required number of bits to test without any errors is 2.99573×10^7 in comparison to our case that we had only 9616 transmitted bits.

Figure 4.11: Scotland FM radio outdoor deployment. The BBC 95.8 MHz station in "Radio 2" band was selected for measurements. The FM transmitter was 34.5 Km away from the measurement's setup and its transmission power was 250 kW.

The proposed system was also tested indoors in the Heriot-Watt Microwaves and Antennas Laboratory, selecting the most powerful FM station as the ambient RF
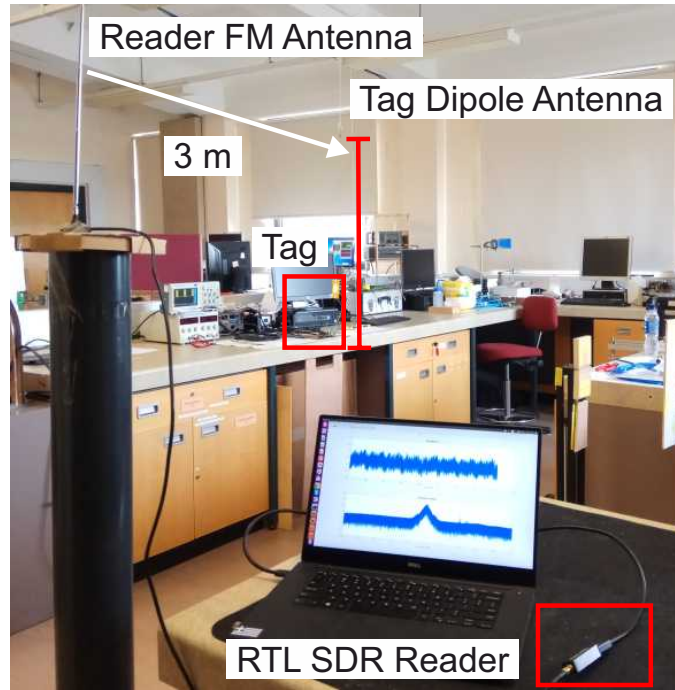
Figure 4.12: Indoor experimental setup. The tag with the FM dipole antenna was set in a vertical position and the receiver was tuned at the most powerful FM station. For communication measurements, the receiver was placed at a maximum of 5 m away from the tag with the receiver antenna on top of a beam.

source to use in backscattering. Thus, the receiver was tuned to BBC 95.8 MHz station with 1 MS/s sampling rate. The station is located 34.5 Km away at the "Black Hill" location between the town of Edinburgh and Glasgow as depicted in Fig. 4.11. The transmission power of the station is 250 kW. The power of the FM station carrier signal was measured in the vicinity of the tag antenna in the lab at -51 dBm. The reader was placed close to the tag at different reader-to-tag distances with a maximum range of 5 m (Fig. 4.12). The antenna of the reader was placed on top of a plastic stick with height 1.5 m for better reception.

The tag was programmed to send packets with the fixed information bits (same as above) for the following different bit rates: 50, 100, 500, 1000, 1250 and 2500 bps. The received packets for 500 bps and 50 bps after the matched filtering step are illustrated in Fig. 4.13 and Fig. 4.14 respectively. One can see that the packets are inverted due to the channel conditions i.e. random, unknown channel phase. It is clear that there is trade-off between bit rate and efficient filtering. In case that a high bit rate is employed (Fig. 4.13), there is less channel fluctuation, and the matched filtering operation is not able to remove the high-frequency components of
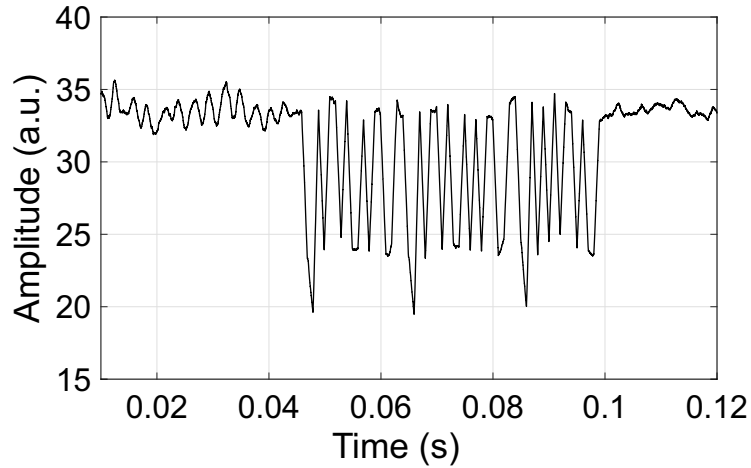
Figure 4.13: Corrected received packet after matched filtering for $T_{\text{symbol}} = 1$ ms (500 bps) featuring a smaller channel fluctuation. High frequency noise components can be observed.

the ambient FM signal, due to the wider bandwidth of the matched filter. In the case of low bit rate transmission (Fig. 4.14) the filtering operation is more effective, corresponding to a higher SNR, but a channel fluctuation effect is visible. When channel fluctuation is present it is more difficult to decode the packet due to the fast varying signal level.

In order to validate the effectiveness of our digital backscatter communication system, numerous range measurements were performed indoors with the setup described above. Figures 4.15 and 4.16 display the BER and PER performance as a function of the tag-to-reader distance for the three different data rates. The minimum PER and BER value at 5 m was measured to be 0.043 and 0.0019 respectively. As the tag-to-receiver distance decreases, the reader can decode successfully more the bit packets. It is also seen that for a given distance value, reducing the bit rate improves the PER and BER performance. As the bit rate goes up the length of each symbol becomes smaller, increasing the probability of a bit corrupted by noise. Thus, the PER and BER goes up. However, transmitting packets at lower bit rates result in increased transmission time and energy per packet while the MCU and the front-end staying in "on" state for longer time. There is a direct and inversely proportional relationship between the bit rate and the energy that a tag consumes sending a packet as shown in Table 4.1, where the energy per packet for six bit rates is presented. The table also provides the tag power consumption for each bit rate.
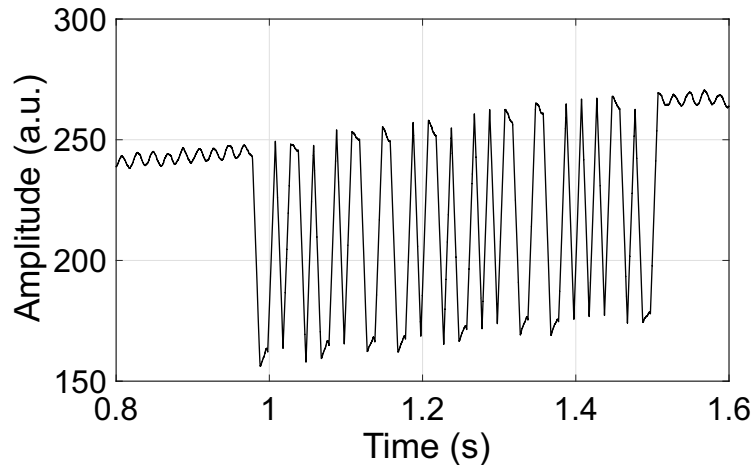
Figure 4.14: Corrected received packet after matched filtering for $T_{\text{symbol}} = 10$ ms (50 bps) including the channel fluctuation effects. A better filtering quality is observed.

Table 4.1: Binary Tag Power Characteristics.

Bit Rate (bps)	Power (mW)	Energy/Packet (μJ)
2500	2.838	36.9
1250	2.087	43.4
1000	1.785	46.4
500	1.283	66.73
100	0.751	195.45
50	0.677	352.15

A higher power consumption of the MCU electronics is observed when operating at a higher bit rate. In order to compile the measurements shown in Table 4.1, the tag was programmed to wake up every 3 sec, transmit a packet and go to sleep mode, while being powered from the super capacitor.

Finally, the potential interfering effects of ambient backscatter systems on the performance of the ambient systems it utilizes should be considered. In U.S.A., according to the Federal Communications Commission (FCC), it is illegal to broadcast unlicensed signals on FM band (88 MHz to 108 MHz) [92]. However, devices that communicate with backscatter signals (e.g. RFID tags) have not been reviewed by FCC. The reason is that the RF front ends of backscatter tags are not active components (have no amplifiers) and they only modulate the reflections of the incoming signals. Consequently the power of the reflected signals is of very low levels. The ambient backscatter operation such as our developed system belongs to the category
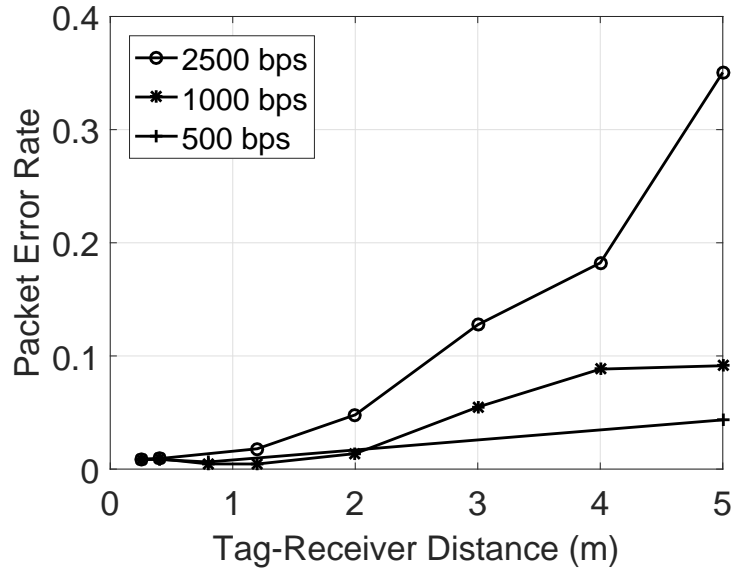
Figure 4.15: Measured packet error rate (PER) versus the tag-receiver distance for 0.5, 1 and 2.5 Kbps.

of RFID tags so it is not illegal under current rules. However, the reflected signals of existing FM signals could interfere with commercial FM receivers. Experimentally it was observed that the transmissions did not affect typical FM receivers, due to the low power level of ambient backscatter signals, and the different type of modulation (ASK). The commercial FM receivers detect the FM signals and we use ASK to modulate our information. We used a smartphone FM Receiver (Xiaomi redmi note 4) with headphones as receiving antenna in order to test the interference of the system. For the testing, we programmed the tag in the worst case scenario where always backscatters random data. The transmit antenna of the tag was placed parallel next to the FM receiver antenna (headphones). When we turned on the FM Receiver we didn't observe any noticeable glitches in the sound. This is only a simple experiment, and a detailed experimental study is required to determine the level and limits of interference generated by ambient backscatter.

4.7   Conclusion

In this chapter, we presented a novel FM backscatter tag and receiver system. The tag communicates with a low cost SDR reader by backscattering the ambient FM signals. Data acquisition from sensors with low power operation and communication
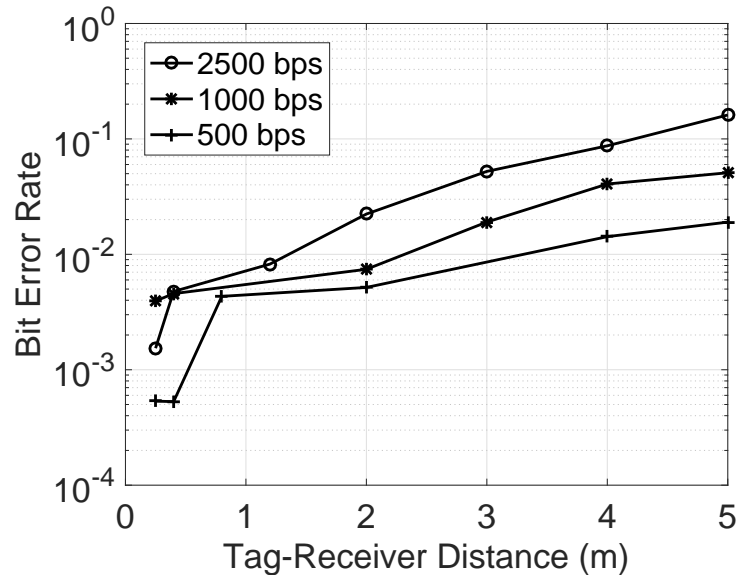
Figure 4.16: Measured bit error rate (BER) versus the tag-receiver distance for 0.5, 1 and 2.5 Kbps.

ranges up to 5 m has been demonstrated experimentally. The communication was implemented with OOK modulation over the modulated carrier of the most powerful FM station. This concept can be the next novel way for low power and low cost long range communication.

The tag that is proposed is semi-passive (i.e., battery-assisted) tag which means that the tag uses super capacitor or battery to communicate with the reader. With the utilization of the bistatic topology and semi-passive tags that communicate with a low bitrate, it is possible to implement large-scale networks, in the fields comprising of low-cost sensor/tags. In this work, the communication scheme is simplified since it requires only a receiver eliminating the need for CW emitters. The receiver is also low cost and low power compared with the RFID readers of the market. The tag cost of the proposed work, compared to classic WSNs sensor node is significantly lower since the RF front-end is composed of a single transistor-switch. Using off-the-shelf electronic components, resulted in the relatively low cost in terms of bill of materials (BOM) of approximately 15 EUR per tag. For example, if we want to cover a big field with 100 tags and we use custom soil moisture sensors, the overall cost of sensor nodes will be $15 * 100$ EUR. Also, we will need one reader (20 EUR) and a computer or smartphone for reader connectivity. Multiple access of tags in time domain will be studied in future work.

Chapter 5

High Order Modulated Ambient Backscatter

5.1 Introduction

Existing ambient RF signals have been proposed for backscatter communication instead of a CW emitter signal [93]. This approach simplifies the complexity and cost of the system and its deployment. In [73] for the first time high order modulation was introduced for ambient backscattering communications. The authors demonstrated 4-FSK modulation to transmit two bits per symbol over the ambient FM signals with a maximum data rate 3.2 kbps. The work involves simulation of an integrated circuit for the tag, while for the prototype an AWG was used connected with an RF front-end. In [94], a backscatter PSK hardware prototype is presented that combines a 4-PSK transmitter, an energy harvester and a multi-level voltage detector. Two similar prototypes can communicate with data rate of 20 kbps using an ambient signal from UHF TV band. In [95] a dual-band 4-QAM backscatter modulator circuit was proposed for ambient signals. It is composed by two transistors and a dual-band Wilkinson power divider, following the same principle proposed in [17]. The modulator presents an average power consumption of 27 nW for 500 kbps of data rate at 900 MHz and 2.45 GHz (cellular and WiFi frequencies).

Chapter 4 demonstrates a tag capable of transmitting FM reflections to a computer or a tablet through a low-cost SDR reader. The tag uses ASK binary modulation with FM0 encoding on ambient FM station signals as in commercial RFID

systems. The FM transmitter was 34.5 Km away from the measurement's setup and a 5 m communication range between the tag and the reader was achieved with 2.5 Kbps bit rate. A theoretical analysis of the error rate performance also provided.

In this chapter we consider high order amplitude modulation and we demonstrate the first prototype suitable for ambient backscatter communication deployment working with 4-PAM. The FM frequencies were selected due to the strong ambient signal source that can be used for backscatter communication. The 4-PAM modulation is used to double the bit rate, compared to a 2-PAM system. With amplitude modulation the complexity of the receiver and the tag can be drastically simplified as there is no need for a different frequency for each symbol. Tag and receiver are more complex as variation of modulating signal has to be converted and detected from corresponding variation in frequencies.

Preliminary results were presented in previous work [96], where 4-PAM scheme was selected due the low hardware complexity and low power consumption. This work is an extensive presentation of the FM backscatter system in [96] thus theoretical analysis of the system is provided as well as a real time receiver implementation. Additional details about the tag are also provided. In particular, our tag employs a single low cost transistor and a telescopic antenna achieving communication with low bit rate for reduces power consumption. This work differs from [16, 17] since it uses ambient FM signals as the carrier instead of an intentionally transmitted unmodulated CW signal. The use of FM signals on the receiver increases the complexity of selecting the thresholds associated with demodulation, as explained below in section 5.5. In particular, we present a tag consisting of a MCU with a DAC and an ADC. The tag could collect data from sensors through the ADC and process them. The MCU creates the modulation pulses internally and controls the RF front-end transistor via the DAC. A low cost SDR receiver is used similarly to chapter 4.

This chapter is structured as follows: section 5.2 reviews the principles of the proposed backscatter modulation scheme. Section 5.3 describes the tag hardware implementation. Section 5.4 provides the theory and performance analysis of the FM ambient 4-PAM technique. Section 5.5 discusses the theory and the receiver implementation. In section 5.6, the proof-of-concept experimental communication
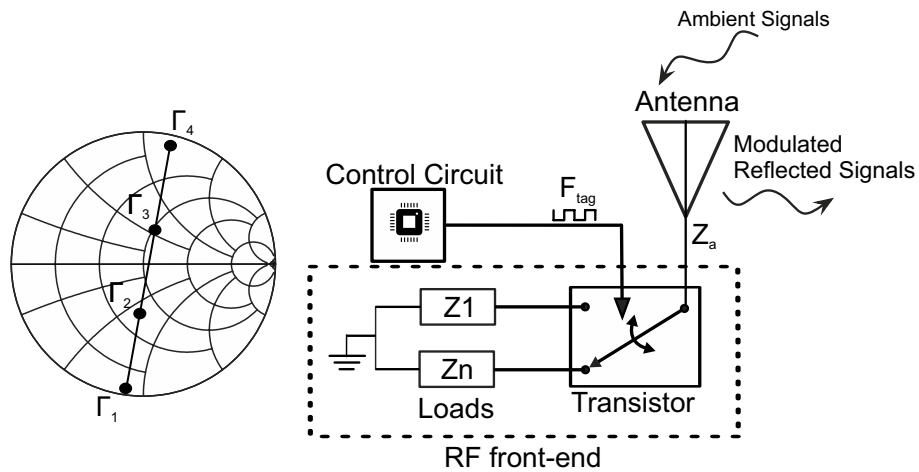
Figure 5.1: Backscatter radio principle: An RF transistor alternates the termination loads Z_i of the antenna corresponding to different reflection coefficients Γ_i. Four reflection coefficients ($n = 4$) could create a four pulse amplitude modulation (4-PAM).

results are presented. Section 5.7 provides the comparison of our work with other similar high order modulation works. Finally, section 5.8 concludes this work.

5.2 High Order Backscatter Modulation

In system of chapter 4, an RF switch was directly connected to the RF front-end antenna in order to create the two discrete states. For high order modulations, the number of states have to be increased and the RF circuit must create a specific discrete impedance for each transmitted symbol. For this purpose, a single RF transistor circuit can be used as an active load in order to create different impedances for the PAM constellation [17]. In this work an enhancement mode pseudomorphic high electron mobility transistor (E-pHEMT) was used to implement a circuit compatible with a 4-PAM scheme. The RF circuit presents four distinct impedance values for a four different gate voltages. A given antenna with impedance Z_a connected to a complex load with impedance $Z_i \in \{Z_1, Z_2, Z_3, Z_4\}$, is associated with a reflection coefficient obtained from equation 2.1. By changing the gate voltage of the transistor, four distinct reflection coefficients can be achieved corresponding to the four symbols. The performance of PAM modulation is optimized when the Γ_i values lie equidistantly along a straight line on the Smith Chart (Fig. 5.1, left) [17]. Considering the above, we can select the desired values of the reflection coefficients; an

Table 5.1: 4-PAM Modulation Parameters

Γ_i	Symbol	Bits	V_{gate} (mV)
$-0.7245 - j0.6922$	-3	00	0
$-0.3414 - j0.2881$	-1	01	333
$+0.0223 + j0.1779$	$+1$	11	387
$+0.3079 + j0.6334$	$+3$	10	600

example of four equidistant measured values on the same line is shown in Table 5.1. Using this table and (2.1), the desired voltage values at the transistor gate can be obtained. The received signal can be expressed with the complex baseband form (2.2) from chapter 2.

5.3 Tag Design
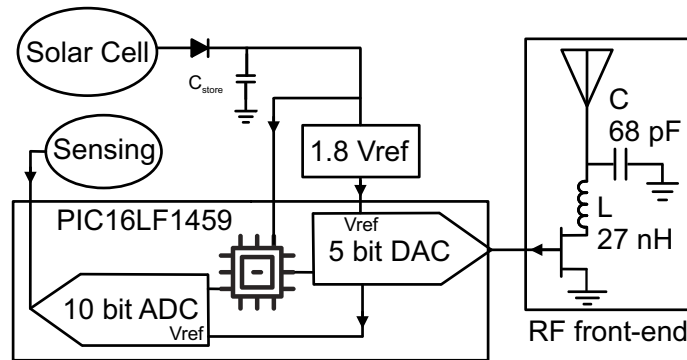
Figure 5.2: Schematic of Proof-of-concept tag. A low power micro-controller reads the sensors and controls the RF front-end circuit.

Our tag consists of an ultra low power MCU connected with an RF front-end as it is depicted in the block diagram of Fig. 5.2. The 8-bit PIC16LF1459 MCU from Microchip Inc. was used, whitch consumes 25 μA/MHz of current at 1.8 V [46]. The clock of the MCU was programmed at 32 KHz in order to minimize the power consumption of the tag. The MCU also has a sleep mode operation with current consumption of 0.6 μA. The MCU includes a 10 bit ADC and collects data from analog sensors on the tag. The 5-bit DAC of the MCU is used in our application to drive the RF front-end transistor with different voltages. The DAC has the ability to supply the gate of the transistor with 32 distinct voltage levels in order to change the antenna load impedance. Fig. 5.3 depicts the tag power consumption for all the possible DAC output voltages when the MCU was supplied by a 1.8 V voltage
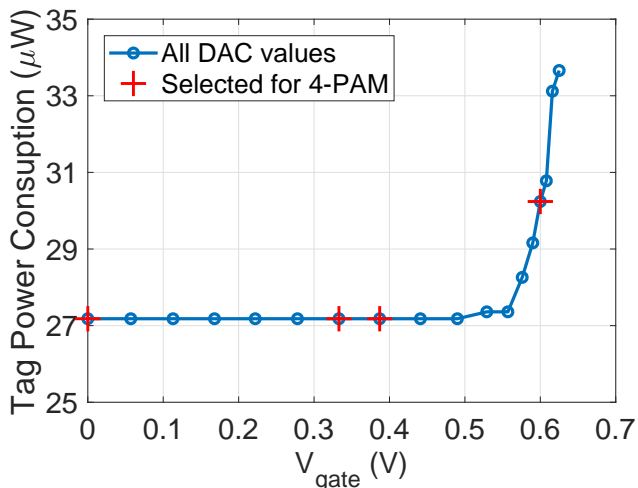
Figure 5.3: Digital-to-Analog Converter output voltage versus the tag power consumption. The tag was measured at 1.8 V when the ADC was turned off. Four optimal values were selected for the backscatter communication.

source. The figure shows the voltages up to 0.625 V, since the maximum voltage for the transistor (DAC output), in our application was 0.6 V. Four DAC outputs were selected for our backscatter modulation scheme as it is explained in more details below. The tag was powered by the flexible solar panel, SP3-37 provided by PowerFilm Inc. [54]. The solar panel charges a 220 μF tantalum capacitor instead of a battery through a low-voltage-drop Schottky diode. An external voltage reference IC XC6504 [48] was also used to supply the tag with a stable voltage (V_{ref}) 1.8 V. The proposed sensor node does not focus on a specific sensing application or power management system but only on the novel telecommunication part of the system. An RF harvester could be designed in the future [97] to charge the capacitor during the night in combination with solar cell during the day [53]. Another idea is an integrated cooperative harvester capable of collecting both electromagnetic and kinetic energy simultaneously as proposed in [98].

The RF front-end consists of the ATF52189 RF E-pHEMT from Broadcom [99] and the SRH788 monopole antenna. The maximization of the magnitude of complex reflection coefficient differences between the four states is a main objective for optimized backscatter communication [100]. In this work, a core RF circuit challenge was to achieve the desired change of the drain impedance by varying the voltage at the gate in the range between 0 to 0.6 V. The Advanced Design System (ADS) from Keysight was used for the optimization of the RF front-end circuit. The simu-
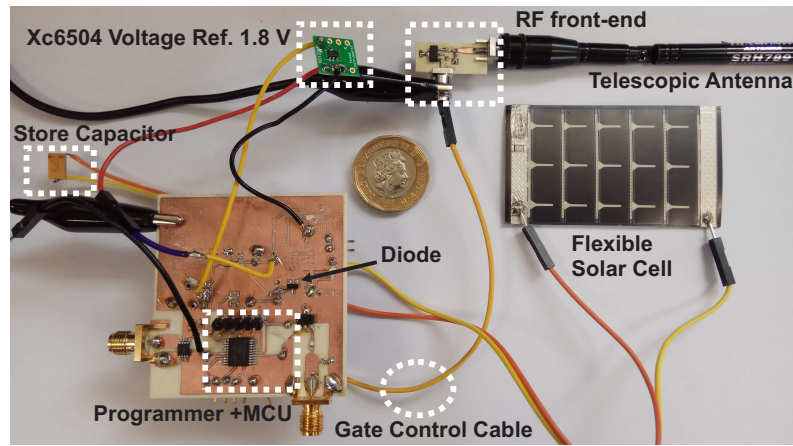
Figure 5.4: The fabricated tag prototype with the RF front-end board. The tags is powered by a solar panel.

lations performed involved the variation of the gate voltage at the transistor from 0 to 0.6 V with a sweep of 0.01 V from 87.5 MHz to 108 MHz. More specifically the large-signal S-parameter simulation was used to perform the backscatter modulation in order to maximize the distance between the consecutive Γ_i values. Following the aforementioned optimization procedure, the matching network between the transistor and the antenna was composed by a capacitor and an inductor as depicted in the schematic of Fig. 5.2. In the simulation we assumed that we have a ideal 50 Ohm antenna connected with our RF front-end and the optimum component values were found to be 68 pF and 27 nH.

The RF front-end board was fabricated on Astra MT77 substrate with thickness 0.762 mm, $\varepsilon_r = 3.0$ and $tan\delta = 0.0017$. The main board of the proof-of-concept tag that integrates the MCU was fabricated on a Rogers RO4350B substrate. The fabricated prototypes and the solar panel are shown in Fig. 5.4. As mentioned, the output of the DAC was connected with the gate of the transistor on the RF front-end. The fabricated RF front-end board was measured using a vector network analyser (VNA) with $P_{in} = -20$ dBm at the frequencies of the FM band, $87.5 - 108$ MHz. Each DAC output corresponds to a specific reflection coefficient Γ_i and all the possible voltages of Fig. 5.3 were tested through the VNA. Four voltages: 0, 333, 387 and 600 mV were found as the optimum values to supply the gate of the transistor and create the 4-PAM modulation. The selected values are also depicted in Fig. 5.3 creating four impedances or symbols for a specific frequency. The measured Γ_i using the four voltages in the FM band are presented in Fig. 5.5.
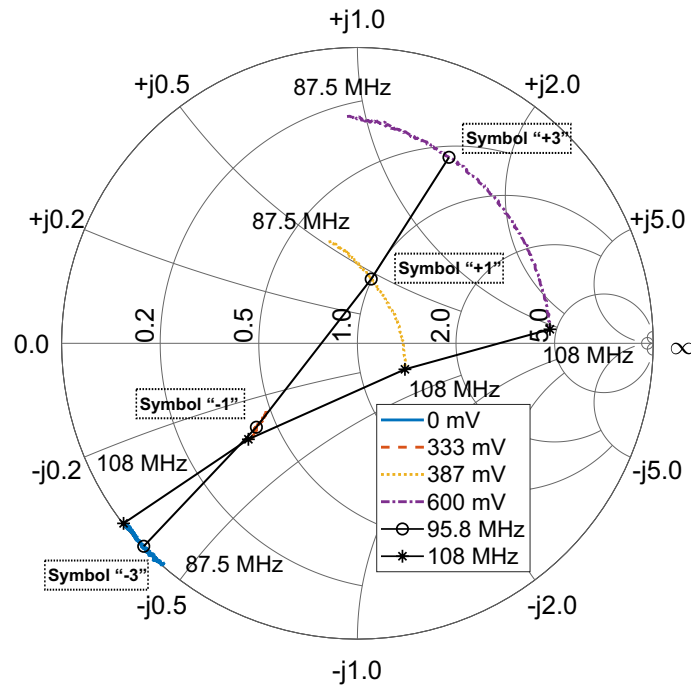
Figure 5.5: Smith Chart with measured reflection coefficient values for 4 different voltage levels at the gate of transistor. The Pin was fixed at -20 dBm for frequencies $87.5 - 108$ MHz.

As it is observed, the selected voltage values offer almost equal distances between the corresponding Γ_i. The prototype board was also tested at -10 dBm and -30 dBm and the outcomes were similar with the results of Fig. 5.5. Table 5.1 also shows the resulting Γ_i in combination with the symbols, the bits and the gate voltages at a fixed frequency of 95.8 MHz. Using the four voltages at the gate of the transistor and sweeping the frequency it is possible to observe that each state corresponds to an "arc" on the Smith Chart. In particular, the set of four states (each line in Fig. 5.5) rotates clockwise as the frequency increases. As per the design target, equal distances between the symbols were achieved assuming antenna input impedance equal with 50 Ohms, in order to maximize the SNR and thus the efficiency of the PAM modulation. It is noted that our tag is a semi-passive design where the available capacitor powers the MCU during transmission from the tag to the reader. According to [100, 101] for semi-passive tags, the two pairs of symbols and (-1, +1) must be diametrically opposite on two unit circles.
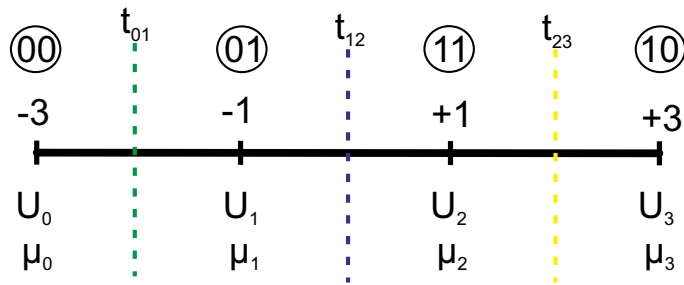
Figure 5.6: The 4-PAM symbols. Three thresholds are calculated for the decision.

5.4   Ambient FM 4-PAM Modulation

Pulse Amplitude Modulation (PAM) is a method of sending information by scaling a pulse shape with the amplitude of the symbols and duration T_{symbol} [102]. In the 4-PAM there are four symbols and each symbol corresponds to a pair of two bits. Each bit duration is denoted as T_{bit} and the data bit rate is $2/T_{\text{bit}}$ bits per second (bps). According to 4-PAM it is possible to transmit two bits with each symbol/pulse, for example, by associating the amplitudes of -3,-1,+1,+3, with four bit choices 00, 01, 11, and 10 (Table. 5.1). The symbols $\pm 1, \pm 3$ are shown in Fig. 5.6 and the bit representation of the symbols is Gray coded [45]. In order to transmit a digital stream, it must be converted into an analog signal. After conversion of the bits into symbols, the analog form of a 4-PAM modulation signal can be expressed as:

$$\Gamma_{\text{i}}(t - \tau) = \sum_{n=0}^{N-1} x_n \Pi[t - nT_{\text{symbol}} - \tau] \tag{5.1}$$

where $x_n \in \{-3, -1, +1, +3\}$, N is the number of transmitted symbols and $\Pi(t)$ is a pulse with duration T_{symbol}. Thus, each member of the 4-PAM data sequence is multiplied by a pulse that is non-zero over the appropriate time window.

The proof-of-concept tag was set up to send a fixed bitstream packet format. In this work the fixed bit sequence was: 10001000100111−00−01−0111100011 which is translated to symbol sequence: +3−3+3−3+3−1+1 −3 −1 −1+1+3−3+1. Transmission of some known preamble data is required at the receiver to identify the beginning of a frame (packet) at the transmission. Here the first seven symbols (14 bits) were added before the message sequence as a preamble. The symbols of the preamble are used also as training symbols as explained below. After the preamble, "Tag Number" bits (2 bits), "Sensor Number" bits (2 bits) and "Sensor Data" bits (10 bits) follow.
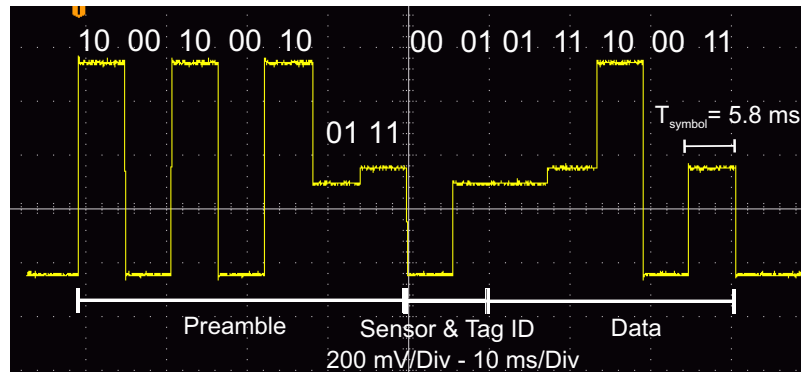
Figure 5.7: An oscilloscope measurement of the sending packet. Voltage levels correspond to the 4-PAM symbols at the gate of the transistor are presented.

The "Tag Number" bits were utilized in case that four different tags will be used in a future wireless sensor network. With this allocation, the tag could support up to four sensors and the "Sensor ID" part is used to identify the sensor number. The last 10 bits section is used for transmitting the sensor data. An example of the transmitted packet is depicted in Fig. 5.7 and more bits could be added in order to include extra sensors or tags.

5.5 Receiver

5.5.1 Receiver Theory

FM radio stations typically operate in the range of frequencies from 88 MHz to 108 MHz and use frequency modulation in order to transmit the audio signals. The FM signals are described in chapter 4 and are given by the formulations x_{FM} and $m(t)$ of the section 4.2.1. In our case, an FM modulated signal is used for communication instead of a CW signal and the complex baseband received signal is described by $y_{\text{amp}}(t)$ signal in (4.3) and contains the rectangular pulses of (5.1). Initially, a similar procedure as in section 4.4 is followed at the receiver. The signal $Z(t)$ from equation (4.12) is correlated with a pulse $q(t) = 1$ for $0 < t \leq T_{\text{symbol}}$ and a synchronization procedure is then applied in order to identify the stating point of the frame. A DC removal is required for the synchronization; since the DC term does not contribute with any information on the transmitted data, it can be ignored in the remaining of the receiver processing. The obtained signal can be expressed

as:

$$U_i = X_i + V_i = \int_0^{T_{\text{symbol}}} A^2 |h(t)|^2 q(t) \mathrm{d}t + \int_0^{T_{\text{symbol}}} w(t) q(t) \mathrm{d}t. \qquad (5.2)$$

Using the 4-PAM modulation, $|h(t)|^2$ can take four values ($h_i(t)$) with $i \in \{1, 2, 3, 4\}$ and thus V_i is a Gaussian process:

$$V_i \sim \mathbb{N} \left(T_{\text{symbol}} N_w, T_{\text{symbol}}^2 N_w^2 + 2 T_{\text{symbol}}^2 A^2 N_w |h_i|^2 \right). \qquad (5.3)$$

Using $X_i = T_{\text{symbol}} A^2 |h_i|^2$ it is straightforward to show that U_i is a Gaussian process with $U_i \sim \mathbb{N}(\mu_i, \sigma_i^2)$. The mean and variance are analysed as:

$$\mu_i = T_{\text{symbol}} A^2 |h_i|^2 + T_{\text{symbol}} N_w, \qquad (5.4)$$

$$\sigma_i^2 = T_{\text{symbol}}^2 N_w^2 + 2 T_{\text{symbol}}^2 A^2 N_w |h_i|^2. \qquad (5.5)$$

Our system works in non-coherent mode where the algorithm does not perform synchronisation between receiver and transmitter. A non-coherent algorithm does not use phase and frequency estimation techniques that add complexity and rate loss at the receiver [103].

For the symbol detection the minimum distance (Maximum-Likelihood) rule is used thus no a priori information on the transmitted symbols is available for our system [45]. The decision boundaries and the transmitted constellation for a given measurement U_i, $i \in \{0, 1, 2, 3\}$ are depicted in Fig. 5.6. Three decision boundaries t_{01}, t_{12} and t_{23} are located between the subsequent symbols. They quantise the signal values as decisions are taken by comparing by comparing them with the thresholds. If the symbol error probability can be defined as P_e we can also evaluate the BER as:

$$P_b = \frac{P_e}{2} = \frac{1}{8} \sum_{i=0}^{3} P_{e,i} \qquad (5.6)$$

with $P_{e,i}$ the error probability of each symbol. For example, when the symbol -3 was sent, the probability of error is the probability to decide in the right side of threshold t_{01} (Fig. 5.6) and it is defined as $P(U > t_{01}|U_0)$. The conditional error probability

for each symbol can be calculated and simplified using Q-function accordingly:

$$P_{e0} = P(U > t_{01}|U_0) = Q\left(\frac{t_{01} - \mu_0}{\sigma_0}\right),$$

$$P_{e1} = P(U > t_{12}|U_1) + P(U \leq t_{01}|U_1) = Q\left(\frac{t_{12} - \mu_1}{\sigma_1}\right) + Q\left(\frac{\mu_1 - t_{01}}{\sigma_1}\right),$$

$$P_{e2} = P(U > t_{23}|U_2) + P(U \leq t_{12}|U_2) = Q\left(\frac{t_{23} - \mu_2}{\sigma_2}\right) + Q\left(\frac{\mu_2 - t_{12}}{\sigma_2}\right),$$

$$P_{e3} = P(U \leq t_{23}|U_3) = Q\left(\frac{\mu_3 - t_{23}}{\sigma_3}\right)$$

(5.7)

where $Q(x) = \frac{1}{\sqrt{2\pi}}\int_x^\infty e^{-t^2/2}dt$ the Q function. For two adjacent conditional probabilities we can assume that:

$$P(U = t_{01}|U_0) = P(U = t_{01}|U_1) \tag{5.8}$$

which is expressed as:

$$\frac{1}{\sigma_0\sqrt{2\pi}}e^{-(t_{01}-\mu_0)^2/2\sigma_0^2} = \frac{1}{\sigma_1\sqrt{2\pi}}e^{-(t_{01}-\mu_1)^2/2\sigma_1^2} \tag{5.9}$$

thus U_0, U_1 are Gaussian as it was mentioned before. Using the above equality the threshold t_{01} can be easily calculated as:

$$t_{01} = \frac{\sigma_1^2\mu_0 - \sigma_0^2\mu_1}{\sigma_1^2 - \sigma_0^2} \pm \frac{\sqrt{\sigma_1^2\sigma_0^2\left[(\mu_1 - \mu_0)^2 + (\sigma_1^2 - \sigma_0^2)\ln\frac{\sigma_1^2}{\sigma_0^2}\right]}}{\sigma_1^2 - \sigma_0^2}. \tag{5.10}$$

It is clear that the threshold t_{01} is a function of μ_0 and σ_0 parameters and in practice it depends on time-varying received SNR. It is noticed that since $\mu_0 < t_{01} < \mu_1$ only one of the two above solutions is valid for the detection. Also it can be observed that if $\sigma_0^2 = \sigma_1^2$ the threshold can be simplified as $t_{01} = (\mu_0 + \mu_1)/2$ and it is located in the middle between the two symbols. Following the same derivation, the other

two thresholds t_{12} and t_{23} are calculated similarly:

$$t_{12} = \frac{\sigma_2^2\mu_1 - \sigma_1^2\mu_2}{\sigma_2^2 - \sigma_1^2} \pm \frac{\sqrt{\sigma_2^2\sigma_1^2\left[(\mu_2 - \mu_1)^2 + (\sigma_2^2 - \sigma_1^2)\ln\frac{\sigma_2^2}{\sigma_1^2}\right]}}{\sigma_2^2 - \sigma_1^2},$$

$$t_{23} = \frac{\sigma_3^2\mu_2 - \sigma_2^2\mu_3}{\sigma_3^2 - \sigma_2^2} \pm \frac{\sqrt{\sigma_3^2\sigma_2^2\left[(\mu_3 - \mu_2)^2 + (\sigma_3^2 - \sigma_2^2)\ln\frac{\sigma_3^2}{\sigma_2^2}\right]}}{\sigma_3^2 - \sigma_2^2}.$$

$$(5.11)$$

Next, a simple estimation approach is proposed for the calculation of the decision thresholds. If we assume high SNR for our received signal and thus $T_{\text{symbol}}A^2|h_{\text{i}}|^2 \gg T_{\text{symbol}}N_{\text{w}}$ we can say that:

$$\mu_{\text{i}} \sim T_{\text{symbol}}A^2|h_{\text{i}}|^2, \sigma_{\text{i}}^2 \sim 2N_{\text{w}}T_{\text{symbol}}\mu_{\text{i}}. \tag{5.12}$$

Using the above, the threshold of (5.17) can be simplified as:

$$t_{01} \approx \frac{\sigma_1\mu_0 + \sigma_0\mu_1}{\sigma_1 + \sigma_0}. \tag{5.13}$$

The other two thresholds can be approximated as:

$$t_{12} \approx \frac{\sigma_2\mu_1 + \sigma_1\mu_2}{\sigma_1 + \sigma_2}, t_{23} \approx \frac{\sigma_3\mu_2 + \sigma_2\mu_3}{\sigma_2 + \sigma_3}. \tag{5.14}$$

Having the three thresholds, we can take the decision and ML method performs independent detection of the four double-bit symbols according to decision areas of Fig. 5.6. The detection method is explained below:

- Decide X_0 from U_0 if $U < t_{01}$.
- Decide X_1 from U_1 if $t_{01} < U < t_{12}$.
- Decide X_2 from U_2 if $t_{12} < U < t_{23}$.
- Decide X_3 from U_3 if $t_{23} > U$.

5.5.2 Receiver Implementation

In this chapter, the low cost RTL SDR of section 2.6 was used as receiver. It was connected with a telescopic monopole antenna for FM signals reception. The gain of the monopole is 2.15 dBi from 5 to 300 MHz. The sampling rate of the SDR
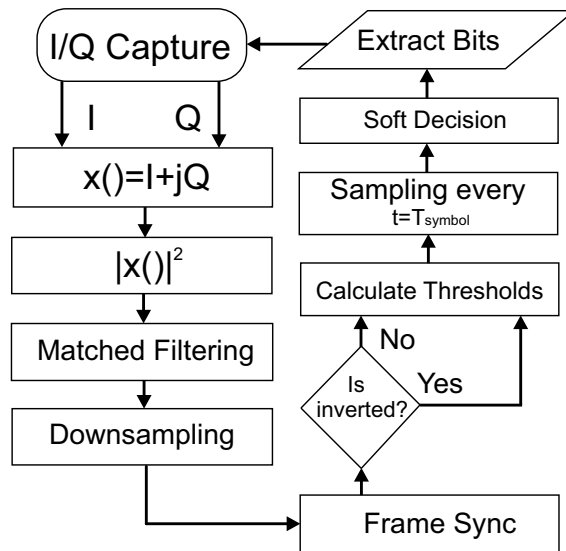
Figure 5.8: Flowchart of the receiver algorithm implemented in MATLAB software.

was fixed at 1 MSps for this work. At 98.5 MHz the sensitivity of the receiver was estimated at -129 dBm [104] and this makes it suitable for our low cost application.

A modified version of previous algorithm in section 4.5 was used for our real-time receiver algorithm. The flowchart of the 4-PAM receiver is shown in Fig. 5.8 and the MATLAB algorithm is available in Appendix A.3. The algorithm captures data in a specific time window equal with $3 \times$ packet duration and packet duration $= 14 * T_{\text{symbol}}$. The baseband received signal can be expressed using the (4.21). that includes the modulated useful information and a component based on the FM message. The absolute squared value of $y_r[k]$ was taken and a matched filtering was utilized to maximize the SNR. The matched filter is a square pulse signal with T_{symbol} duration and acts as a low-pass filter that removes out-of-band signals. Fig. 5.9 (a) shows an example of a received packet in time domain after the absolute square operation. The packet after the low-pass filtering is depicted in Fig. 5.9 (b). The packet was captured using a real FM station in an indoor demo as it is explained in section 5.6. It can be observed that the packet also includes spurious/noise signals from the building environment.

Following the same steps of previous chapter, a downsampling operation by a factor of 10 was applied in order to reduce the computational complexity of the following steps without compromising the detection quality. Proper decoding requires locating where the frame starts and this step is called frame synchronization. Cross-correlation was used for the synchronization with a known preamble sequence
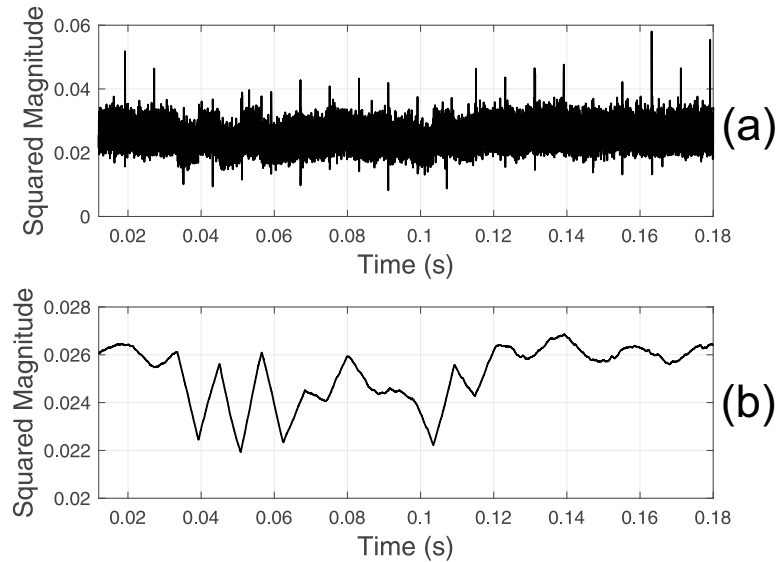
Figure 5.9: Received packet signal. a) Signal after squared absolute operation and b) signal after matched filtering for $T_{\text{symbol}} = 5.4$ ms.

10-00-10-00-10-01-11. As it is observed the preamble includes all the symbols at least once and in this work, it is used also for training. In particular, the group of training symbols are send prior to the useful data symbols and they are useful for calculation of the thresholds. More specifically it consists of seven symbols and the last four of them are used to estimate the μ_i and σ_i of each symbol and thus the three thresholds. During synchronization, it is also detected if the signal is an inverted waveform or not. An inverted waveform (Fig. 5.9) results due to the multipath channel characteristics and the high level of the signal has become low and vice versa. This is detected through the comparison of the detected preamble bits with our a priori known preamble and the inverse known preamble [90]. The correlation operation that returns the maximum result, indicates where the packet starts and if it is inverted or not. The inversion is position-dependent and this information is required for the next step.

Three amplitude thresholds are calculated using the theoretical formulations of (5.13) and (5.14). For each packet coming at the receiver it is necessary to calculate different thresholds and thus different μ_i, σ_i values. In Fig. 5.10, the estimated thresholds for the signal of Fig. 5.9 are depicted. The thresholds are inverted because our initial signal was inverted.

Next, the algorithm quantizes the received signal based on the three thresholds.
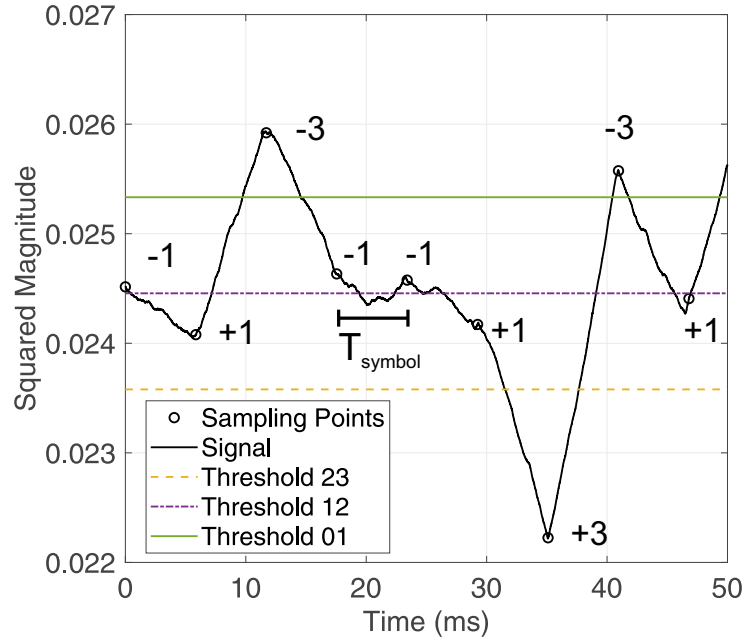
Figure 5.10: Received packet without the preamble after matched filtering. The respective symbols can be decided using three thresholds.

Samples every T_{symbol} are taken and compared with threshold(s) to determine the recovered data symbols. A transmitted symbol is determined if the sample corresponds to its specific symbol region. In Fig. 5.10 is depicted the useful signal of Fig. 5.9 without the preamble bits and a specific symbol/region corresponds to a received sample for a given T_{symbol}. Finally, a quantizer makes the decisions that are then decoded back from symbols to the bits of the message. In Fig. 5.10 can be observed that the distances between symbols are not equal or maximized instead of the Γ_i in Fig. 5.5. In the RF front-end design we assumed that the antenna is matched to 50 Ohms and we used a commercial antenna afterwards. The monopole antenna was not well matched thus the GND plane of our RF front-end was small, and this leads to a discrepancy from the desired reflection coefficients. As a result, there is a corresponding reduction in the distance between the symbols and thus performance degradation. As part of future work, we will optimize the bias points taking into account the measured antenna impedance values.
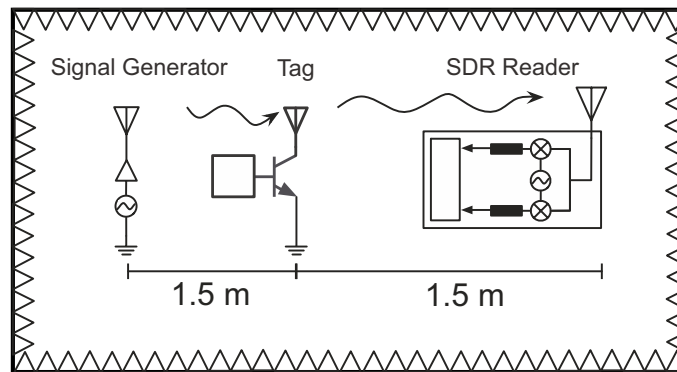
Figure 5.11: Schematic of the experimental setup in the anechoic chamber. The transmitter-to-tag distance and the tag-to-reader distance were 1.5 m.

5.6 Measurement Results

In order to evaluate telecommunication measurements for our system, the proof-of-concept tag prototype was programmed to produce a fixed packet bit-stream at the DAC output. The symbol representation of bit-sequence was described above and it is depicted in Fig. 5.7. The figure is an oscilloscope measurement and shows the four voltage levels of the transmitted symbols that are used to drive the transistor. The T_{symbol} was fixed at 5.8 ms and thus the bit rate is calculated at 345 bps. It can be observed that a small variation between the gate voltages corresponding to the states −1 and +1 occurs. This variation does not correspond to small variation in Γ_i but leads to the maximum distance between Γ_1 and Γ_2 as it is shown in Fig. 5.5. This is due to the non-linear relationship between the transistor gate voltage and the corresponding Γ_i.

To test the performance of the backscatter communication link we first demonstrated our system in a controlled environment (anechoic chamber). The same setup, lab equipment and configuration with our previous section 4.6 was used. The RF front-end antenna was placed 1.5 m away from the receiver antenna while the FM generator antenna was 1.5 m way from the tag. The generator and the reader use commercial passive FM antennas with gain 2.15 dBi. For our deployment we used the bistatic architecture where the illuminating CW emitter and the receiver of the reflected signals are distinct units, located at different positions. The bistatic topology is showed in Fig. 5.11 and the signal generator was set at 98.5 MHz. Different transmit power levels were recoded at the generator while the tag was set to send
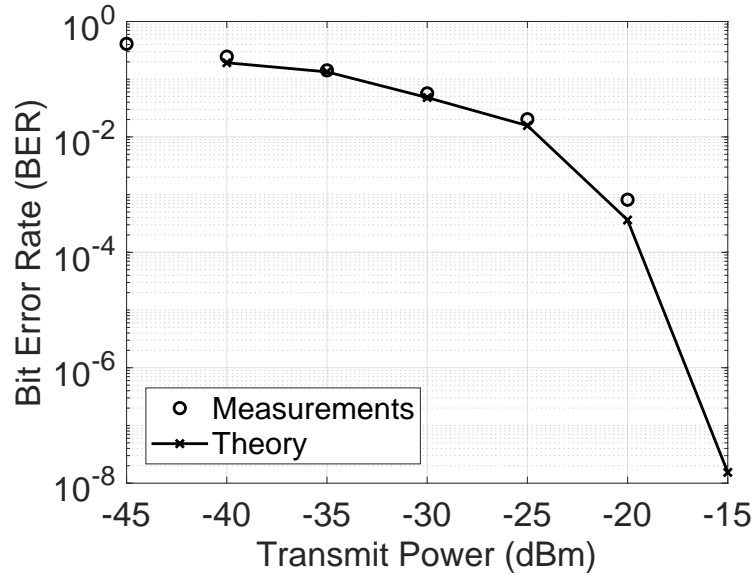
Figure 5.12: Experimental bit error rate (BER) versus the transmitted power at the generator. The bit rate was 345 bps and the distances transmitter-to-tag, tag-to-reader were 1.5 m.

the fixed packet continuously. At the receiver, the bandwidth around the carrier frequency was fixed at 1 MHz. In order to compute the BER, 1200 packets of data were collected for a varying transmit power from -45 to -20 dBm. Each packet contains 28 bits and thus the transmitted bits were 33600. The resulting BER versus the transmit power is shown in Fig. 5.12 and the minimum BER value at -20 dBm was measured to be $8.16 * 10^{-4}$. In the previous chapter we use 2-ASK modulation with FM0 encoding and was showed that BER approached $2.5 * 10^{-3}$ when the transmit power was -30 dBm. As expected, the BER increased as the power at the generator decreases thus the reader can not decode successfully the packets. The 4-PAM high order modulation is less efficient compared to the binary modulation referred in chapter 4. With 4-PAM we need higher SNR to get the same BER that we would get with 2-PAM (2-ASK). In Fig. 5.12 the theoretical BER results are also depicted along with the measurements.

For the theoretical calculations of BER (P_b) the formula of (5.6) is used with the four corresponding Q functions of (5.7). Using a capture of 100 packets we calculated the μ_i value and the σ_i value of each symbol and thus the thresholds. In order to achieve accurate results we used all the symbols of the packet and not only the from the preamble. A different P_b was calculated for each packet and an average value of probabilities was taken at the end. This was performed in order
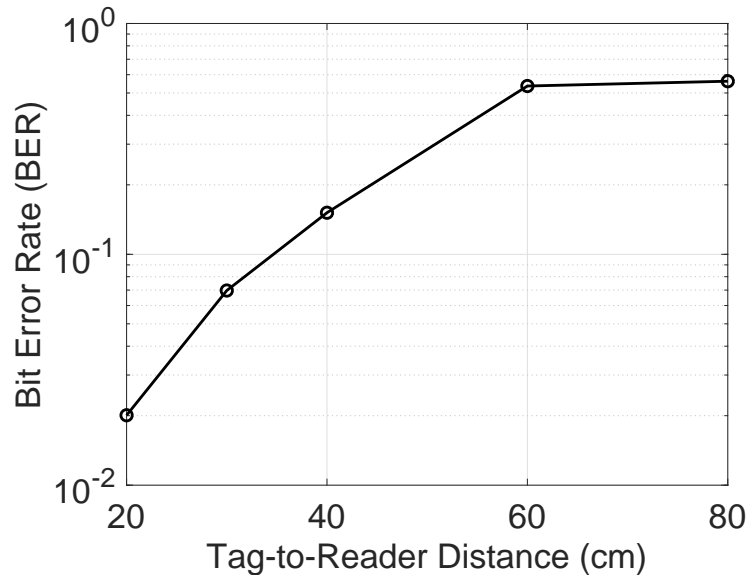
Figure 5.13: Measured bit error rate (BER) versus the tag-to-reader distance. A FM station 34 Km away was used and the communication bit rate was 345 bps.

to account for the variable thresholds across different packets. A good agreement between simulation and measurement results can be observed. Theoretical results were performed for transmitted power up to -15 dBm where the BER approached 10^{-8}. For 10^{-8} BER we need $3 * 10^{+8}$ bits for a confidence level of 0.95 [105] and in the measurements we used only 33600 transmitted bits.

The tag was also tested indoors using the most powerful FM station that was measured in the building. It corresponds to the BBC 95.8 MHz station which is located around 34.65 Km away from experimental setup. The radiated power of the FM station was 250 KW and the power of the received FM signal next to the tag antenna, was measured with a spectrum analyser at around -40 dBm. The BER was measured for different tag-to-reader distances. and the BER results are shown in Fig. 5.13 for a fixed bit rate of 345 bps.

The 4-PAM high order modulation is less efficient compared to the binary modulation referred. There is a clear trade-off between performance and spectral efficiency. Given a baseband channel with bandwidth B and a PAM constellation, by increasing the order of modulation ($m = 2$) we can increase the spectral efficiency $R_b/B = 2m$ bps/Hz and we can transmit with a higher bit rate R_b. The performance of modulation is decreased thus given a fixed BER value, the SNR that is necessary to achieve must be increased with m.

Table 5.2: Tag Power Characteristics

Operation Mode	μW	Bit rate (kbps)
Sleep: (no DAC, no ADC)	1.08	0
Active: 2-ASK (no DAC, no ADC)	6.48	0.147
Active: 2-ASK (no DAC, ADC)	396	0.147
Active: 4-PAM (DAC, no ADC)	27	0.345
Active: 4-PAM (DAC, ADC)	432	0.345
Active: 4-PAM (DAC, no ADC)	283	10.2
Active: 4-PAM (DAC, ADC)	501	10.2

A link budget was also calculated to estimate the received power of our signal [42]. The FM backscatter system is similar to a bistatic radar setup where the FM station source and FM receiver are physically separated. Referring to the geometry of Fig. 5.11 and assuming free space propagation between the emitter and the tag we can calculate the differential received power at the SDR as [106]:

$$P_{\text{SDR}} = \frac{\text{EIRP}\Delta\sigma G_{\text{SDR}}\lambda^2}{(4\pi)^3 D_{\text{tag-SDR}}^2 D_{\text{FM-tag}}^2} \tag{5.15}$$

with G_{SDR}, $D_{\text{tag-SDR}}$, the receiver antenna gain and tag-to-receiver distance respectively. $D_{\text{FM-tag}}$ is the distance from the FM station to the tag, and EIRP is the effective isotropic radiated power of the FM station. The P_{SDR} is proportional to the differential radar cross section (RCS) of the tag [14, 100, 101]:

$$\Delta\sigma = \frac{\lambda^2}{4\pi} G_{\text{tag}}^2 |\Gamma_{\text{i}} - \Gamma_{\text{i+1}}|^2 \tag{5.16}$$

where G_{tag} is the tag antenna gain. For our calculations we assumed, the frequency of 95.8 MHz, $G_{\text{tag}} = G_{\text{SDR}} = 0.5$ dBi, $D_{\text{tag-SDR}} = 0.8$ m and $D_{\text{FM-tag}} = 34.65$ km. Using the four reflection coefficients of Table 5.1, we estimated the three received power magnitudes as: -40.9, -40.4 and -41.2 dBm. For backscatter using more than two reflection states, we can modify the expressions to identify the worst case differential RCS between any two reflection states, since this worst case received power will determine the BER [107, 108]:

$$\Delta\sigma = \frac{\lambda^2}{4\pi} G_{\text{tag}}^2 \min_{i,j \text{ for } i\neq j} |\Gamma_{\text{i}} - \Gamma_{\text{j}}|^2. \tag{5.17}$$

Table 5.3: High Order Modulation Backscatter Designs

Work	Modulation	Backscatter Signal	Power	Part	Bit rate	Energy/bit	Range (m)
This work	4-PAM	Ambient FM	27 μW (Meas)	Tag+Modulator	345 bps	78.2 nJ/bit	1
This work	4-PAM	Ambient FM	501 μW (Meas)	Tag+Modulator	10.2 Kbps	27.7 nJ/bit	-
[14]	4-QAM	UHF CW	115 nW+6mW (Meas)	Tag+Modulator	400 kbps	15 nJ/bit	2.92
[16]	16-QAM	UHF CW	1.49 mW (Meas)	Modulator	96 Mbps	15.5 pJ/bit	1.24
[17]	16-QAM	UHF CW	1 mW (Meas)	Modulator	60 Mbps	6.7 pJ/bit	-
[18]	32-QAM	5.8 GHz CW	113 μW (Sim)	Tag+Modulator	2.5 Mbps	49.1 pJ/bit	-
[94]	4-PSK	UHF TV	-	Tag+Modulator	20 kbps	-	0.7
[95]	4-QAM	Cellular & Wi-Fi	27 nW (Sim)	Modulator	500 kbps	0.054 pJ/bit	-
[73]	4-FSK	Ambient FM	11.07 μW (Sim)	Tag+Modulator	3.2 kbps	3.46 nJ/bit	4.8

For power consumption comparison and validation purposes, 2-ASK binary modulation with FM0 encoding (chapter 4) was designed on this proof-of-concept tag. The proposed MCU was used without the DAC thus binary modulation requires only a digital output pin in order to control the transistor. For the 2-ASK and using the clock of 32 kHz, the minimum T_{symbol} achieved was 3.4 ms and it corresponds to a bit rate of 147 bps. Table 5.2 presents the average power consumption results for 2-ASK and 4-PAM in addition to corresponding bit rates. In binary modulation the average power dissipation was measured at 6.48 μW when the ADC was off and 396 μW when the ADC was activated. The ADC is used for sensing and it is turned off exactly after the data collection in order to reduce the average power consumption. Using the high order modulation, the 4-PAM was measured at 27 μW with the ADC disabled and 432 μW with ADC turned on. The proposed tag was programmed in a higher bit rate of 10.2 Kbps only for power measurements purpose and the power consumption was measured at 501 μW when the ADC was turned on and 501 μW when the ADC was off. An increment of power consumption of the tag plus the modulator (RF transistor) is observed for 4-PAM when is programmed at a higher bit rate. There is also a trade-off between the bit rate and the power consumption across the two modulation schemes. The bit rate is almost duplicated but the consumption is not, due to the non-linear behaviour of the DAC component.

5.7 Discussion

The DC power consumption reported in this work compared with all the similar referenced works so far, are summarized in Table 5.3. The table presents all the designs that include hardware implementation and use only high order modulation over a CW/ambient signal in order to communicate. Our tag has been measured at low bit

rate using ambient FM signals for communication and ensure fair comparison with the other works. As shown, this works represents the lowest power consumption ambient backscatter hardware prototype implementation with high order modulation, reported to date. The energy per bit was calculated at 78 nJ/bit for 345 bps and 27.7 nJ/bit for 10.2 kbps including the energy consumption of the modulator (RF transistor). In [14] the static DC power consumption of the modulator, excluding the power consumption of the microcontroller, was 115 nW corresponding to a data rate of 400 kbps. The tag was fixed at 2.92 m away from the transmitter antenna with EIRP +38.4 dBm. In their prototype tag, a MSP430 microcontroller was consuming an additional $3 - 6$ mW when generating the data. A CR2032 3 V lithium coin cell battery was used as a power source for the device. In [16] the semi-passive device was using a CR2032 3 V coin cell battery for DC power and it was capable of transmitting 96 Mbps with the modulator consuming 1.49 mW (15.5 pJ/bit). Using a transmitter with +23 dBm EIRP the backscatter data link had a measured operating distance of 1.24 m in a typical indoor environment. The [14, 16] were utilizing 4-QAM and 16-QAM respectively on an UHF CW signal. In [17] the value of energy spent in the 16-QAM modulator was 16.7 pJ/bit for a data rate of 60 Mbps and the average power consumption was estimated at 1 mW. [18] presents a 113 μW 32-QAM transmitter employing the backscattering technique for the transmitting part. In [94] a 4-PSK hardware prototype link was implemented using ambient signals. Two tags can communicate with information rate of 20 kbps over a distance of 0.7 m. An RF source was setup to transmit the single tone at 539 MHz with power 10 dBm. In [95], a system capable of modulating the ambient signals was designed for two different ambient sources (cellular and Wi-Fi signals) with 4-QAM high order modulation. Considering a data rate of 500 kbps, the power consumption of the modulator was 27 nW with 0.054 pJ energy per bit. The designs of [17, 95] were tested using a signal generator to generate the transmitter signals and an arbitrary waveform generator to generate the voltage levels at the gate of each transistor. A coupler was used to measure the reflected signal from the circuit, by a VNA. Finally, in [73], the ambient signals were used for communication and for their tag, they simulated an integrated circuit that backscatters audio signals, and showed that it consumes 11.07 μW at 3.2 kbps bit rate. For testing their 4-

FSK modulator prototype, they used an arbitrary waveform generator. A USRP transmitter was setup to broadcast mono and stereo audio signals with power up to -60 dBm. For transmit power -60 dBm at 1.6 and 3.2 kbps, the BER was low at distances (tag-to-reader) as high as 4.8 m. Further, at 1.6 kbps, the BERs were still low up to 0.9 m and 1.82 m at -60 and -50 dBm respectively.

An alternative solution for our RF front-end is the use of four lumped impedances instead of one transistor. For example, the modulator in [14, 94] includes a 4-to-1 Mux (a SP4T CMOS RF switch) to modulate the circuit impedance between 4 impedance states. It can be thought of as an "impedance DAC" that converts a 2-bit digital input to a specified modulating impedance. The multi-state RF switch based modulator is power efficient as the DAC solution, though it trades off the board area and the more complex implementation. In case of an IC implementation it is required bigger die area because 4 switched impedances are required to implement 4-ary modulation. The solution of a simple impedance transistor and a DAC seems to be a promising solution with similar power consumption but reduced die area.

A future challenge for this work is to employ communication measurements (BER) for the 2-PAM using this tag and compare them with the existing high order modulation results. The tag that is proposed in this work is semi-passive since it uses a super capacitor for power supply. With the utilization of the bistatic topology and semi-passive tags that communicate with a low bit rate, it is possible to implement a wireless sensor network, comprising the proposed low-cost sensor/-tags. In that scenario, multiple tags could communicate with only one reader using a TDMA scheme. Each tag could be programmed to work in a duty cycle operation in order to minimize the average power consumption. Each tag will be active only for a desired minimum period of time (i.e. send two packets) and in "sleep" mode for most of the time where the power consumption is only 1.08 μW. The receiver could sent a pure CW signal in order to wake up the nearby tags from the "sleep" mode. The tags could send their information in random intervals in order to avoid a possible signal collision.

5.8   Conclusion

In this work, we designed and integrated an ultra-low-power sensor node/tag with ambient FM backscatter and high order modulation capabilities. The tag can read up to four sensors and modulate the information using 4-PAM modulation instead of the binary 2-PAM. The transmitted bit rate is duplicated and the tag uses the ambient FM signals in order to send the data to a low-cost SDR reader. A real time algorithm was implemented in order to read the reflected signals and communication was demonstrated experimentally indoors. The tag does not require batteries and was supplied with a small solar panel consuming only 27 μW. This high order modulation approach is the first demonstration of backscatter 4-PAM modulation on ambient FM signals. It also paves the way for practical deployments for short range, ultra-low-power backscatter sensors such as wearable body area-sensors.

Chapter 6

Future Steps

This work opens a new direction for backscatter research by showing spread-spectrum-modulation and ambient FM backscatter tags. They can exploit data acquisition from sensors with low power operation and communication ranges up to 10 meters. It seems that the use of ambient FM signals as the only source of both the carrier and "maybe" the tag power is an extremely high energy-efficient communication technique compared to the general RFID technique. At the receiver part, we focus to transmit our useful signals to smartphones using FM backscatter communication. The TV signals are an alternative solution for the ambient source due to their shorter wavelength which means small antennas. Since our application will take advantage on the fact that smartphones have FM receivers, the TV signals do not fulfil our requirements.

Two of the main risks of our work was: 1) If the power dissipation of the electronics is too high, a duty cycle operation will be implemented, and a larger solar panel need be used. 2) If the modulator efficiency is low, the range of communication will be limited. The proposed implementations offer many advantages but also many possibilities for future improvements. Next, a list of future work for a low-cost, long-range ambient backscatter setup is reported:

- **A smartphone as a receiver.**

  Broadcast FM radio infrastructure already exists in cities around the world and devices such as smartphones and cars have the receiver hardware to decode our target ambient signals. Using a commercial cheap smartphone as a receiver, the cost of the communication setup is decreased dramatically instead

97

of using a heavy, costly SDR receiver connected with a computer. The majority of smartphones have inside a FM receiver and they could be operate as SDRs enabling a low cost communication. Using the embedded FM tuner, an Android application and signal processing we could be able to read the useful information of the tag. Finally, many phones use wired headphones as FM radio antennas. Although many smartphone manufacturers recently removed the standard 3.5 mm headphone connector from their latest models, they offer adapters to connect wired headphones. A user standing close to the tag and wearing the pair of headphones connected to the smartphone, could receive the backscattered signals and thus the useful information.

- **Reduce the tag power consumption.**

  The power consumption of the tag can be reduced by the following modifications. First, it is possible to use a more energy efficient MCUs such as PIC16LF1459 (25 μA/MHz at 1.8 V) [46] or small FPGAs (Microsemi IGLOO nano) for the spread spectrum modulation tag [62]. Similarly, one can select sensing elements with minimum power dissipation or even employ some passive sensing technique such as for example [109, 110]. Second, the RF front-end can be modified to use instead of an off-the-shelf switch, a single transistor based switch such as the ones in [17, 111] with pJ/bit energy consumption. Finally, a customized CMOS based IC may provide an even further reduction of dissipated power, as suggested in [73].

- **More energy harvesting techniques.**

  In addition to reducing the circuit consumption, battery-less operation can be achieved by exploring energy harvesting techniques. There are several studies related to the availability of ambient RF energy [112–115] as well as demonstrations of sensors powered by harvesting ambient RF energy from TV [84], Wi-Fi [116] or even microwave oven signals [117], which could be used for smart house-targeted sensors. In addition, multiple technology of energy harvesters such as solar and electromagnetic energy harvesters can be employed in order to combine the different forms of ambient energy availability [53, 118].

- **Extend the tag-to-reader range.**

  Utilizing the bistatic topology and semi-passive tags that communicate with a

low bitrate, it is possible to implement long range backscatter communication. In order to further improve the tag-to-reader communication range a new compact RF front-end could be designed and optimized together with a coil FM antenna on the same substrate. Finally, the combination of a chirp spread spectrum modulation scheme (chapter 3) with ambient FM signals is a well promising approach for range extension. As chirp spread spectrum uses its entire allocated bandwidth to broadcast a signal, it makes it robust to channel noise. Further, because the chirps utilize a broad band of the spectrum, chirp spread spectrum is also resistant to multi-path fading even when operating at very low power.

Appendix A

Appendix

A.1 Morse Code Receiver

```matlab
%%%%%%%%%%%%%%%%%%%%%%%%%%%%%%%%%%%%%%%%%%%%%%%%%%%
%Spiros Daskalakis
%20-11-2016
%Daskalakispiros@gmail.com
%wwww.daskalakispiros.com
%Morse signal translation
%Single: only for one sensor (not WSN)
%Data is captured from RTL SDR througth GNURADIO
%compatible with windows-linux
%%%%%%%%%%%%%%%%%%%%%%%%%%%%%%%%%%%%%%%%%%%%%%%%%%%
close all;
clear all;
clc;
%%%%%%%%%%%%%%%%%%%%%%%%%%%%%%%%%%%%%
GAIN=-10;
Fs = 250e3;              %Same as gnuradio
Ts = 1/Fs;
Resolution = 1;         % in Hz
N_F = Fs/Resolution;
F_axis = -Fs/2:Fs/N_F:Fs/2-Fs/N_F;
```

```matlab
21  %Subcarrier center Freq
22  SUB_CENTER = [33000]
23  SUB_BW = 0.5e3;
24  fi = fopen('spiros2', 'rb');
25  t_sampling = 1.1;                            % seconds
26  N_samples = round(Fs*t_sampling);
27  t = 0:Ts:t_sampling-Ts;
28  packets = 0;
29  HIST_SIZE = 50;
30  cfo_counter=1;
31  DF_est=0;
32  %%%%%%%%%%%%%%%%%%%%%%%%%%%%%%%%%%%
33  while(1)
34  x = fread(fi, 2*N_samples, 'float32');% get samples (*2 for
        I-Q)
35  x = x(1:2:end) + j*x(2:2:end);        % deinterleaving
36  packets = packets + 1
37  if(~mod(cfo_counter, 3))
38      % fft
39      x_fft = fftshift(fft(x, N_F));
40      % cfo estimate
41      [mval mpos] = max(abs(x_fft).^2);
42      DF_est = F_axis(mpos);
43  end
44  % cfo correction
45  x_corr = x.*exp(-j*2*pi*DF_est*t).';
46  % corrected cfo
47  x_corr_fft = fftshift(fft(x_corr, N_F));
48  % sensor's fft
49  F_power_x1=(10*log10((abs(x_corr_fft).^2)*Ts))+GAIN;
50  cfo_counter = cfo_counter + 1;
51  abstream=abs(x_corr);
```

```matlab
52  z  = signal_proc(Fs, SUB_CENTER,SUB_BW, abstream);
53  MorseDemodulator(z);
54  if(mod(packets,HIST_SIZE) ==0)
55      return;
56  end
57  end

1  function [digit_Morse ] = signal_proc(Fs, SUB_CENTER,SUB_BW,
        abstream)
2  Ts = 1/Fs;
3  % Design and apply the bandpass filter
4  speed=104.3;
5  dit = 1.2 / speed;
6  dit_samples = Fs*dit;
7  over = round(dit/Ts);
8  newover = 10;
9  order    = 2;
10 LEFT = SUB_CENTER - SUB_BW;
11 RIGHT = SUB_CENTER + SUB_BW;
12 %Higher orders will give  better off-frequency rejection at
        the
13 %expense of a longer impulse response and a little more
        computation expense
14 [b,a]     = butter(order ,[LEFT,RIGHT]/(Fs/2), 'bandpass');
15 %gia na prosomeioso thorivo vazo 121.. kai kano active to
        parakato
16 %[b, a] = butterTwoBp(1/Fs, LEFT, RIGHT ) ;
17 %x          = filter(b,a,abstream);
18 x = filtfilt(b,a,abstream);
19 % EnaergyPacket=sum(x.^2)*Ts
20 %x_f = mfilter(x,17,Fs,13180);
21 % half-wave rectify x
22 x2 = abs(x);
```

```matlab
23  % slow-wave filter
24  %flt = dit_samples;
25  %y = filter(ones(1,flt)/flt,1, x2);
26  matcheds=ones(round(dit_samples),1);
27  y=conv(matcheds,x2);
28  %agc1 = comm.AGC;
29  %rxSig = agc1(y)
30  agc = max(y);
31  threshold = agc/3;
32  %downsample
33  y = y(1:over/newover:end);
34  % threshold (digitize) y
35  digit_Morse = (y > threshold);
36  % z is now effectively our morse signal
37  axis_x= (1: length(x))*Ts;
38  %figure3= figure;
39  %axes1 = axes('Parent',figure3,'YGrid','on','XGrid','on','
        FontSize',18);
40      figure(3);
41      subplot(3,1,1);
42      plot(axis_x,x, 'LineWidth',1,'Color',[0 0 0]);
43      grid on;
44      title('BandPass Filter');
45      xlabel('Time (Sec)', 'FontSize',18);
46      ylabel('Amplitude', 'FontSize',18);
47      subplot(3,1,2);
48      plot(y, 'LineWidth',1,'Color',[0 0 0]);
49      grid on;
50      title('Matched Filter');
51      xlabel('Time (Sec)', 'FontSize',18);
52      ylabel('Amplitude', 'FontSize',18);
53      subplot(3,1,3);
```

```matlab
54      plot(digit_Morse, 'LineWidth',1,'Color',[0 0 0]);
55      drawnow
56      title('Digitized Morse Signal');
57      grid on;
58      xlabel('Time (Sec)', 'FontSize',18);
59      ylabel('Amplitude', 'FontSize',18);
60  end
```

```matlab
1   function [ ] = MorseDemodulator_v2(dig_sig)
2   %zero pad z so we always start with an onset
3   %dig_sig = [zeros(10,1); dig_sig];
4   % id tones/spaces    ——————————————————
5   % —> find changes between 0/1 and 1/0
6   b = diff(dig_sig);
7   %figure(2); plot(b, 'o');
8   % 1: change from 1 to 0
9   % 0: no change
10  % -1: change from 0 to 1
11  c = b(b~=0);
12  c2 = find(b~=0);
13  tokens = -c .* diff([0; c2]);
14  %figure(3); plot(tokens);
15  % value == length of token
16  % sign == tone/space
17  % id shorts/longs   ——————————————————
18  % since short/long should be bi-modal dist, a regular
        average should give
19  % us a good cutoff point to distinguish between the two? (
        assuming equal
20  % counts of short and long...)
21  % use mean as simple cutoff point; smarter algorithms can
        get smarter about
22  % this classification if they want to.
```

```matlab
23  % 1: short, 2: long, +: tone, -: space
24  tokens2 = tokens;
25  % cutoff tones, cutoff spaces;
26  cut_t = mean(tokens2(tokens2>0));
27  cut_s = mean(tokens2(tokens2<0));
28  %theshold for spases bettwen words
29  w_spase=min(tokens2(tokens2<0))/2;
30  tokens2(tokens > 0 & tokens < cut_t ) = 1;
31  tokens2(tokens > 0 & tokens > cut_t ) = 2;
32  tokens2(tokens < 0 & tokens > cut_s) = -1;
33  tokens2(tokens < 0 & tokens < cut_s ) = -2;
34  tokens2(tokens < 0 & tokens < w_spase ) = -3;
35  % now tokens 2 is a string of -1s, -2s, 1s, 2s, can trim
        first known space;
36  % put final endstop at end
37  tokens2 = [tokens2(2:end); -2];
38  % can drop little spaces, b/c they don't matter when parsing
        ;
39  tokens2(tokens2 == -1) = [];
40  tokens3 = tokens2;
41  tokens4 = {};
42  start_idx = 1;
43  toparse = find(tokens3(start_idx:end) <= -2);
44  int=1;
45  for j=1:length(toparse)
46      a = toparse(j);
47      temp = tokens3(start_idx:a-1);
48      tokens4{int} = temp;
49      tokens4{int+1}= tokens3(a);
50      % zeropad for easy comparison
51      %tokens4{j} = [tokens4{j}; zeros(length(tokens4{j}), 1)];
52      start_idx = a+1;
```

```matlab
53        int=int+2;
54 end
55 % now tokens4 is de−codeable tokens... proceed to setup
       lookups
56 % letters
57 code{1} = [1 2 ];
58 code{2} = [2 1 1 1];
59 code{3} = [2 1 2 1];
60 code{4} = [2 1 1];
61 code{5} = [1];
62 code{6} = [1 1 2 1];
63 code{7} = [2 2 1];
64 code{8} = [1 1 1 1];
65 code{9} = [1 1];
66 code{10} = [1 2 2 2];
67 code{11} = [2 1 2];
68 code{12} = [1 2 1 1];
69 code{13} = [2 2];
70 code{14} = [2 1];
71 code{15} = [2 2 2];
72 code{16} = [1 2 2 1];
73 code{17} = [1 2 1 2];
74 code{18} = [1 2 1];
75 code{19} = [1 1 1];
76 code{20} = [2];
77 code{21} = [1 1 2];
78 code{22} = [1 1 1 2];
79 code{23} = [1 2 2];
80 code{24} = [2 1 1 2];
81 code{25} = [2 1 2 2];
82 code{26} = [2 2 1 1];
83 % punct
```

```
84   code{27} = [1 2 1 2 1 2];
85   code{28} = [2 2 1 1 2 2];
86   code{29} = [1 1 2 2 1 1];
87   code{30} = [2 1 1 2 1];
88   % numbers
89   code{31} = [1 2 2 2 2];
90   code{32} = [1 1 2 2 2];
91   code{33} = [1 1 1 2 2];
92   code{34} = [1 1 1 1 2];
93   code{35} = [1 1 1 1 1];
94   code{36} = [2 1 1 1 1];
95   code{37} = [2 2 1 1 1];
96   code{38} = [2 2 2 1 1];
97   code{39} = [2 2 2 2 1];
98   code{40} = [2 2 2 2 2];
99   decode{1} = 'A';
100  decode{2} = 'B';
101  decode{3} = 'C';
102  decode{4} = 'D';
103  decode{5} = 'E';
104  decode{6} = 'F';
105  decode{7} = 'G';
106  decode{8} = 'H';
107  decode{9} = 'I';
108  decode{10} = 'J';
109  decode{11} = 'K';
110  decode{12} = 'L';
111  decode{13} = 'M';
112  decode{14} = 'N';
113  decode{15} = 'O';
114  decode{16} = 'P';
115  decode{17} = 'Q';
```

```
116  decode{18} = 'R';
117  decode{19} = 'S';
118  decode{20} = 'T';
119  decode{21} = 'U';
120  decode{22} = 'V';
121  decode{23} = 'W';
122  decode{24} = 'X';
123  decode{25} = 'Y';
124  decode{26} = 'Z';
125  decode{27} = '.';
126  decode{28} = ',';
127  decode{29} = '?';
128  decode{30} = '/';
129  decode{31} = '1';
130  decode{32} = '2';
131  decode{33} = '3';
132  decode{34} = '4';
133  decode{35} = '5';
134  decode{36} = '6';
135  decode{37} = '7';
136  decode{38} = '8';
137  decode{39} = '9';
138  decode{40} = '0';
139  out1 = [];
140  % compare tokens to tables
141  %display('Demorsed message:');
142  for j = 1:length(tokens4)
143  %zero pad temp_tok
144  out1(j) =' ';
145  temp_tok = [tokens4{j}; zeros(6 - length(tokens4{j}), 1)];
146  if isequal(temp_tok,[-3;0;0;0;0;0])
147      fprintf(' ');
```

```matlab
148   else
149   for k = 1:length(code)
150   if ~isequal(temp_tok,[code{k}'; zeros(6 - length(code{k}),
          1)])
151       %display('!! DECODING TOKEN ERROR !!')
152       elseif (temp_tok == [code{k}'; zeros(6 - length(code{k}),
              1)]);
153       out1(j) = char(decode{k});
154       fprintf('%s',decode{k});
155       %display(decode{k});
156   end
157   end
158   end
159   % if didn't find a match
160   if isempty(out1)
161       display('!!NOT DETECTABLE MESSAGE!!')
162   end
163   % elseif out1(j)==-1
164   % out1(j) = '_';
165   % end
166   end
167   fprintf('\n');
168   % semi-prettify
169   % outstring = 32*ones(2*length(out1),1);
170   % outstring(2:2:end) = out1;
171   % outstring = char(outstring');
172   % display(outstring);
173   end
```

A.2   2PAM Backscatter Receiver

```matlab
1   %%%%%%%%%%%%%%%%%%%%%%%%%%%%%%%%%%%%%%%%%%%%%%%%%%%%%%%%%%%%%%%%%
2   %      Spiros Daskalakis                                     %
```

```matlab
3   %         last  Revision  11/7/2017                                    %
4   %%%%%%%%%%%%%%%%%%%%%%%%%%%%%%%%%%%%%%%%%%%%%%%%%%%%%%%%%%%%
5   clc;
6   close  all;
7   clear  all;
8   %%%%%%%%%%%%%%%%%%%%%%%%%%%%%%%%%%%%%%%%%%%%%%%%%%%%%%%%%%
9   %pause(6) %wait  six  sec
10  %% RTL SDR  parameters
11  %%%%%%%%%%%%%%%%%%%%%%%%%%%%%%%%%%%%%%%%%%%%%%%%%%%%%%%%%%%
12  GAIN=−15;
13  F_ADC  =  1e6;    %1  MS/s
14  DEC  =  1;
15  Fs  =  F_ADC/DEC;
16  Ts  =  1/Fs;
17  %% Sympol  parameters
18  %%%%%%%%%%%%%%%%%%%%%%%%%%%%%%%%%%%%%%%%%%%%%%%%%%%%%%%%%%%%
19  Tsymbol  =  2.8e−3;
20  % put  the  Duration  (T)  or  the  smallest  Sympol  of  the
         bitstream
21  % put  0.990e−3 =>  for  500  bps
22  % put  500e−6 =>     for  1  kbps
23  % put  202e−6 =      for  2  kbps  (try  198)
24  Tbit=Tsymbol∗2;                  % Datarate= 1/Tbit => For  500  us
         :  1  kbps
25  over  =  round(Tsymbol/Ts);    % Oversampling  factor
26  newover  =  10;                  % Downsample  factor
27  %%%%%%%%%%%%%%%%%%%%%%%%%%%%%%%%%%%%%%%%%%%%%%%%%%%%%%%%%%%%%
28  %%   Tag  Packet  parameters
29  %%%%%%%%%%%%%%%%%%%%%%%%%%%%%%%%%%%%%%%%%%%%%%%%%%%%%%%%%%%%
30  %Bitstreams  length
31  preamble_length=10;   % NoFM0_prample=[1  0  1  0  1  0  1  1  1  1];
32  id_length=2;             % NoFM0_ID=[0  1];
```

```matlab
33  util_length=1;          % NoFM0_util=[0 1];
34  codeword_length=10;   % NoFM0_DATA=[0 0 1 1 1 1 0 0 0 1 0 1];
35  dummybit=1;               %put a dummy bit at the end of packet
        bitstream for better reception
36  %%%
37  total_packet_length=id_length+preamble_length+util_length+
        codeword_length+dummybit;
38  total_packet_duration=total_packet_length*Tbit;
39  preamble_duration=preamble_length*Tbit;
40  % Preamble in FM0 format with symbols (not bits).
41  preamble_symbols=[1 1 0 1 0 0 1 0 1 1 0 1 0 0 1 1 0 0 1 1];
42  preamble = preamble_symbols;    %try (2*preamble_bits-1)=>
        same result
43  preamble_neg=-1*preamble_symbols;
44  preamble_neg_pos=2*preamble_symbols-1;
45  % bitstreams with Data and packet data contained in the
        packet=>for validation perposes
46  fixeddata=[0 0 1 1 1 1 0 0 0 1 0 1];
47  fixedpacketdata=[0 1 0 0 1 1 1 1 0 0 0 1 1];  % id +
        sensor_id + fixeddata
48  %%%%%%%%%%%%%%%%%%%%%%%%%%%%%%%%%%%%%%%%%%%%%%%%%%%%%%%%%%%%%
49  %% Sigmal Prosesing  Variables
50  % For FFT plots (not used)
51  Resolution = 1;    % in Hz
52  N_F = Fs/Resolution;
53  F_axis = -Fs/2:Fs/N_F:Fs/2-Fs/N_F;
54  %% Capture Window Parameters
55  framelength=3;                                        %Window
        =3*packet_length
56  t_sampling = framelength*total_packet_duration;     %
        Sampling time frame (seconds).
57  N_samples = round(Fs*t_sampling);
```

```matlab
58  %%%%%%%%%%%%%%%%%%%%%%%%%%%%%%%%%%%%%%%%%%%%%%%%%%%%%%%%%%%%%%%%%%
59  %% Import Datasets
60  fi = fopen('myfifo', 'rb');
61  t = 0:Ts:t_sampling-Ts;
62  HIST_SIZE =1200;
63  dataset =[];
64  %%%%%%%%%%%%%%%%%%%%%%%%%%%%%%%%%%%%%%%%%%%%%%%%%%%%%%%%%%%%%%%%%%
65  % Debug Print variables => activate and deactive the plots
66  DEBUG_en1=0;
67  DEBUG_en2=1;
68  DEBUG_en3=0;
69  %%%%%%%%%%%%%%%%%%%%%%%%%%%%%%%%%%%%%%%%%%%%%%%%%%%%%%%
70  %% Decoder General variables
71  correct_packets=0;
72  error_packets=0;
73  cut_packets=0;
74  negative_starts1=0;
75  negative_starts2=0;
76  droped_packets=0;
77  pos=1;
78  FLIPPED=0;
79  packets = 1;
80  counter=0;
81  nopacket_ind=0;
82  nodroped_packets=0;
83  %%%%%%%%%%%%%%%%%%%%%%%%%%%%%%%%%%%%%%%%%%%%%%%%%%%%%%
84  %% Decoder  FM0 vectors
85  bits_FM0_2sd_wayB =[];
86  decision_bits_B =[];
87  BER_sum =[];
88  infomatr =[];
89  errorind =[];
```

```matlab
90   %%%%%%%%%%%%%%%%%%%%%%%%%%%%%%%%%%%%%%%%%%%%%%%%%%%
91   %% Orthogonal  pulces  for  detection
92   %D1
93   D1_ups=zeros(1,newover*2);
94   D1_ups(1:newover)=1;
95   D1_ups(newover+1:newover*2)=-1;
96   %D2
97   D2_ups=zeros(1,newover*2);
98   D2_ups(1:newover)=-1;
99   D2_ups(newover+1:newover*2)=1;
100  %%%%%%%%%%%%%%%%%%%%%%%%%%%%%%%%%%%%%%%%%%%%%%%%%%%%
101  ENERGYTHRESS=0;
102  ENERGYTHRESS1=0;
103  while (1)
104  x = fread(fi, 2*N_samples, 'float32');  % get samples (*2
         for  I-Q)
105  x = x(1:2:end) + j*x(2:2:end);          % deinterleaving
106  counter = counter + 1;
107  % delay  every  two  windows  ||  ===> capture__delay(duration=
         packet_window)__capture__delay__......
108  if ~mod(counter, 2)
109  packets = packets + 1;
110  fprintf('Packet=%d|\n',packets)
111  %% Absolute  operation  removes  the  unknown CFO
112  abstream=abs(x).^2;
113  %% Matched  filtering
114  matcheds=ones(round(Tsymbol/Ts),1); % the  pulse  of  matched
         filter  has  duration  Tsymbol
115  dataconv=conv(abstream,matcheds);   %  aply  the  filter  with
         convolution
116  %% Downsample  same  prosedure
117  total_env_ds = dataconv(1:over/newover:end); %% by  factor  of
```

```matlab
        10 to reduce the computational complexity
118 %% Time sync of downsample
119 total_envelope = total_env_ds(newover+1:end-newover+1); %
        total_env_ds(newover+1:end-newover+1);
120 %% remove the DC offset
121 total_envelope=total_envelope-mean(total_env_ds);
122 %% Reject windows if the energy is not much
123 % Calculate the energy in the packet. If the energy is less
        than a threshold, discard packet.
124 energy= sum(total_envelope.^2);
125 maxpoint= max(abs(total_envelope));
126 %% Flip the packet  if its nessesarry
127 %%  Position estimation of packet with  packet's energy
        synchronization
128 for k=1:1: length(total_envelope)-(total_packet_length*2*
        newover)+1
129     energy_synq(k)=sum(abs(total_envelope(k : k+
            total_packet_length*2*newover-1)).^2);
130 end
131 % find the starting point of packet
132     [energy_sinq_max  energy_sinq_ind]=max(energy_synq);
133 %% Print Plots
134 if DEBUG_en1==1;
135     time_axis= 0:Ts:Ts*length(abstream)-Ts;          %same as
            xaxis_m= (1: length(abstream))*Ts Captured signal
            time axis.
136    % fft
137    x_fft = fftshift(fft(x, N_F));
138    F_sensor_est_power=10*log10((abs(x_fft).^2)*Ts/50*1e3)
            -15;
139    figure(1);
140    subplot(2, 1, 1);
```

114

```matlab
141        plot ( time_axis , abstream ) ;
142        title ( 'Time  Domain ' )
143        xlabel ( 'Time  ( Sec ) ' ) ;
144        subplot ( 2 ,  1 ,  2 ) ;
145        plot ( F_axis /1000000,  F_sensor_est_power ) ;
146        title ( 'Frequency  Domain ' )
147        xlabel ( 'Frequency  ( MHz) ' ) ;
148        drawnow ;
149  end
150  if  DEBUG_en2==1;
151        figure ( 3 ) ;
152        time_axis=  0 : Ts : Ts∗length ( abstream )−Ts ;
153        time_comv=0: Ts : Ts∗length ( dataconv )−Ts ;
154        subplot ( 2 ,  1 ,  1 ) ;
155        plot ( dataconv ) ;
156        title ( 'Matched−filtered '  , 'FontSize ' ,14  )
157        xlabel ( 'Time  ( Sec ) ' ,  'FontSize ' ,12 ,  'FontWeight ' , 'bold ' )
             ;
158        ylabel ( 'Amplitude ' ,  'FontSize ' ,12 ,  'FontWeight ' , 'bold ' ) ;
159        grid  on ;
160        subplot ( 2 ,  1 ,  2 ) ;
161        plot ( total_envelope ) ;
162        title ( 'FLIPPED DOWNSAMPLED' )
163        drawnow ;
164   end
165  if  DEBUG_en3==1;
166        figure ( 5 ) ;
167        plot ( total_envelope ) ;
168        xlabel ( 'Time  ( Sec ) ' ,  'FontSize ' ,12 ,  'FontWeight ' , 'bold ' )
             ;
169        ylabel ( 'Amplitude ' ,  'FontSize ' ,12 ,  'FontWeight ' , 'bold ' ) ;
170        grid  on ;
```

115

```matlab
171        drawnow;
172    end
173    %% dc zero offser
174    %% Assume symbol synchronization, which can be implemented
           using correlation with a sequence of known bits in the
           preamble
175    % comparison of the detected preamble bits with the a priori
            known bit sequence
176    %convert the header to a time series for the specific
           sampling frequency and bit duration.
177    %% create the preamble neover format
178    preample_neover=upsample(preamble, newover);
179    preample_neg_neover=upsample(preamble_neg, newover);
180    %% Sync via ENERGY
181    for k=1:1: length(total_envelope)- (total_packet_length*2*
           newover)+1
182        energy_synq(k)=sum(abs(total_envelope(k : k+
               total_packet_length*2*newover-1)).^2);
183    end
184    [energy_sinq_max   energy_sinq_ind]=max(energy_synq);
185    sumxor=0;
186    pointer1=energy_sinq_ind-total_packet_length*2*newover;
187    %if pointer1<=0     || energy <= ENERGYTHRESS/3
188    %negative_starts2=negative_starts2+1;
189    %disp 'Negative start_2';
190    %continue;
191    %end
192    %% Sync via preamble correlation
193    corrsync_out = xcorr(preample_neover, total_envelope);
194    corrsync_out_neg = xcorr(preample_neg_neover, total_envelope
           );
195    [m ind] = max(corrsync_out);
```

```matlab
196  [m_neg ind_neg] = max(corrsync_out_neg);
197  %notice that correlation produces a 1x(2L-1) vector, so
         index must be shifted.
198  %the following operation points to the "start" of the packet
         .
199  if (m < m_neg)
200      start = length(total_envelope)-ind_neg;
201  else
202      start = length(total_envelope)-ind;
203  end
204  if(start <= 0)
205       negative_starts1 = negative_starts1 + 1;
206       disp 'Negative start_1';
207       continue;
208  %% Check if the detected packet is cut in the middle.
209  elseif start+((total_packet_length)*2)*newover > length(
         total_envelope)
210       cut_packets = cut_packets + 1;
211       disp 'Packet cut in the middle!';
212       continue;
213  end
214  shifted_sync_signal_B=total_envelope(start+length(
         preample_neover)-newover-1: start+total_packet_length*2*
         newover);
215  for xi=1:newover*2: length(shifted_sync_signal_B)-newover*2
216       sample2=shifted_sync_signal_B(xi: xi+newover*2-1);
217       sumD1_ups=sum(D1_ups.*sample2');
218       sumD2_ups=sum(D2_ups.*sample2');
219       if (sumD1_ups > sumD2_ups)
220        bits_FM0_2sd_wayB=[bits_FM0_2sd_wayB, 1];
221       else
222        bits_FM0_2sd_wayB=[bits_FM0_2sd_wayB, 0];
```

```matlab
223        end
224  end
225  jim=1;
226  for indx =2:1:length(bits_FM0_2sd_wayB)
227      if bits_FM0_2sd_wayB(indx) == bits_FM0_2sd_wayB(indx−1)
228          decision_bits_B(jim)=0;
229      else
230          decision_bits_B(jim)=1;
231      end
232    jim=jim+1;
233  end
234  id_est_B = decision_bits_B(1: id_length);
235  sensor_id_est_B = decision_bits_B(id_length + 1: id_length +
          util_length);
236  data_bits_es_B = decision_bits_B(id_length+util_length + 1:
          end);
237  if  isequal(decision_bits_B , fixedpacketdata)
238       disp 'Packet Correct !!!!!!!!!!!!!!!!!!!!!!!!!';
239      ENERGYTHRESS=energy;
240      ENERGYTHRESS1=maxpoint;
241       correct_packets=correct_packets+1;
242  else
243       disp 'Packet WRONGGGG
                 ——————————————————————————————————';
244       errorind =[ errorind , packets ];
245       error_packets=error_packets+1;
246      BER_sum(error_packets) = sum(xor(decision_bits_B ,
              fixedpacketdata));
247  end
248       bits_FM0_2sd_wayB =[];
249       decision_bits_B =[];
250  end
```

```
251  if (mod( packets ,HIST_SIZE ) ==0)
252     infomatr (1)=correct_packets ;
253     infomatr (2)=error_packets ;
254     infomatr (3)=negative_starts1+negative_starts2 ;
255     infomatr (4)=cut_packets ;
256     infomatr (5)=error_packets /(correct_packets+error_packets)
            ;
257     infomatr (6)= sum(BER_sum) ;
258     infomatr (7)= sum(BER_sum)/((correct_packets+error_packets)
            *length(fixedpacketdata ));
259     fprintf('Corecct Packets=%d|Packet Error=%d\n',
            correct_packets , error_packets)
260     fprintf('Negative Starts=%d|Cut Packets=%d\n',
            negative_starts1 , cut_packets)
261     fprintf('Negative Starts2=%d\n', negative_starts2)
262     %PER is the number of incorrectly received data packets
            divided by the total number of received packets.
263     fprintf('Packet Error Rate=%d\n', error_packets / (
            correct_packets+error_packets))
264     %fprintf('Bit error rate mean(BER)=%d\n', mean(BER_int))
265     fprintf('Bit error rate (BER)=%d\n', sum(BER_sum)/((
            correct_packets+error_packets)*length(fixedpacketdata))
            )
266  return ;
267  end
268  end
```

A.3   4PAM Backscatter Receiver

```
1  %%%%%%%%%%%%%%%%%%%%%%%%%%%%%%%%%%%%%%%%%%%%%%%%%%%%%%%%%%%%%%%%%
2  %      Spiros  Daskalakis                                      %
3  %      last  Revision  27/4/2018                               %
4  %%%%%%%%%%%%%%%%%%%%%%%%%%%%%%%%%%%%%%%%%%%%%%%%%%%%%%%%%%%%%%%%%
```

```matlab
5   clc;
6   close all;
7   clear all;
8   %%%%%%%%%%%%%%%%%%%%%%%%%%%%%%%%%%%%%%%%%%%%%%%%%%%%%%%
9   %pause(6) %wait six sec
10  %% RTL SDR parameters
11  %%%%%%%%%%%%%%%%%%%%%%%%%%%%%%%%%%%%%%%%%%%%%%%%%%%%%%%%
12  GAIN=−15;
13  F_ADC = 1e6;   %1 MS/s
14  DEC = 1;
15  Fs = F_ADC/DEC;
16  Ts = 1/Fs;
17  %% Sympol parameters
18  %%%%%%%%%%%%%%%%%%%%%%%%%%%%%%%%%%%%%%%%%%%%%%%%%%%%%%%%
19  Tsymbol = 5.85e−3 ;
20  %Tsymbol = 200e−6 ;
21  Tbit=Tsymbol/2;                 % Datarate= 1/Tbit => For 500 us
        : 1 kbps
22  over = round(Tsymbol/Ts);    % Oversampling factor
23  newover = 585;                  % Downsample factor
24  %%%%%%%%%%%%%%%%%%%%%%%%%%%%%%%%%%%%%%%%%%%%%%%%%%%%%%%%
25  %%  Tag Packet parameters
26  %%%%%%%%%%%%%%%%%%%%%%%%%%%%%%%%%%%%%%%%%%%%%%%%%%%%%%%%
27  %Bitstreams length
28  preamble_length=10;               % NoFM0_prample=[1 0 1 0
        1 0 1 1 1 1];
29  id_length=2;                     % NoFM0_ID=[0  1];
30  util_length=2;                   % NoFM0_util=[0  1];
31  codeword_length=14;              % NoFM0_DATA=[0 0 1 1 1 1
        0 0 0 1 0 1];
32  dummybit=0;          %put a dummy bit at the end of packet
        bitstream for better reception
```

```matlab
33  %%%
34  total_packet_length=(id_length+preamble_length+util_length+
        codeword_length+dummybit)/2;
35  total_packet_duration=total_packet_length*Tsymbol;
36  preamble_duration=preamble_length*Tbit;
37  % Preamble in FM0 format with symbols (not bits).
38  preamble=[+3,-3,+3,-3, +3];
39  preamble_neg=-1*preamble;
40  %%%%%%%%%%%%%%%%%%%%%%%%%%%%%%%%%%%%%%%%%%%%%%%%%
41  % bitstreams with Data and packet data contained in the
        packet=>for validation perposes
42  fixedpacketdata=[0 1  1 1  0 0  0 1  0 1  1 1  1 0  0 0  1
        1];  % id + sensor_id + fixedata
43  ipHat = zeros(1,length(fixedpacketdata)/2);
44  %%%%%%%%%%%%%%%%%%%%%%%%%%%%%%%%%%%%%%%%%%%%%%%%%
45  %% Sigmal Prosesing  Variables
46  % For FFT plots (not used)
47  Resolution = 1;   % in Hz
48  N_F = Fs/Resolution;
49  F_axis = -Fs/2:Fs/N_F:Fs/2-Fs/N_F;
50  %% Capture Window Parameters
51  framelength=3;                                    %Window
        =3*packet_length
52  t_sampling = framelength*total_packet_duration;      %
        Sampling time frame (seconds).
53  N_samples = round(Fs*t_sampling);
54  %%%%%%%%%%%%%%%%%%%%%%%%%%%%%%%%%%%%%%%%%
55  %% Import Datasets
56  fi = fopen('PAMAmbient', 'rb');
57  t = 0:Ts:t_sampling-Ts;
58  %%%%%%%%%%%%%%%%%%%%%%%%%%%%%%%%%%%%%%%%%%%%%%%%%%%%%%%%%%%%
59  % Debug Print variables => activate and deactive the plots
```

```matlab
60  DEBUG_en1=0;
61  DEBUG_en2=1;
62  DEBUG_en3=1;
63  %%%%%%%%%%%%%%%%%%%%%%%%%%%%%%%%%%%%%%%%%%%%%%%%%%%%%%
64  %% Decoder General variables
65  correct_packets=0;
66  error_packets=0;
67  cut_packets=0;
68  negative_starts1=0;
69  negative_starts2=0;
70  droped_packets=0;
71  pos=1;
72  FLIPPED=0;
73  packets = 1;
74  counter=0;
75  nopacket_ind=0;
76  nodroped_packets=0;
77  %%%%%%%%%%%%%%%%%%%%%%%%%%%%%%%%%%%%%%%%%%%%%%%%%%%%%%
78  %% Decoder  FM0 vectors
79  bits_FM0_2sd_wayB=[];
80  decision_bits_B=zeros(1,length(fixedpacketdata));
81  BER_sum=[];
82  infomatr=[];
83  errorind=[];
84  dataset= [];
85  HIST_SIZE  =500;
86  while (1)
87  x = fread(fi, 2*N_samples, 'float32');  % get samples (*2
        for I-Q)
88  x = x(1:2:end) + j*x(2:2:end);          % deinterleaving
89  counter = counter + 1;
90  % delay every two windows  ||  ==> capture__delay(duration=
```

```matlab
        packet_window)__capture__delay__......
 91  if ~mod(counter, 2)
 92      packets = packets + 1;
 93      fprintf('Packet=%d|\n',packets)
 94      %% Absolute operation removes the unknown CFO
 95      abstream=abs(x).^2;
 96      %% Matched filtering
 97      matcheds=ones(round(Tsymbol/Ts),1); % the pulse of
            matched filter has duration Tsymbol
 98      dataconv=conv(abstream,matcheds);   % aply the filter
            with convolution
 99      dataconv=dataconv/length(matcheds);
100      %% Downsample same prosedure
101      total_env_ds = dataconv(1:ceil(over/newover):end); %% by
            factor of 10 to reduce the computational complexity
102      %% Time sync of downsample
103      total_envelopea = total_env_ds(newover+1:end-newover+1);
            % total_env_ds(newover+1:end-newover+1);
104      %% remove the DC offset
105       total_envelope=total_envelopea-mean(total_envelopea);
106      %% Sync via ENERGY
107  for k=1:1: length(total_envelope)- (total_packet_length*
     newover)+1
108          energy_synq(k)=sum(abs(total_envelope(k : k+
                total_packet_length*newover-1-newover)).^2);
109  end
110  [energy_sinq_max   energy_sinq_ind]=max(energy_synq);
111  pointer1=energy_sinq_ind-total_packet_length*newover
112  if pointer1<=0
113      negative_starts2=negative_starts2+1;
114      disp 'Negative start_2';
115      continue;
```

```matlab
116    end
117    if DEBUG_en1==1;
118        time_axis= 0:Ts:Ts*length(abstream)-Ts;          %same as
               xaxis_m= (1: length(abstream))*Ts Captured signal time
               axis.
119        % fft
120        x_fft = fftshift(fft(x, N_F));
121        F_sensor_est_power=10*log10((abs(x_fft).^2)*Ts/50*1e3)
               -15;
122        figure(1);
123        %subplot(2, 1, 1);
124        plot(time_axis,abstream);
125        title('Absolute-squared', 'FontSize',14 )
126        xlabel('Time (Sec)', 'FontSize',12, 'FontWeight','bold');
127        ylabel('Amplitude', 'FontSize',12, 'FontWeight','bold');
128        grid on;
129        drawnow;
130    end
131    %% dc zero offser
132    %% Assume symbol synchronization, which can be implemented
           using correlation with a sequence of known bits in the
           preamble
133    % comparison of the detected preamble bits with the a priori
            known bit sequence
134    %convert the header to a time series for the specific
           sampling frequency and bit duration.
135    %% create the preamble neover format
136    preample_neover=upsample(preamble, newover);
137    preample_neg_neover=upsample(preamble_neg, newover);
138    %% Sync via preamble correlation
139    corrsync_out = xcorr(preample_neover, total_envelope);
140    corrsync_out_neg = xcorr(preample_neg_neover, total_envelope
```

124

```matlab
        );
141 [m ind] = max(corrsync_out);
142 [m_neg ind_neg] = max(corrsync_out_neg);
143 %notice that correlation produces a 1x(2L-1) vector, so
        index must be shifted.
144 %the following operation points to the "start" of the packet
        .
145 if (m < m_neg)
146     start = length(total_envelope)-ind_neg;
147     total_envelope=-total_envelope;
148     total_envelopea=-total_envelopea;
149 else
150 start = length(total_envelope)-ind;
151 end
152 if(start <= 0)
153   negative_starts1 = negative_starts1 + 1;
154     disp 'Negative start';
155     continue;
156 elseif start+((total_packet_length))*newover > length(
        total_envelope)  %% Check if the detected packet is cut
        in the middle.
157     cut_packets = cut_packets + 1;
158     disp 'Packet cut in the middle!';
159     continue;
160 end
161 if DEBUG_en2==1;
162     figure(2);
163     subplot(2, 1, 1);
164     plot(dataconv);
165     title('Matched-filtered' ,'FontSize',14 )
166     xlabel('Time (Sec)', 'FontSize',12, 'FontWeight','bold')
            ;
```

```
167        ylabel('Amplitude', 'FontSize',12, 'FontWeight','bold');
168        grid on;
169        subplot(2, 1, 2);
170        plot(total_envelope);
171        title('DOWNSAMPLED DC Removal')
172        xlabel('Time (Sec)', 'FontSize',12, 'FontWeight','bold')
              ;
173        ylabel('Amplitude', 'FontSize',12, 'FontWeight','bold');
174        drawnow;
175  end
176  as=ceil(newover/10);
177  simashifted=total_envelopea(start:start+total_packet_length*
        newover);
178  Sm3=simashifted(3*newover-as:3*newover+as);
179  V0= var(Sm3);
180  M0=mean(Sm3);
181  Sp3=simashifted(4*newover-as:4*newover+as);
182  V3= var(Sp3);
183  M3=mean(Sp3);
184  Sm1=simashifted(5*newover-as:5*newover+as);
185  V1= var(Sm1);
186  M1=mean(Sm1);
187  Sp1=simashifted(6*newover-as:6*newover+as);
188  V2= var(Sp1);
189  M2=mean(Sp1);
190  SimpleTress01=((sqrt(V1)*M0+sqrt(V0)*M1)/(sqrt(V1)+sqrt(V0))
        )+(sqrt(V1)*(V1-V0)/(2*sqrt(V0)*(M1-M0)));
191  SimpleTress12=((sqrt(V1)*M2+sqrt(V2)*M1)/(sqrt(V1)+sqrt(V2))
        )+(sqrt(V2)*(V2-V1)/(2*sqrt(V1)*(M2-M1)));
192  SimpleTress23=((sqrt(V2)*M3+sqrt(V3)*M2)/(sqrt(V3)+sqrt(V2))
        )+(sqrt(V3)*(V3-V2)/(2*sqrt(V2)*(M3-M2)));
193  shifted_sync_signal_B=total_envelopea(start+length(
```

```matlab
        preample_neover)+1: start+total_packet_length*newover);
194 x=shifted_sync_signal_B(1:newover:end);
195 % quantize the input signal x to the alphabet
196 % using nearest neighbor method
197 % alphabet: -3; -1; 1; 3
198 ipHat(find(x< SimpleTress01)) = -3;
199 ipHat(find(x>= SimpleTress23)) = 3;
200 ipHat(find(x>=SimpleTress01 & x<SimpleTress12)) = -1;
201 ipHat(find(x>=SimpleTress12 & x<SimpleTress23)) = 1;
202 y_bits=ipHat
203 if DEBUG_en3==1;
204     figure(6);
205     clf('reset')
206     y1=1:newover:length(shifted_sync_signal_B);
207     plot(y1,x, '*');
208     hold on
209     plot(shifted_sync_signal_B);
210     plot(SimpleTress01*ones(1,length(shifted_sync_signal_B)),
            '-');
211     plot(SimpleTress12*ones(1,length(shifted_sync_signal_B)),
            '-');
212     plot(SimpleTress23*ones(1,length(shifted_sync_signal_B)),
            '-');
213     title('Start Points' ,'FontSize',14)
214     legend('Start Symbol Point','Packet-Signal', 'Thres01', '
            Thres12', 'Thres23')
215     grid on;
216     drawnow;
217 end
218 bitsind=1;
219 %(-3 || 00)-----(-1 || 01)-------(1 || 11)-----(3 || 10)
220 for i=1:length(y_bits)
```

```
221        if  y_bits(i)==-3
222           decision_bits_B  (bitsind)=0;
223           decision_bits_B  (bitsind+1)=0;
224        elseif  y_bits(i)==-1
225           decision_bits_B  (bitsind)=0;
226           decision_bits_B  (bitsind+1)=1;
227         elseif  y_bits(i)==1
228            decision_bits_B  (bitsind)=1;
229           decision_bits_B  (bitsind+1)=1;
230         elseif  y_bits(i)==3
231           decision_bits_B  (bitsind)=1;
232           decision_bits_B  (bitsind+1)=0;
233    end
234           bitsind=bitsind+2;
235    end
236           final_packet=decision_bits_B;
237    if   isequal(final_packet, fixedpacketdata)
238           disp  'Packet  Correct  !!!!!!!!!!!!!!!!!!!!!!!!';
239           correct_packets=correct_packets+1;
240           if  (correct_packets==2)
241           %return;
242    end
243    else
244           disp  'Packet  WRONGGGG——————————————————';
245           error_packets=error_packets+1;
246           BER_sum(error_packets)  =  sum(xor(decision_bits_B,
                   fixedpacketdata));
247    end
248    end
249    decision_bits_B=[];
250    if(mod(packets,HIST_SIZE)  ==0)
251       infomatr(1)=correct_packets;
```

```matlab
252    infomatr(2)=error_packets;
253    infomatr(3)=negative_starts1+negative_starts2;
254    infomatr(4)=cut_packets;
255    infomatr(5)=error_packets /(correct_packets+error_packets)
          ;
256    infomatr(6)= sum(BER_sum);
257    infomatr(7)= sum(BER_sum)/((correct_packets+error_packets)
          *length(fixedpacketdata));
258    fprintf('Corecct Packets=%d|Packet Error=%d\n',
          correct_packets, error_packets)
259    fprintf('Negative Starts=%d|Cut Packets=%d\n',
          negative_starts1, cut_packets)
260    fprintf('Negative Starts2=%d\n', negative_starts2)
261    %PER is the number of incorrectly received data packets
          divided by the total number of received packets.
262    fprintf('Packet Error Rate=%d\n', error_packets / (
          correct_packets+error_packets))
263    fprintf('Bit error rate (BER)=%d\n', sum(BER_sum)/((
          correct_packets+error_packets)*length(fixedpacketdata))
          )
264    save('4PAM_FM_CW_min10_500_pakets_1MSps_myway','infomatr')
265     return;
266 end
267 end
```

Bibliography

[1] F. FAO *et al.*, *The future of food and agriculture: Trends and challenges.* Food and Agriculture Organisation, Rome, 2017.

[2] T. Ojha, S. Misra, and N. S. Raghuwanshi, "Wireless sensor networks for agriculture: The state-of-the-art in practice and future challenges," *Elsevier, Computers and Electronics in Agriculture*, vol. 118, pp. 66–84, 2015.

[3] W. Liu, K. Huang, X. Zhou, and S. Durrani, "Backscatter Communications for Internet-of-Things: Theory and Applications," *arXiv preprint arXiv:1701.07588*, Jan. 2017.

[4] H. Stockman, "Communication by Means of Reflected Power," *Proc. IEEE IRE*, vol. 36, no. 10, pp. 1196–1204, Oct. 1948.

[5] *Specification for RFID Air Interface Protocol for Communications at 860 MHz-960 MHz, Version 2.0.1*, EPC Global Inc., 2015. [Online]. Available: https://www.gs1.org/sites/default/files/docs/epc/Gen2_Protocol_Standard.pdf

[6] A. P. Sample, D. J. Yeager, P. S. Powledge, A. V. Mamishev, and J. R. Smith, "Design of an RFID-based battery-free programmable sensing platform," *IEEE Trans. Instrum. Meas.*, vol. 57, no. 11, pp. 2608–2615, Jun. 2008.

[7] S. Naderiparizi, A. N. Parks, Z. Kapetanovic, B. Ransford, and J. R. Smith, "Wispcam: A Battery-Free RFID camera," in *Proc. IEEE Int. Conf. on RFID*, Apr. 2015.

[8] J. Kimionis, A. Bletsas, and J. N. Sahalos, "Increased Range Bistatic Scatter Radio," *IEEE Trans. Commun.*, vol. 62, no. 3, pp. 1091–1104, Mar. 2014.

[9] S. N. Daskalakis, S. D. Assimonis, E. Kampianakis, and A. Bletsas, "Soil Moisture Scatter Radio Networking With Low Power," *IEEE Trans. Microw. Theory Techn.*, vol. 64, no. 7, pp. 2338–2346, Jun. 2016.

[10] V. Iyer, V. Talla, B. Kellogg, S. Gollakota, and J. Smith, "Intertechnology backscatter: Towards internet connectivity for implanted devices," in *Proc. ACM Spec. Interest Group Data Commun. Conf. (SIGCOMM)*, Florianopolis, Brazil, Aug. 2016, pp. 356–369.

[11] S. N. Daskalakis, G. Goussetis, S. D. Assimonis, M. M. Tentzeris, and A. Georgiadis, "A uW Backscatter-Morse-Leaf Sensor for Low-Power Agricultural Wireless Sensor Networks," *IEEE Sensors J.*, vol. 18, no. 19, pp. 7889–7898, Oct. 2018.

[12] E. Kampianakis, A. Sharma, J. Arenas, and M. S. Reynold, "A Dual-Band Wireless Power Transfer and Backscatter Communication Approach for Real-Time Neural/EMG Data Acquisition," *IEEE J. of Radio Frequency Identification*, vol. 1, no. 1, pp. 100–107, Aug. 2017.

[13] S. Thomas and M. S. Reynolds, "QAM backscatter for passive UHF RFID tags," in *Proc. IEEE Int. Conf. on RFID*, Orlando, FL, USA, Apr. 2010, pp. 210–214.

[14] S. J. Thomas, E. Wheeler, J. Teizer, and M. S. Reynolds, "Quadrature amplitude modulated backscatter in passive and semipassive UHF RFID systems," *IEEE Trans. Microw. Theory Techn.*, vol. 60, no. 4, pp. 1175–1182, Apr. 2012.

[15] J. Kimionis, A. Georgiadis, and M. M. Tentzeris, "Millimeter-wave backscatter: A quantum leap for gigabit communication, RF sensing, and wearables," in *Proc. IEEE MTT-S Int. Microw. Symp. (IMS)*, Honolulu, HI, USA, Jun. 2017, pp. 812–815.

[16] S. J. Thomas and M. S. Reynolds, "A 96 Mbit/sec, 15.5 pJ/bit 16-QAM modulator for UHF backscatter communication," in *Proc. IEEE Int. Conf. on RFID*, Orlando, FL, USA, Apr. 2012, pp. 185–190.

[17] R. Correia, A. Boaventura, and N. B. Carvalho, "Quadrature Amplitude Backscatter Modulator for Passive Wireless Sensors in IoT Applications," *IEEE Trans. Microw. Theory Techn.*, vol. 65, no. 4, pp. 1103–1110, Feb. 2017.

[18] A. Shirane, H. Tan, Y. Fang, T. Ibe, H. Ito, N. Ishihara, and K. Masu, "A 5.8 GHz RF-powered transceiver with a 113 uW 32-QAM transmitter employing the IF-based quadrature backscattering technique," in *Proc. IEEE Int. Solid-State Circuits Conf. (ISSCC)*, San Francisco, CA, USA, Feb. 2015, pp. 1–3.

[19] C. Boyer and S. Roy, "Backscatter communication and RFID: Coding, Energy, and MIMO Analysis," *IEEE Trans. on Commun.*, vol. 62, no. 3, pp. 770–785, Mar. 2014.

[20] V. Liu, A. Parks, V. Talla, S. Gollakota, D. Wetherall, and J. R. Smith, "Ambient backscatter: wireless communication out of thin air," *ACM SIGCOMM Comput. Commun. Rev.*, vol. 43, no. 4, pp. 39–50, Oct. 2013.

[21] S. Ivanov, K. Bhargava, and W. Donnelly, "Precision farming: Sensor analytics," *IEEE Intelligent Systems J.*, vol. 30, no. 4, pp. 76–80, Jul. 2015.

[22] L. Ruiz-Garcia, L. Lunadei, P. Barreiro, and I. Robla, "A review of wireless sensor technologies and applications in agriculture and food industry: state of the art and current trends," *Molecular Diversity Preservation International Open Access Sensors J.*, vol. 9, no. 6, pp. 4728–4750, Jun. 2009.

[23] C. Yu, Y. Cui, L. Zhang, and S. Yang, "Zigbee wireless sensor network in environmental monitoring applications," in *Proc. IEEE Conf. on Wireless Commun. Networking and Mob. Comput. (WiCOM)*, Binjiang, China, Sept. 2009, pp. 1–5.

[24] N. Fahmi, S. Huda, E. Prayitno, M. U. H. Al Rasyid, M. C. Roziqin, and M. U. Pamenang, "A prototype of monitoring precision agriculture system based on WSN," in *Proc. IEEE Int. Sem. on Intelligent Technology and Its Applications (ISITIA)*, Surabaya, Indonesia, Aug. 2017, pp. 323–328.

[25] S. Oren, H. Ceylan, P. S. Schnable, and L. Dong, "High-Resolution Patterning and Transferring of Graphene-Based Nanomaterials onto Tape toward Roll-to-

Roll Production of Tape-Based Wearable Sensors," *Advanced Materials Technologies*, vol. 2, no. 12, p. 1700223, Dec. 2017.

[26] V. Palazzari, P. Mezzanotte, F. Alimenti, F. Fratini, G. Orecchini, and L. Roselli, "Leaf compatible "eco-friendly" temperature sensor clip for high density monitoring wireless networks," *Cambridge Univ. Press Wireless Power Transfer*, vol. 4, no. 1, pp. 55–60, Feb. 2017.

[27] H.-D. Seelig, R. J. Stoner, and J. C. Linden, "Irrigation control of cowpea plants using the measurement of leaf thickness under greenhouse conditions," *Springer J. Irrigation Science*, vol. 30, no. 4, pp. 247–257, Jul. 2012.

[28] A. Afzal, S. W. Duiker, J. E. Watson, and D. Luthe, "Leaf thickness and electrical capacitance as measures of plant water status," *Trans. of the ASABE*, vol. 60, no. 4, pp. 1063–1074, Jan. 2017.

[29] *SG-1000 Leaf Sensor*, AgriHouse Inc., 2017. [Online]. Available: https://www.biocontrols.com/Leaf%20Sensor/SG-1000softwareV1.pdf

[30] N. Patel, A. Mehta, and A. Shekh, "Canopy temperature and water stress quantificaiton in rainfed pigeonpea (Cajanus cajan (L.) Millsp.)," *Elsevier, Agricultural and Forest Meteorology*, vol. 109, no. 3, pp. 223–232, Sep. 2001.

[31] N. Abraham, P. Hema, E. Saritha, and S. Subramannian, "Irrigation automation based on soil electrical conductivity and leaf temperature," *Elsevier Agricultural Water Management J.*, vol. 45, no. 2, pp. 145–157, Jul. 2000.

[32] R. Pearcy, O. Bjorkman, A. Harrison, and H. Mooney, "Photosynthetic performance of two desert species with C4 photosynthesis in Death Valley, California," *Carnegie Institute Year Book*, vol. 70, pp. 540–550, 1971.

[33] G. Hornero, J. E. Gaitán-Pitre, E. Serrano-Finetti, O. Casas, and R. Pallas-Areny, "A novel low-cost smart leaf wetness sensor," *Elsevier, Computers and Electronics in Agriculture*, vol. 143, pp. 286–292, Dec. 2017.

[34] *PHYTOS 31, Dielectric Leaf Wetness Sensor, product manual*, Decagon Devices, Inc., 2016. [Online]. Available: http://library.metergroup.com/Manuals/10386_Leaf%20Wetness%20Sensor_Web.pdf

[35] S. D. Assimonis, S. N. Daskalakis, and A. Bletsas, "Sensitive and efficient RF harvesting supply for batteryless backscatter sensor networks," *IEEE Trans. Microw. Theory Techn.*, vol. 64, no. 4, pp. 1327–1338, Apr. 2016.

[36] E. Kampianakis, J. Kimionis, K. Tountas, C. Konstantopoulos, E. Koutroulis, and A. Bletsas, "Wireless environmental sensor networking with analog scatter radio and timer principles," *IEEE Sensors J.*, vol. 14, no. 10, pp. 3365–3376, Oct. 2014.

[37] C. Konstantopoulos, E. Koutroulis, N. Mitianoudis, and A. Bletsas, "Converting a Plant to a Battery and Wireless Sensor with Scatter Radio and Ultra-Low Cost," *IEEE Trans. Instrum. Meas.*, vol. 65, no. 2, pp. 388–398, Feb. 2016.

[38] S. F. Pichorim, N. J. Gomes, and J. C. Batchelor, "Two Solutions of Soil Moisture Sensing with RFID for Landslide Monitoring," *Multidisciplinary Digital Publishing Institute Sensors J.*, vol. 18, no. 2, p. 452, Feb. 2018.

[39] V. Palazzi, F. Gelati, U. Vaglioni, F. Alimenti, P. Mezzanotte, and L. Roselli, "Leaf-compatible autonomous RFID-based Wireless Temperature Sensors for Precision Agriculture," in *Proc. IEEE Wireless Sensors and Sensor Networks (WiSNet) Conf.*, Orlando, Florida, USA, Jan. 2019.

[40] S. N. Daskalakis, A. Collado, A. Georgiadis, and M. M. Tentzeris, "Backscatter morse leaf sensor for agricultural wireless sensor networks," in *Proc. IEEE Sensors Conf.*, Glasgow, UK, Oct. 2017, pp. 1–3.

[41] K. Kurokawa, "Power waves and the scattering matrix," *IEEE Trans. Microw. Theory Techn.*, vol. 13, no. 2, pp. 194–202, Mar. 1965.

[42] J. D. Griffin and G. D. Durgin, "Complete link budgets for backscatter-radio and RFID systems," *IEEE Antennas Propag. Mag.*, vol. 51, no. 2, pp. 11–25, Apr. 2009.

[43] C.-C. Yen, A. E. Gutierrez, D. Veeramani, and D. Van Der Weide, "Radar cross-section analysis of backscattering rfid tags," *IEEE Ant. and Wireless Prop. Lett.*, vol. 6, pp. 279–281, Jun. 2007.

[44] J. J. Fahie, *A History of Electric Telegraphy, to the year 1837.* London: E. & FN Spon, 1884.

[45] J. G. Proakis and M. Salehi, *Digital Communications fifth edition, 2007.* McGraw-Hill Companies, Inc., New York, NY, 2008.

[46] *PIC16LF1459, USB Microcontroller with Extreme Low-Power Technology, product manual*, Microchip Technology Inc., 2014. [Online]. Available: http://www.microchip.com/downloads/en/DeviceDoc/40001639B.pdf

[47] *TS3002 1V/1uA Easy-to-Use Silicon Oscillator/Timer, product manual*, Silicon Laboratories, Inc., 2014. [Online]. Available: https://docs-apac. rs-online.com/webdocs/1257/0900766b812571eb.pdf

[48] *XC6504 Ultra Low Power Consumption Voltage Regulator, product manual*, Uorex Semiconductor, 2012. [Online]. Available: https://www.torexsemi. com/file/xc6504/XC6504.pdf

[49] C. Konstantopoulos, "Self-Powered Plant Sensor for Scatter Radio," Master's thesis, School of Electrical and Computer Engineering, Technical University of Crete, Greece, 2015.

[50] *TPL5010Nano-power System Timer with Watchdog Function, product manual*, Instruments, Texas, 2015. [Online]. Available: http://www.ti.com/lit/ds/ symlink/tpl5010.pdf

[51] *LMT84 Analog Temperature Sensor, product manual*, Instruments, Texas, 2017. [Online]. Available: http://www.ti.com/lit/ds/symlink/lmt84.pdf

[52] *ADG919 RF switch, product manual, product manual*, Analog Devices, 2016. [Online]. Available: http://www.analog.com/media/en/ technical-documentation/data-sheets/ADG918_919.pdf

[53] K. Niotaki, A. Collado, A. Georgiadis, S. Kim, and M. M. Tentzeris, "Solar/-Electromagnetic energy harvesting and wireless power transmission," *Proc. IEEE*, vol. 102, no. 11, pp. 1712–1722, Nov. 2014.

[54] *SP3-37 Flexible Solar Panel 3V @ 22mA, product manual*, PowerFilm, 2009. [Online]. Available: https://goo.gl/q5ECXh

[55] *NESDR SMArt Bundle-Premium RTL-SDR, product manual*, NooElec Inc., 2017. [Online]. Available: http://www.nooelec.com/store/nesdr-smart.html

[56] G. Radio, "The gnu software radio," *Available from World Wide Web: https://gnuradio. org*, 2007.

[57] P. Baronti, P. Pillai, V. W. Chook, S. Chessa, A. Gotta, and Y. F. Hu, "Wireless sensor networks: A survey on the state of the art and the 802.15.4 and Zigbee standards," *Elsevier, Computer Communications*, vol. 30, no. 7, pp. 1655–1695, May. 2007.

[58] M. Centenaro, L. Vangelista, A. Zanella, and M. Zorzi, "Long-range communications in unlicensed bands: The rising stars in the IoT and smart city scenarios," *IEEE Wireless Commun.*, vol. 23, no. 5, pp. 60–67, Oct. 2016.

[59] *LoRaWAN 1.0.3 Specification*, LoRa Alliance, Inc., 2018. [Online]. Available: https://lora-alliance.org/sites/default/files/2018-07/lorawan1.0.3.pdf

[60] G. Vougioukas, S.-N. Daskalakis, and A. Bletsas, "Could battery-less scatter radio tags achieve 270-meter range?" in *Proc. IEEE Wireless Power Transfer (WPTC) Conf.*, Aveiro, Portugal, Jun. 2016, pp. 1–3.

[61] V. Talla, M. Hessar, B. Kellogg, A. Najafi, J. R. Smith, and S. Gollakota, "Lora backscatter: Enabling the vision of ubiquitous connectivity," in *Proc. of the ACM on Interactive, Mobile, Wearable and Ubiquitous Technologies*, vol. 1, no. 3, Sep. 2017, p. 105.

[62] Y. Peng, L. Shangguan, Y. Hu, Y. Qian, X. Lin, X. Chen, D. Fang, and K. Jamieson, "Plora: A passive long-range data network from ambient LoRa transmissions," in *Proc. ACM Special Interest Group on Data Communication (SIGCOMM)*, Budapest, Hungary, Aug. 2018, pp. 147–160.

[63] R. Correia, Y. Ding, S. N. Daskalakis, P. Petridis, G. Goussetis, A. Georgiadis, and N. B. Carvalho, "Chirp based backscatter modulation," in *Proc. IEEE*

MTT-S Int. Microw. Symp. (IMS), Boston, Massachusetts, USA, Jun. 2019, pp. 279–282.

[64] A. Varshney, O. Harms, C. Pérez-Penichet, C. Rohner, F. Hermans, and T. Voigt, "Lorea: A backscatter architecture that achieves a long communication range," in *Proc. of the 15th ACM Conference on Embedded Network Sensor Systems*, Delft, Netherlands, Nov. 2017, p. 18.

[65] *LoRa modulation basics, Application Note*, Semtech Corporation, Nov. 2015.

[66] R. Ghanaatian, O. Afisiadis, M. Cotting, and A. Burg, "Lora digital receiver analysis and implementation," in *Proc. IEEE Int. Conf. on Acoustics, Speech and Signal Proc. (ICASSP)*, Brighton, United Kingdom, Apr. 2019, pp. 1498–1502.

[67] M. Knight and B. Seeber, "Decoding LoRa: Realizing a modern LPWAN with SDR," in *Proc. GNU Radio Conf.*, vol. 1, no. 1, Boulder, Colorado, USA, Sep. 2016.

[68] *ATF-54143 Low Noise Enhancement Mode Pseudomorphic HEMT Transistor 36 dBm OIP3, product manual*, Avago Technologies, 2012. [Online]. Available: https://docs.broadcom.com/docs/AV02-0488EN

[69] P. Robyns, P. Quax, W. Lamotte, and W. Thenaers, "A multi-channel software decoder for the LoRa modulation scheme," in *Proc. 3rd International Conference on Internet of Things, Big Data and Security (IoTBDS)*, Madeira, Portugal, Mar. 2018, pp. 41–51.

[70] D. Croce, M. Gucciardo, S. Mangione, G. Santaromita, and I. Tinnirello, "Impact of LoRa imperfect orthogonality: Analysis of link-level performance," *IEEE Commun. Lett.*, vol. 22, no. 4, pp. 796–799, Apr. 2018.

[71] T. Elshabrawy and J. Robert, "Closed-form approximation of LoRa modulation BER performance," *IEEE Commun. Lett.*, vol. 22, no. 9, pp. 1778–1781, Sep. 2018.

[72] B. Reynders and S. Pollin, "Chirp spread spectrum as a modulation technique for long range communication," in *Proc. IEEE Symp. on Comm. and Vehicular Technologies (SCVT)*, Mons, Belgium, Nov. 2016, pp. 1–5.

[73] A. Wang, V. Iyer, V. Talla, J. R. Smith, and S. Gollakota, "FM backscatter: Enabling Connected Cities and Smart Fabrics," in *Proc. USENIX Symp. on Networked Sys. Design and Impl. (NSDI)*, Boston, MA, Mar. 2017, pp. 243–258.

[74] B. Kellogg, A. Parks, S. Gollakota, J. R. Smith, and D. Wetherall, "Wi-Fi backscatter: Internet connectivity for RF-powered devices," in *Proc. ACM Spec. Interest Group Data Commun. Conf. (SIGCOMM)*, Chicago, IL, USA, Aug. 2014, pp. 607–618.

[75] D. Bharadia, K. R. Joshi, M. Kotaru, and S. Katti, "BackFi: High throughput WiFi backscatter," in *Proc. ACM Spec. Interest Group Data Commun. Conf. (SIGCOMM)*, London, UK, Aug. 2015, pp. 283–296.

[76] G. Wang, F. Gao, R. Fan, and C. Tellambura, "Ambient backscatter communication systems: Detection and performance analysis," *IEEE Trans. on Commun.*, vol. 64, no. 11, pp. 4836–4846, Aug. 2016.

[77] D. Darsena, G. Gelli, and F. Verde, "Performance analysis of ambient backscattering for green Internet of Things," in *Proc. IEEE Personal, Indoor, Mob. Radio Commun. (PIMRC) Symp.*, Valencia, Spain, Sep. 2016, pp. 1–6.

[78] J. Qian, F. Gao, G. Wang, S. Jin, and H. Zhu, "Noncoherent detections for ambient backscatter system," *IEEE Trans. Wireless Commun.*, vol. 16, no. 3, pp. 1412–1422, Dec. 2017.

[79] S. N. Daskalakis, J. Kimionis, A. Collado, M. M. Tentzeris, and A. Georgiadis, "Ambient FM Backscattering for Smart Agricultural Monitoring," in *Proc. IEEE MTT-S Int. Microw. Symp. (IMS)*, Honolulu, HI, USA, Jun. 2017, pp. 1339–1341.

[80] D. M. Dobkin, "The RF in RFID Passive UHF in Practice," *United States of America, Newness*, 2008.

[81] L. Der, "Frequency Modulation FM tutorial," *Silicon Laboratories Inc*, 2008.

[82] *MSP430FR5969 LaunchPad Development Kit, product manual*, Texas Instruments, 2015. [Online]. Available: http://www.ti.com/lit/ug/slau535b/slau535b.pdf

[83] *ADG902 RF switch, product manual, product manual*, Analog Devices, 2016. [Online]. Available: https://www.analog.com/media/en/technical-documentation/data-sheets/ADG901_902.pdf

[84] S. Kim, R. Vyas, J. Bito, K. Niotaki, A. Collado, A. Georgiadis, and M. M. Tentzeris, "Ambient RF energy-harvesting technologies for self-sustainable standalone wireless sensor platforms," *Proc. IEEE*, vol. 102, no. 11, pp. 1649–1666, Nov. 2014.

[85] M. Simon and D. Divsalar, "Some interesting observations for certain line codes with application to RFID," *IEEE Trans. on Commun.*, vol. 54, no. 4, pp. 583–586, Apr. 2006.

[86] S. G. Wilson, *Digital modulation and coding.* Prentice-Hall, Inc., 1995.

[87] J. G. Proakis, *Digital Communications fourth edition, 2001.* McGraw-Hill Companies, Inc., New York, NY, 1998.

[88] A. Bletsas, J. Kimionis, A. G. Dimitriou, and G. N. Karystinos, "Single-antenna coherent detection of collided FM0 RFID signals," *IEEE Trans. on Commun.*, vol. 60, no. 3, pp. 756–766, Feb. 2012.

[89] N. Kargas, F. Mavromatis, and A. Bletsas, "Fully-coherent reader with commodity SDR for Gen2 FM0 and computational RFID," *IEEE Wireless Commun. Lett.*, vol. 4, no. 6, pp. 617–620, Sep. 2015.

[90] M. Bamiedakis-Pananos, "Synchronization and Detection for Gen2 RFID Signals," Master's thesis, School of Electrical and Computer Engineering, Technical University of Crete, Greece, 2015.

[91] *Agilent N4901 Serial BER, User's Guide*, Agilent Technologies Inc., 2006.

[92] *Permitted Forms of Low Power Broadcast Operation, Public Notice 14089.*, Federal Communications Commission (FCC). [Online]. Available: https://apps.fcc.gov/edocs_public/attachmatch/DOC-297510A1.pdf

[93] N. Van Huynh, D. T. Hoang, X. Lu, D. Niyato, P. Wang, and D. I. Kim, "Ambient Backscatter Communications: A Contemporary Survey," *IEEE Communications Surveys & Tutorials*, vol. 20, no. 4, pp. 2889–2922, May 2018.

[94] J. Qian, A. N. Parks, J. R. Smith, F. Gao, and S. Jin, "IoT Communications with M-PSK modulated ambient backscatter: Algorithm, analysis, and implementation," *IEEE Internet of Things J.*, vol. 6, no. 1, pp. 844–855, Feb. 2019.

[95] R. Correia and N. B. Carvalho, "Dual-B and High Order Modulation Ambient backscatter," in *Proc. IEEE MTT-S Int. Microw. Symp. (IMS)*, Philadelphia, Pennsylvania, USA, Jun. 2018, pp. 270–273.

[96] S. N. Daskalakis, R. Correia, G. Goussetis, M. M. Tentzeris, N. B. Carvalho, and A. Georgiadis, "Spectrally efficient 4-PAM ambient FM backscattering for wireless sensing and RFID applications," in *Proc. IEEE MTT-S Int. Microw. Symp. (IMS)*, Philadelphia, Pennsylvania, USA, Jun. 2018.

[97] S. D. Assimonis, S. N. Daskalakis, and A. Bletsas, "Efficient RF harvesting for low-power input with low-cost lossy substrate rectenna grid," in *Proc. IEEE Conf. on RFID Techn. and Appl. (RFID-TA)*, Tampere, Finland, Sep. 2014, pp. 1–6.

[98] X. Gu, S. Hemour, L. Guo, and K. Wu, "Integrated Cooperative Ambient Power Harvester Collecting Ubiquitous Radio Frequency and Kinetic Energy," *IEEE Trans. Microw. Theory Techn.*, vol. 66, no. 9, pp. 4178–4190, Sep. 2018.

[99] *ATF-52189 High Linearity Mode Enhancement Pseudomorphic HEMT FET Transistor, product manual*, Broadcom, 2006. [Online]. Available: https://www.broadcom.com/products/wireless/transistors/fet/atf-52189#

[100] A. Bletsas, A. G. Dimitriou, and J. N. Sahalos, "Improving Backscatter Radio Tag Efficiency," *IEEE Trans. Microw. Theory Techn.*, vol. 58, no. 6, pp. 1502–1509, Jun. 2010.

[101] P. V. Nikitin, K. Rao, and R. Martinez, "Differential RCS of RFID tag," *IET Electron. Lett.*, vol. 43, no. 8, pp. 431–432, Apr. 2007.

[102] C. R. Johnson Jr, W. A. Sethares, and A. G. Klein, *Software receiver design: build your own digital communication system in five easy steps.* Cambridge Univ. Press, 2011.

[103] P. N. Alevizos, Y. Fountzoulas, G. N. Karystinos, and A. Bletsas, "Log-linear-complexity GLRT-optimal noncoherent sequence detection for orthogonal and RFID-oriented modulations," *IEEE Trans. on Commun.*, vol. 64, no. 4, pp. 1600–1612, Apr. 2016.

[104] B. Clarke and K. Kreitzer, "Maximizing the dynamic range of software-defined radio," *Analog Devices Technical Article MS-2735*, pp. 1–4, 2014.

[105] S. N. Daskalakis, J. Kimionis, A. Collado, G. Goussetis, M. M. Tentzeris, and A. Georgiadis, "Ambient Backscatterers Using FM Broadcasting for Low Cost and Low Power Wireless Applications," *IEEE Trans. Microw. Theory Techn.*, vol. PP, no. 99, pp. 1–12, Nov. 2017.

[106] J. F. Ensworth and M. S. Reynolds, "Ble-backscatter: ultralow-power IoT nodes compatible with Bluetooth 4.0 low energy (BLE) smartphones and tablets," *IEEE Trans. Microw. Theory Techn.*, vol. 65, no. 9, pp. 3360–3368, Sept. 2017.

[107] J. G. Proakis and M. Salehi, *Fundamentals of communication systems.* 2nd ed. Colchester, Essex: Pearson, 2014.

[108] J. Rosenthal and M. S. Reynolds, "A 1.0-mb/s 198-pj/bit Bluetooth Low-Energy Compatible Single Sideband Backscatter Uplink for the Neurodisc Brain–Computer Interface," *IEEE Trans. Microw. Theory Techn.*, vol. 67, no. 10, pp. 4015–4022, Oct. 2019.

[109] S. Kim, Y. Kawahara, A. Georgiadis, A. Collado, and M. Tentzeris, "Low-cost inkjet-printed fully passive RFID tags using metamaterial-inspired antennas for capacitive sensing applications," in *Proc. IEEE MTT-S Int. Microw. Symp. (IMS)*, Seattle, WA, USA, Jun. 2013, pp. 1–4.

[110] R. Bhattacharyya, C. Floerkemeier, and S. Sarma, "Low-cost, ubiquitous RFID-tag-antenna-based sensing," *Proc. IEEE*, vol. 98, no. 9, pp. 1593–1600, 2010.

[111] J. Kimionis and M. M. Tentzeris, "Pulse shaping: The missing piece of backscatter radio and RFID," *IEEE Trans. Microw. Theory Techn.*, vol. 64, no. 12, pp. 4774–4788, Nov. 2016.

[112] H. J. Visser, A. C. Reniers, and J. A. Theeuwes, "Ambient RF Energy Scavenging: GSM and WLAN Power Density Measurements," in *Proc. IEEE Europ. Microw. Conf. (EuMC)*, Amsterdam, Netherlands, Jun. 2008, pp. 721–724.

[113] L. Guenda, E. Santana, A. Collado, K. Niotaki, N. B. Carvalho, and A. Georgiadis, "Electromagnetic energy harvesting-global information database," *Trans. on Emerging Telecom. Tech.*, vol. 25, no. 1, pp. 56–63, Jun. 2014.

[114] M. Piñuela, P. D. Mitcheson, and S. Lucyszyn, "Ambient RF energy harvesting in urban and semi-urban environments," *IEEE Trans. Microw. Theory Techn.*, vol. 61, no. 7, pp. 2715–2726, May. 2013.

[115] K. Mimis, D. Gibbins, S. Dumanli, and G. T. Watkins, "Ambient RF energy harvesting trial in domestic settings," *IET Microwaves, Ant. & Prop.*, vol. 9, no. 5, pp. 454–462, Apr. 2015.

[116] K. Gudan, S. Chemishkian, J. J. Hull, S. J. Thomas, J. Ensworth, and M. S. Reynolds, "A 2.4 GHz Ambient RF Energy Harvesting System with -20dbm Minimum Input Power and NiMH Battery Btorage," in *Proc. IEEE Conf. on RFID Techn. and Appl. (RFID-TA)*, Tampere, Finland, Sep. 2014, pp. 7–12.

[117] Y. Kawahara, X. Bian, R. Shigeta, R. Vyas, M. M. Tentzeris, and T. Asami, "Power Harvesting from Microwave Oven Electromagnetic Leakage," in *ACM*

Int. joint Conf. on Pervasive and Ubiq. Comp., Zurich, Switzerland, Sep. 2013, pp. 373–382.

[118] J. Bito, R. Bahr, J. G. Hester, S. A. Nauroze, A. Georgiadis, and M. M. Tentzeris, "A Novel Solar and Electromagnetic Energy Harvesting System With a 3-D Printed Package for Energy Efficient Internet-of-Things Wireless Sensors," *IEEE Trans. Microw. Theory Techn.*, vol. 65, no. 5, pp. 1831–1842, Feb. 2017.